A mathematical study of the Darwin–Howie–Whelan equations for Transmission Electron Microscopy

Dissertation

zur Erlangung des akademischen Grades

Doctor rerum naturalium
(Dr. rer. nat.)

im Fach: Mathematik

eingereicht an der
Mathematisch-Naturwissenschaftlichen Fakultät
der
Humboldt-Universität zu Berlin
von

Anieza Maltsi

Präsidentin der Humboldt-Universität zu Berlin:
Prof. Dr. Julia von Blumenthal

Dekanin der Mathematisch-Naturwissenschaftlichen Fakultät:
Prof. Dr. Caren Tischendorf

Tag der mündlichen Prüfung: 11.11.2022

Gutachter:
1. Prof. Dr. Alexander Mielke
2. Prof. Dr. Matthias Ehrhardt
3. Prof. Dr. Michael Lehmann

Abstract

In this thesis a mathematical study on the Darwin–Howie–Whelan (DHW) equations is provided. The equations are commonly used to describe and simulate the scattering of fast electrons in transmission electron microscopy (TEM). They are a system for infinitely many envelope functions, derived from the Schrödinger equation. However, for the simulation of images only a finite set of envelope functions is used, leading to a finite system of ordinary differential equations in the thickness direction of the specimen. Until now, there has been no systematic discussion about the accuracy of approximations depending on the choice of the finite sets used. This question is approached here by studying the mathematical structure of the system and providing error estimates to evaluate the accuracy of special approximations, like the two-beam and the systematic-row approximation. This way, mathematical guidelines for optimal choices are provided and are justified by exact error estimates.

Then a mathematical model and a toolchain for the numerical simulation of TEM images of semiconductor quantum dots (QDs) is developed. This includes elasticity theory to obtain the strain profile coupled with the Darwin-Howie-Whelan equations. A simulation study is performed on indium gallium arsenide QDs with different shapes and the resulting TEM images are compared to experimental ones. This toolchain is used to generate a database of simulated TEM images, which is a key element of a novel concept for model-based geometry reconstruction of semiconductor QDs, involving machine learning techniques.

Finally, symmetries observed in TEM images are investigated with respect to the DHW equations. The motivation for this is that TEM images of strained crystals often exhibit symmetries, the source of which is not always clear. To understand the source, symmetries that occur from the imaging process itself are distinguished from symmetries of the inclusion that might affect the image. Then, mathematical proofs are given showing that the intensities of the solutions of the DHW equations are invariant under specific transformations. A combination of these invariances with specific properties of the strain profile can then explain symmetries observed in TEM images. The results are demonstrated by using selected examples in the field of semiconductor nanostructures, such as quantum wells and quantum dots.

Zusammenfassung

Diese Arbeit liefert einen Beitrag zur mathematischen Untersuchung der Darwin-Howie-Whelan (DHW) Gleichungen. Sie werden üblicherweise zur Beschreibung und Simulation der Diffraktion schneller Elektronen in der Transmissionselektronenmikroskopie (TEM) verwendet. Sie bilden ein System aus Gleichungen für unendlich viele Enveloppenfunktionen, das aus der Schrödinger-Gleichung abgeleitet werden kann. Allerdings wird für Simulation von TEM Bildern nur ein endlicher Satz von Enveloppenfunktionen verwendet, was zu einem System von gewöhnlichen Differentialgleichungen in Richtung der Dicke der Probe führt. Bis jetzt gibt es keine systematische Analyse zur Genauigkeit dieser Näherungen in Abhängigkeit von der Auswahl der verwendeten endlichen Sätze von Enveloppenfunktionen. Diese Frage wird hier untersucht, indem die mathematische Struktur des Systems analysiert wird und Fehlerabschätzungen zur Bewertung der Genauigkeit spezieller Näherungen hergeleitet werden, wie der Zweistrahl-Approximation oder der sogenannten systematischen Reihe. Auf diese Weise werden mathematische fundierte Regeln für optimale Auswahl der Enveloppenfunktionen begründet und durch exakte Fehlerabschätzungen gerechtfertigt.

Anschließend wird ein mathematisches Modell und eine Toolchain für die numerische Simulation von TEM-Bildern von Halbleiter-Quantenpunkten entwickelt. Dazu gehört die Elastizitätstheorie zur Bestimmung der Verformung des Kristallgitters und die Kopplung an die DHW Gleichungen. Es wird eine Simulationsstudie an Indium-Gallium-Arsenid-Quantenpunkten mit unterschiedlicher Geometrie durchgeführt und die resultierenden TEM Bilder werden mit experimentellen Bildern verglichen. Diese Toolchain wird verwendet, um eine Datenbank von simulierten TEM-Bildern zu erzeugen, die ein Schlüsselelement eines neuartigen Konzepts für die modellbasierte Geometrie Rekonstruktion von Halbleiter-Quantenpunkten aus TEM-Bildern darstellt, das Techniken des maschinellen Lernens verwendet.

Schließlich werden die in TEM Bildern beobachteten Symmetrien im Hinblick auf die DHW Gleichungen untersucht. Die Motivation dafür ist, dass TEM Bilder von verspannten Kristallen oft Symmetrien aufweisen, deren Ursache nicht immer klar ist. Um die Ursachen zu verstehen, werden Symmetrien, die durch den Abbildungsprozess selbst entstehen, von Symmetrien des beobachteten Objektes, die beide das TEM Bild beeinflussen können, unterschieden. Dazu werden mathematische Resultate formuliert und bewiesen, die zeigen dass die Intensitäten der Lösungen der DHW Gleichungen unter bestimmten Transformationen invariant sind. Durch die Kombination dieser Invarianten mit spezifischen Eigenschaften des Deformationsfeldes können dann die in TEM Bildern beobachteten Symmetrien erklärt werden. Die Ergebnisse werden anhand ausgewählter Beispiele aus dem Bereich der Halbleiter-Nanostrukturen wie Quantensichten und Quantenpunkte demonstriert.

Acknowledgments

At this point, I would like to take the opportunity to thank the people who supported me during my PhD studies.

First and foremost, I would like to thank my supervisor, Alexander Mielke, for his guidance and support during these years. Working with him was an amazing learning opportunity, for which I will always be grateful. I would also like to thank Thomas Koprucki, for his continuous support and encouragement, on a scientific as well as on a personal level. He truly is a mentor to me. I am extremely grateful to Karsten Tabelow, Timo Streckenbach, Tore Niermann and Laura Niermann for working together in this interdisciplinary research and sharing their knowledge with me.

Additionally, this endeavor would not have been possible without the funding from the Einstein Center for Mathematics Berlin under project MATHEON- OT7 "Model-based geometry reconstruction of quantum dots from TEM” (duration 1.6.2017-31.12.2018) and Deutsche Forschungsgemeinschaft (DFG) through the Berlin Mathematics Research Center MATH+ (EXC-2046/1, project ID: 390685689) under the project EF3-1 "Model-based geometry reconstruction from TEM images” (duration 1.1.2019-31.12.2021).

I am extremely thankful for the support of my partner, Alex, who always believed in me, even when I did not believe in myself. Thank you for showing me your love for almost a decade and being my person. Thank you, also, for sharing your beautiful latex template. Of course, special thanks go to my friends: Jacqueline, Stelios, Betty, Dimitra, Aggeliki, Voula, Vaios, Stavros, Spiros, Stefanos and Marios. You were always there for me, supporting me in every step and filling the last years in Berlin with exciting moments, despite all the difficulties.

Finally, words can not express my gratitude to my mother who, despite all the difficulties that came her way, put all her energy and effort to make sure that I will have the opportunity to study. Without you, I would not have made it.

List of publications

The work presented here is based on the following papers:

1. Th. Koprucki, A. Maltsi, A. Mielke. *Symmetries in TEM imaging of crystals with strain*. Under review, Preprint in: *arXiv preprint*, (2022), DOI:10.48550/ARXIV.2206.01689
2. Th. Koprucki, A. Maltsi, A. Mielke. *On the Darwin-Howie-Whelan equations for the scattering of fast electrons described by the Schrödinger equation*. In: *SIAM Journal on Applied Mathematics* **81**, 1552-1578, (2021), DOI:10.1137/21M139164X
3. A. Maltsi, T. Niermann, T. Streckenbach et al. *Numerical simulation of TEM images for In(Ga)As/GaAs quantum dots with various shapes*. In: *Opt Quant Electron* **52**, 257 (2020). DOI:10.1007/s11082-020-02356-y

and was motivated by the work in the following conference proceedings:

1. Th. Koprucki, A. Maltsi, T. Niermann, T. Streckenbach, K. Tabelow, J. Polzehl. *On a database of simulated TEM images for In(Ga)As/GaAs quantum dots with various shapes*. In: *Proceedings of the 19th International Conference on Numerical Simulation of Optoelectronic Devices – NUSOD 2019*, J. Piprek, K. Hinze, eds., IEEE Conference, 2019, pp. 13–14, DOI: 10.1109/NUSOD.2019.8807025
2. A. Maltsi, Th. Koprucki, T. Niermann, T. Streckenbach, K. Tabelow, J. Polzehl. *Model-based geometry reconstruction of quantum dots from TEM*. In: *Proceedings in Applied Mathematics and Mechanics (PAMM)*, **Volume 18**, 2018, p. 201800398, DOI: 10.1002/pamm.201800398
3. Th. Koprucki, A. Maltsi, T. Niermann, T. Streckenbach, K. Tabelow, J. Polzehl. *Towards model-based geometry reconstruction of quantum dots from TEM*. In: *Proceedings of the 18th International Conference on Numerical Simulation of Optoelectronic Devices (NUSOD 2018)*, A. Djurišić, J. Piprek, eds., IEEE Conference Publications, 2018, pp. 115-116, DOI: 10.1109/NUSOD.2018.8570246

Contents

List of Notations xix

1 Introduction 1

2 Transmission Electron Microscopy imaging 5

  2.1 Crystallography basics 7

    2.1.1 Direct space 7

    2.1.2 Miller indices 9

    2.1.3 Reciprocal space 9

  2.2 Bragg's equation and Ewald sphere 11

  2.3 Column approximation 13

  2.4 Dynamical electron scattering 15

3 On the Darwin–Howie–Whelan equations for the scattering of fast electrons 19

  3.1 Setup of the model 20

  3.2 Sets of admissible beams 21

  3.3 Mathematical estimates 23

    3.3.1 Conservation of norms 24

3.3.2 Exponential decay of modes 26
3.3.3 Error estimates for finite-dimensional approximations 29
3.3.4 Averaging via conservation of the energy norm 32
3.4 Special approximations 35
3.4.1 Free-beam approximation 35
3.4.2 Approximation via the lowest-order Laue zone 36
3.4.3 Two-beam approximation and beating 37
3.4.4 Systematic-row approximation 39
3.5 Simulations for TEM experiments 41

4 Simulated TEM Images of Quantum Dots **45**
4.1 Model based geometry reconstruction approach 46
4.2 Influence of strain in the DHW equation 47
4.3 Elasticity theory and Eshelby's method 49
4.4 Numerical simulation of TEM images for different geometries 50
4.4.1 Toolchain for simulation of TEM images 50
4.4.2 Spherical QD 51
4.4.3 Pyramidal and lens-shaped QDs 52
4.5 Database of TEM images 54

5 Symmetries in TEM imaging of strained crystals **57**
5.1 Image symmetries via the DHW equations 58
5.2 Symmetries in TEM images 59
5.2.1 Symmetry with respect to the sign of the displacement 60

5.2.2 Symmetry with respect to the center of the sample 61
5.2.3 Symmetry with respect to the sign of s_g 62
5.2.4 Symmetries explained via DHW equations 63
5.2.5 Mirrored TEM images induced by strain 68
5.2.6 Symmetries for general profiles 70
5.3 Mathematical treatment of the symmetries 71

6 Summary and Outlook **77**

Appendices **79**

A Lattice and elastic constants **81**

List of Figures

2.1 Ray path within TEM 6

2.2 Experimental TEM images of InAs QDs 6

2.3 A 2D lattice with basis vectors a,b 7

2.4 3D lattices 8

2.5 Planes and Miller indices 10

2.6 Bragg's condition in real space 12

2.7 Ewald sphere construction 13

2.8 Column approximation 14

2.9 Experimental setup 16

3.1 Plot of second and first derivative terms 22

3.2 Sets of admissible beams 23

3.3 Atomic form factors and scattering potential 27

3.4 Lowest order Laue zone 34

3.5 A typical setup for the two-beam conditions 38

3.6 Amplitudes for different excitation errors 42

3.7 Simulation for different sets of beams 43

4.1 MBGR approach 46

4.2 Simulation of TEM images 47

4.3 Crystal lattice with spherical inclusion 48

4.4 Eshelby's method 49

4.5 Simulated TEM images for spherical QD 51

4.6 3D view of the geometry of a lens-shaped and a pyramidal quantum dot . 52

4.7 Simulated TEM images for different geometries 53

4.8 Comparison of experimental and simulated images 54

4.9 Series of simulated TEM images 56

5.1 Simulation of TEM images for pyramidal QD 60

5.2 TEM imaging of inclined quantum well 61

5.3 TEM imaging of spherical quantum dot 62

5.4 Series of TEM images for a spherical quantum dot 63

5.5 Strong and weak symmetry in four-beam approximation 65

5.6 Plots of shifted even and odd functions 68

5.7 Mirrored images 69

5.8 Pyramidal quantum dot with a rhomboidal base 70

5.9 Pyramidal quantum dot with different lateral aspect ratio 71

List of Tables

2.1 Coefficients of the Schrödinger equation 15

3.1 Comparison of first and second derivative 22
3.2 Comparison of Laue approximation and systematic row 40
3.3 Excitation errors 41
3.4 Comparison of solutions 43

5.1 Comparison of intensities at the exit plane for the four-beam model 66
5.2 Comparison of intensities at the exit plane for the two-beam model 66

A.1 Lattice and elastic constants of GaAs and InAs 81
A.2 Lattice and elastic constants of $In_{1-x}Ga_xAs$ 82

List of Notations

Λ	Primal Lattice 7
Λ^*	Dual Lattice 9
$\mathbf{k_0}$	Wave vector of incoming beam 11
$\mathbb{S}_{\mathrm{Ew}}$	Ewald sphere 12
$s_{\mathbf{g}}$	Excitation error 13
$\boldsymbol{\mathcal{U}}$	Effective periodic potential 15
$\boldsymbol{\nu}$	Outwards normal 15
$\psi_{\mathbf{g}}$	Slowly varying envelope function 16
$U_{\mathbf{g}}$	Fourier coefficients of the periodic potential 16
$\rho_{\mathbf{g}}$	Projected momentum of diffracted wave 16
$\sigma_{\mathbf{g}}$	Deviation from Ewald sphere 16
$\boldsymbol{\psi} = (\psi_{\mathbf{g}})_{\mathbf{g}\in\Lambda^*_m}$	State vector of envelope functions 17
$\mathbf{g}_{\mathrm{ap}}$	Beam chosen by the objective aperture 17
$\Lambda^{*\gamma}$	Set of admissible beams 21
Λ^{*M}	Reduced set of admissible beams 21
$\Vert\psi\Vert_{\Lambda^*_m}$	Wave-flux norm 24
$\mathfrak{H}(\Lambda^*_m)$	Hilbert Space 24
$\langle A, B\rangle_{\Lambda^*_m}$	Scalar product on $\mathfrak{H}(\Lambda^*_m)$ 24
$\Vert\boldsymbol{\psi}\Vert^2_\alpha$	Exponentially weighted norm 26
$\kappa(\alpha)$	Exponential factor of potential 26
$\frac{\alpha}{\kappa(\alpha)}$	Collective scattering length 29
ξ_g	Extinction length 29
$\ell_{\mathrm{excit}}(s_g)$	Excitation length 29
$\Lambda^{*M}_{\mathrm{Ew}}$	Ewald reduction 33
$\mathbf{T}_{\mathbf{k_0}}$	Tangent plane to the Ewald sphere 36
$\Lambda^*_{\mathrm{LOLZ}}$	Lower order Laue zone 36
$\Lambda^*_{\mathrm{syrow}}$	Systematic row 39
ε^*	Eshelby's eigenstrain 49
σ^*	Eshelby's eigenstress 49
$I_{\mathbf{g}_{\mathbf{ap}}}(i, j)$	Intensity for chosen beam $\mathbf{g}_{\mathbf{ap}}$ at pixel (i, j) 50
$F(z)$	Strain profile 59
$R(z)$	Flip operator 74

Chapter 1

Introduction

The use of various glass types to make objects look bigger was already known to ancient Romans and Egyptians. But the invention of the first microscope is traced back to the 16th century when Zacharias and Hans Janssen, two Dutch spectacle makers, created the first compound microscope. Their instrument could achieve a magnification of 3× to 9× bigger. This new instrument, which we now know revolutionised science and our lifes, was met with a lack of interest from scientists, see [Bal66]. Although impressed by the ability to observe objects closer, people did not use this new invention in doing observations in their scientific work, until decades later. The entrance of the microscope into the scientific world starts in the 17th century. In 1609 it was Galileo Galilei who turned his telescope into a microscope, using lenses with a shorter focal length, and achieved a magnification of 30× bigger. But the first use of observations made with a microscope to give scientific explanations was done in 1654 by Peter Borel in *Historiarum et Observationum Medicophysicarum*, which is the first medical work using a microscope. Our next stop in this short trip to the history of microscopy is 1665, when Robert Hooke wrote *Micrographia*, in which he includes his observations on fleas and corks using a microscope. It is in this work that he observed pores on the cork, not realising though that he had just discovered plant cells. Then, in 1674 Anton van Leeuwenhoek created a microscope that achieved a higher magnification ranging from 70× to 270× bigger. He observed, among other things, bacteria for the first time in history.

Since then, the microscope not only entered the scientific world but it became the backbone of modern science. It opened to us the door for the "micro" world. Many scientific fields, from life sciences to technology, cannot even be imagined without the microscope. With mechanical developments and lens improvements, the microscope changed through the years. What was initially a tube with two lenses at the opposite ends of it evolved into a much more complicated structure, providing us with so many different types of microscopes. While the first ones were based on light in the visible part of the spectrum, limiting their spatial resolution due to the connection between the wavelength of the propagating waves and the minimal size of distinguishable objects, modern microscopes use other types of waves to image even tinier objects. One example is the transmission electron microscope (TEM), invented by Ernst Ruska and Max Knoll in 1931. In TEM, images are created by the propagation of electron waves through the sample, allowing imaging of the crystallographic structure of materials down to an atomic scale. This made TEM an indispensable experimental tool to examine objects in life sciences or material sciences at nanoscales.

In addition to developments in microscopes, we have reached a time where a powerful computer is much cheaper than an average electron microscope. This can be a powerful tool for the creation of TEM images, as well as for their interpretation. The image simulation involves numerical calculations of the image based on first principles and a detailed description of the microscope and the specimen. The processing of the image aims at extracting information for the specimen from the simulated image. Both the creation of the image as well as its interpretation inherently require mathematical theory to solve the reconstruction problem for a single specimen and to allow for automated processing of bulks of them. The analysis of the mathematics behind transmission electron microscopy is the main focus of this thesis. The biggest challenge in this (and at the same time the most interesting part) is that it requires two communities to work together, applied mathematicians and experimental physicists. To help this communication, I tried to write the thesis in a way that both mathematicians and physicists can understand the results, even though the proofs are more technical and aimed at mathematicians.

Chapter 2 aims at giving an overview of the image formation process and the physical procedures behind it. While writing it I had in mind what I would like to have known at the beginning of my PhD. This means that this chapter is written for a mathematician who is getting started with transmission electron microscopy and needs to learn the fundamental concepts behind it, in order to be able to communicate with physicists on the one hand and to understand the derivation of the equations describing the electron propagation, called the Darwin–Howie–Whelan (DHW) equations, on the other hand. When someone starts reading about TEM, the amount of information is so big and the notation used so diverse that it is easy to get lost. I tried to keep it as simple as possible and included only the minimum knowledge needed to get started. At the same time, this chapter serves as a smooth introduction to the notation used in the next chapters, which can get quite complicated.

In Chapter 3 the results from our paper [KMM21] are presented. The work described here is mainly focused on the mathematical analysis of the Darwin–Howie–Whelan equations. They are widely used for the numerical simulation of TEM images, e.g. see [Nie19] for the software package `pyTEM`. They provide a theoretical basis that allows one to construct suitable experimental setups for obtaining microscopy data on the one hand, and can be used to analyze measured data in more details on the other hand. The origins of this model go back to Darwin in [Dar14] with major generalizations by Howie and Whelan in [HW61]. Currently, many quantitative methods emerge for applications in TEM

[Nie19; WS19], holography [LJC+14; JLC+14], scanning electron microscopy [PSC+18; Pas19], electron backscatter diffraction [WTS+07; ZD20] and electron channelling contrast imaging [PHN+18], where quantitative evaluations of micrographs are compared to simulation results to replace former qualitative observations by rigorous measurements of embedded structures in crystals. For that reason, it is essential to evaluate the accuracy and the validity regime of the chosen modeling schemes and simulation tools. In electron microscopy, this includes the heuristic approaches to select the relevant beams in multi-beam approaches [WTS+07; Nie19; WS19]. This chapter is devoted to the theory behind the DHW equations and thus provides mathematical arguments and refinements for the beam-selection problem.

In Chapter 4 the results from our paper [MNS+20] are presented. Here, a mathematical model and a toolchain for the numerical simulation of TEM images for semiconductor quantum dots (QDs) are provided, see [KMN+19]. This work was motivated by the concept of *Model-based geometry reconstruction of quantum dots* first introduced in [MKN+18]. As a first step towards this, a simulation study on lens-shaped and pyramidal indium gallium arsenide QDs embedded in a gallium arsenide matrix is performed and the resulting TEM simulations are compared to experimentally derived images. It is known that TEM images are very sensitive to strain fields around QDs and these fields are mostly responsible for the observed contrast. In order to link the contrasts in TEM images with shapes and concentration of these QDs, it is crucial to combine strain calculations with TEM image simulations. Previous examples of investigations with combined finite element and image calculations include the explanation of surface relaxation contrasts along quantum wells by [JAB+98] and explanation of the typical coffee-bean contrast around QDs by [BFAL96]. Previous observations of [LZD+98] showed that, for single excitation conditions, it is hard to distinguish between effects of shape and crystal symmetries on the TEM images. By our systematic study of the influence of the shape on the image contrast, we could identify excitation conditions that allow to distinguish between lens-shaped and pyramidal QDs.

In Chapter 5 the symmetry properties of the TEM imaging process are analysed via the DHW equations. This analysis showed that the imaging process is invariant under special transformations. The most important symmetries are the sign change of the strain field and the midplane reflection, as well as a symmetry related to the sign change of the excitation error. The latter can be of particular importance in experiments, since modern transmission electron microscopes can create series of images by varying the excitation error, leading to sign changes. In Section 5.2, well chosen examples of symmetries in TEM images are given. These symmetries can be explained by a combination of the theory developed and properties of the strain profile. In 5.2.4 the results are stated in a simple way, while the mathematical proofs of them are in Section 5.3. I think this structure, while a bit unorthodox, serves the communication between the two communities better since the reader does not have to go through the proofs in order to understand the results, unless they want to. At the time of writing, the work presented here has been submitted for publication and is under peer review. A preprint can be found in [KMM22].

Finally, a summary of all the results and an outlook of possible future applications is given in Chapter 6.

Chapter 2

Transmission Electron Microscopy imaging

Transmission electron microscopy (TEM) images are formed by transmitting a beam of electrons through the specimen. The thickness of the specimen is typically below a few hundred nanometers. The electrons interact with the specimen and due to the periodic structure of the latter, the beams are diffracted in discrete directions. In Figure 2.1 we can see a sketch of how a TEM image is created. A parallel electron beam illuminates the specimen. The diffracted beams, that leave the exit surface of the specimen, are focused again by the objective into a magnified image. The set of beams forming the image can be reduced by the objective aperture. If the image that is created includes the undiffracted beam it is called *bright field* image, otherwise it is a *dark field* image.

One of the things that make TEM images interesting is the fact that they are sensitive to specific components of the displacement. In Figure 2.2 we see experimental dark field images of two QDs, in the directions (040) and (004). Both images are showing a coffee-bean-like contrast along the direction of the respective diffraction vector. One use of this sensitivity to certain components of the displacement field is imaging of dislocations. In dislocations, depending on the type, the displacement field has vanishing components in certain directions and these directions can be found by looking for diminishing contrast under the two-beam conditions for different vectors $\mathbf{g}$. Typically, the contrast vanishes for directions $\mathbf{g}$ perpendicular to the Burger's vector of the dislocation, i.e. $\mathbf{g} \cdot \mathbf{b} = 0$ [De 03].

We will come back to images and displacement fields but for now what is important is to understand a bit the imaging procedure, because this will be useful for understanding the mathematical analysis done in the next chapters. We will start with an overview of crystallography, since the specimen is a crystalline object. This will lead us to the conditions that need to be satisfied in order for the beams to be diffracted in discrete directions.

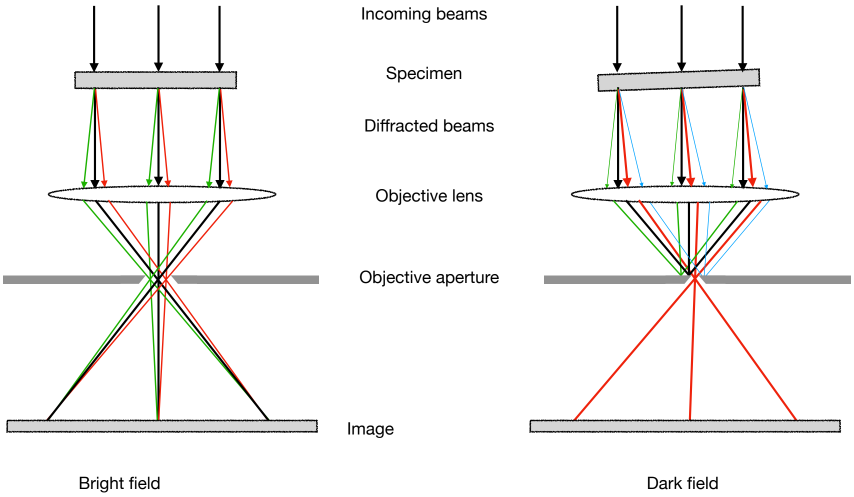
Incoming beams
Specimen
Diffracted beams
Objective lens
Objective aperture
Image
Bright field
Dark field

Figure 2.1: Ray path within TEM. In the first case the objective aperture selects all beams, while in the second the objective aperture only selects the strongly excited beam (dark field image). Adapted from [MNS+20, Fig.1] and used under CC-BY.

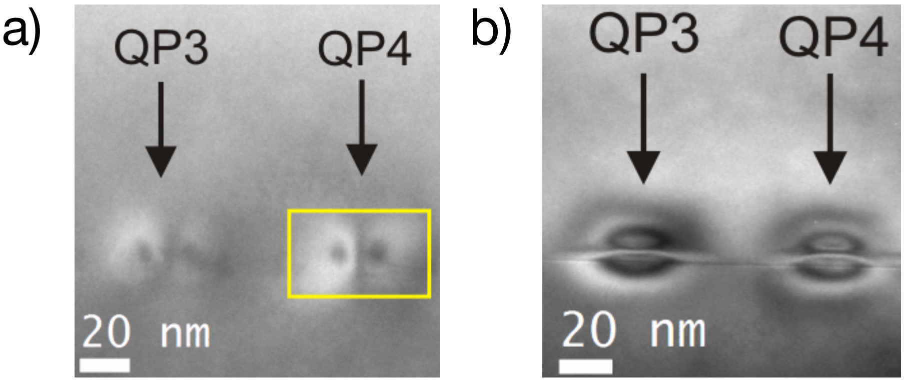
a)
QP3
QP4
20 nm
b)
QP3
QP4
20 nm

Figure 2.2: Experimental TEM images of InAs QDs: (a) dark field of (040) beam, sensitive to [010]-component of strain (b) dark field of (004) beam, sensitive to [001]-component of strain, adapted from [Har11], both showing a coffee-bean-like contrast. © 2018 IEEE. Reprinted, with permission, from [KMN+18].

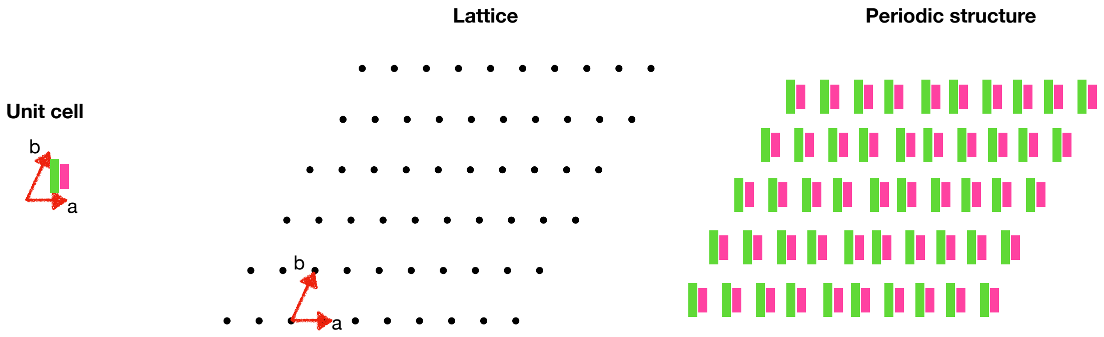

Figure 2.3: A 2D lattice with basis vectors a,b. Repetition of the motif inside the unit cell creates the periodic structure.

2.1 Crystallography basics

It would be impossible to continue talking about TEM imaging without some basic knowledge of crystallography. We start by introducing the direct or real space. This will be our tool to describe the crystal, the positions of atoms in it as well as the distances between atoms. Next, by introducing the Miller indices, we define the reciprocal space and show how the same calculations can be done there. There is so much more in crystallography that is not included here, since the goal is to keep it simple, but fortunately the literature is extensive and the reader who is interested in learning more has many choices, like [DM12; De 03; Bor12] or [Sen90; Pri82; Eng86] for a more mathematical approach.

2.1.1 Direct space

We start with the introduction of the primal lattice, which in physics literature is called direct lattice. Let $\mathbf{a_i} \in \mathbb{R}^d$ be independent vectors. The lattice generated by them is:

$$\Lambda := \{\mathbf{r} = \sum r_i \mathbf{a_i} | r_i \in \mathbb{Z}.\} \tag{2.1}$$

We call $\mathbf{a_i}$ the basis vectors. In the case $d = 3$, a vector $\mathbf{r} \in \Lambda$ is written as: $\mathbf{r} = r_1\mathbf{a_1}+r_2\mathbf{a_2}+r_3\mathbf{a_3}$ and it represents a direction in the crystal lattice , which is usually written as $[r_1 r_2 r_3]$. For negative components a minus sign above the corresponding component is used, e.g. $[r_1 \bar{r}_2 r_3]$ corresponds to the vector $\mathbf{r} = r_1\mathbf{a_1} - r_2\mathbf{a_2} + r_3\mathbf{a_3}$. The volume created by the basis vectors is called a unit cell. Repetition of the unit cell along the directions of the lattice creates the crystal structure. An example in 2D is given in Figure 2.3. A lattice can be described by its lattice parameters, which for a 3 dimensional lattice are $\{a, b, c, \alpha, \beta, \gamma\}$ with $|\mathbf{a_1}| = a$, $|\mathbf{a_2}| = b$, $|\mathbf{a_3}| = c$ and α, β, γ the angles between the basis vectors. In 3D we have 14 unique lattices called Bravais lattices, after Auguste Bravais who introduced them in 1850 [Bra50]. In Figure 2.4 we see three of them and their lattice parameters. Next we would like to compute distances and angles between atoms in the unit cell. Two vectors $\mathbf{r}, \mathbf{q}$ in physical space $\mathbb{R}^3$ have a Euclidean norm and a scalar product. However,

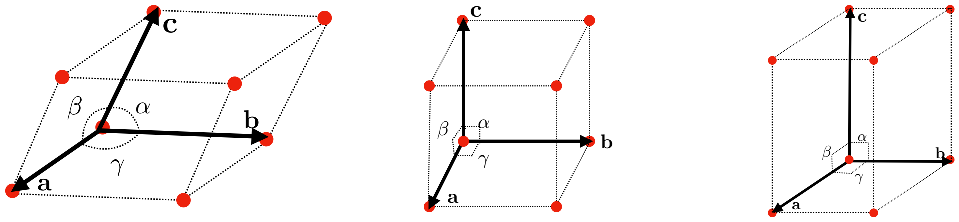

(a) Triclinic unit cell **(b)** Cubic unit cell **(c)** Tetragonal unit cell

Figure 2.4: The triclinic lattice in 2.4a is described by $\{a, b, c, \alpha, \beta, \gamma\}$ with $a \neq b \neq c$ and $\alpha \neq \beta \neq \gamma$. For the cubic lattice 2.4b we have $\{a, a, a, \frac{\pi}{2}, \frac{\pi}{2}, \frac{\pi}{2}\}$ and for the tetragonal 2.4c $\{a, a, c, \frac{\pi}{2}, \frac{\pi}{2}, \frac{\pi}{2}\}$.

we will mainly use the crystallographic basis $\{\mathbf{a_1}, \mathbf{a_2}, \mathbf{a_3}\}$. The dot product between two vectors $\mathbf{r}, \mathbf{q}$ in a general reference frame is given by $\mathbf{r} \cdot \mathbf{q} \equiv |\mathbf{r}||\mathbf{q}| \cos\theta$, with θ being the angle between the vectors. The length of a vector $\mathbf{r} = r_1\mathbf{a_1} + r_2\mathbf{a_2} + r_3\mathbf{a_3}$ is then given by:

$$|\mathbf{r}| = \sqrt{\sum_i \sum_j r_i(\mathbf{a_i} \cdot \mathbf{a_j})r_j} = \sqrt{r_i(\mathbf{a_i} \cdot \mathbf{a_j})r_j}. \tag{2.2}$$

In the last equality, we used the Einstein summation convention: *When a subscript occurs twice in the same term of an equation, then a summation is implied over all values of this subscript and the summation sign can be dropped.* Now, we introduce the notion of the direct metric tensor $\mathbb{G} \in \mathbb{R}^{3\times3}$, which is important in crystallographic computations and is defined as:

$$\mathbb{G} \equiv (\mathbf{a_i} \cdot \mathbf{a_j})_{i,j\in\{1,2,3\}} = \begin{bmatrix} \mathbf{a_1} \cdot \mathbf{a_1} & \mathbf{a_1} \cdot \mathbf{a_2} & \mathbf{a_1} \cdot \mathbf{a_3} \\ \mathbf{a_2} \cdot \mathbf{a_1} & \mathbf{a_2} \cdot \mathbf{a_2} & \mathbf{a_2} \cdot \mathbf{a_3} \\ \mathbf{a_3} \cdot \mathbf{a_1} & \mathbf{a_3} \cdot \mathbf{a_2} & \mathbf{a_3} \cdot \mathbf{a_3} \end{bmatrix}. \tag{2.3}$$

All the above quantities now can be described in terms of $\mathbb{G}$, as we will see in the following simple example.

Example 2.1.1. *For the tetragonal lattice with parameters $a = \frac{1}{3}$ and $c = \frac{1}{2}$, find the dot product and the angle between the vectors $\mathbf{r} = [\frac{1}{2}0\frac{1}{3}]$ and $\mathbf{q} = [\frac{1}{4}\bar{\frac{1}{2}}0]$. We first calculate the direct metric tensor, which is:*

$$\mathbb{G} = \begin{bmatrix} \frac{1}{9} & 0 & 0 \\ 0 & \frac{1}{9} & 0 \\ 0 & 0 & \frac{1}{4} \end{bmatrix}.$$

The dot product now can be calculated from:

$$\mathbf{r} \cdot \mathbf{q} = r_i\mathbf{a_i} \cdot q_j\mathbf{a_j} = r_i(\mathbf{a_i} \cdot \mathbf{a_j})q_j = \begin{bmatrix} \frac{1}{2} & 0 & \frac{1}{3} \end{bmatrix} \begin{bmatrix} \frac{1}{9} & 0 & 0 \\ 0 & \frac{1}{9} & 0 \\ 0 & 0 & \frac{1}{4} \end{bmatrix} \begin{bmatrix} \frac{1}{4} \\ -\frac{1}{2} \\ 0 \end{bmatrix} = \frac{1}{72}\, nm.$$

To find the angle we need the lengths of the vectors as well, which we find using the expression (2.2):

$$|\mathbf{r}| = \frac{\sqrt{2}}{6}\, nm, \quad |\mathbf{q}| = \frac{\sqrt{5}}{12}\, nm.$$

Then the angle can be calculated from:

$$\cos(\theta) = \frac{\mathbf{r} \cdot \mathbf{q}}{|\mathbf{r}||\mathbf{q}|} = \frac{1}{\sqrt{10}} \Rightarrow \theta = 71.56°.$$

2.1.2 Miller indices

Before defining the reciprocal lattice, we will introduce a method to label lattice planes, based on their intercepts with the crystal axes. By lattice plane we mean any plane that contains at least three non-colinear lattice points. The reason we need this is because the reciprocal lattice points represent planes in the direct space. A collection of equally spaced parallel lattice planes is a family of lattice planes. Miller [Mil39] provided a method to label these families of planes by indices, which are often called Miller indices or (hkl) indices. The method goes as follows: First we check if the plane goes through the origin. If yes, then we displace it so that it no longer contains the origin. Then we follow these three steps:

1. Determine the intercepts of the plane with the three basis vectors. In case the plane does not intercept one of the axes, the intercept is considered to be ∞.
2. Invert all three intercepts. In the case that the inverts are not integers, say we have a, b and c with rational ratios, we can still write them in terms of integer indices by scaling them appropriately.
3. Reduce all numbers to relative primes.

We write the three numbers surrounded by round brackets, i.e. (hkl), and these are the Miller indices of the plane. In Figure 2.5 we see two examples. In the first one 2.5a, the plane intercepts the axes at $\frac{1}{2}$ for a, $\frac{1}{2}$ for b and $\frac{1}{3}$ for c, and inverting these intercepts gives the millers indices (223). In the second example 2.5b the plane intercepts the b axes at 1 and the c axes at $\frac{1}{2}$. It does not intercept the a axes though. In this case we consider the intercept to be ∞. By inverting these we get the Millers indices (012). It can happen that we have irrational Miller indices. In this case we have an aperiodic pattern known as a quasicrystal. However, here we focus on periodic structures so the Miller indices will always be integers.

2.1.3 Reciprocal space

The dual lattice Λ^*, or reciprocal lattice as it is called in physics, is defined as:

$$\Lambda^* := \{\mathbf{g} \in (\mathbb{R}^d)^* | \ \mathbf{g} \cdot \mathbf{r} \in \mathbb{Z} \text{ for all } \mathbf{r} \in \Lambda\}. \tag{2.4}$$

A vector $\mathbf{g} \in \Lambda^*$ (for $d = 3$) is written as:

$$\mathbf{g} = h\mathbf{a_1}^* + k\mathbf{a_2}^* + l\mathbf{a_3}^*,$$

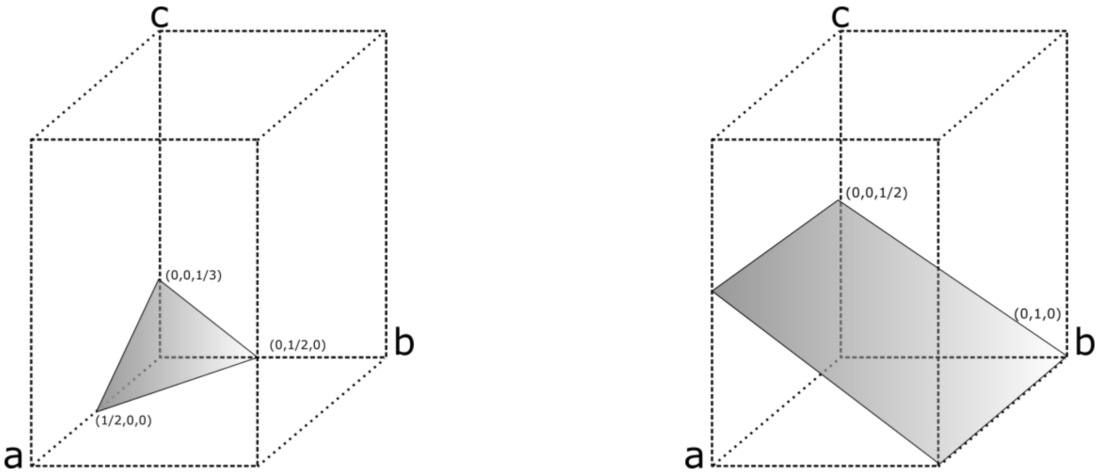

(a) Plane (223)

(b) Plane (012)

Figure 2.5: Planes in the unit cell and their Miller indices.

where the dual basis vectors $\mathbf{a_j}^*$ are defined as $\mathbf{a_i} \cdot \mathbf{a_j}^* = \delta_{ij}$, with δij the Kronecker delta. How is this connected with the Miller indices? Let $\mathbf{r} = x\mathbf{a_1} + y\mathbf{a_2} + z\mathbf{a_3} \in \Lambda$ be perpendicular to the dual lattice vector $\mathbf{g}$. Then we get:

$$\mathbf{g} \cdot \mathbf{r} = hx + ky + lz = 0, \tag{2.5}$$

which is the equation of a plane through the origin of the primal lattice. The general equation of a plane intersecting the basis vectors $\mathbf{a_i}$ at the points a_i, see [Spi68], is:

$$\frac{x}{a_1} + \frac{y}{a_2} + \frac{z}{a_3} = 1. \tag{2.6}$$

Translating the plane across its normal will change the value on the right-hand side of the equation, which becomes zero if the plane goes through the origin. Then by comparing Equation (2.5) with:

$$\frac{x}{a_1} + \frac{y}{a_2} + \frac{z}{a_3} = 0,$$

we see that $h = \frac{1}{a_1}, k = \frac{1}{a_2}, l = \frac{1}{a_3}$, hence the dual lattice vector $\mathbf{g}$ with components (h, k, l) is perpendicular to the plane with Miller indices (hkl). This means that the unit normal to the plane is $\mathbf{n} = \frac{\mathbf{g}}{|\mathbf{g}|}$.

The interplanar spacing d_{hkl} is defined as the distance between the equally spaced parallel planes expressed by the Miller indices (hkl). This will be equal to the perpendicular distance from the origin to the plane intersecting the direct basis vectors at the points $\frac{1}{h}$, $\frac{1}{k}$ and $\frac{1}{l}$. This distance is equal to the projection of any vector $\mathbf{r}$ ending in the plane onto the plane normal $\mathbf{n}$:

$$\mathbf{r} \cdot \mathbf{n} = \mathbf{r} \cdot \frac{\mathbf{g}}{|\mathbf{g}|} = d_{hkl}.$$

Choosing $\mathbf{r} = \frac{\mathbf{a_1}}{h}$, we have:

$$\mathbf{r} \cdot \mathbf{g} = \frac{\mathbf{a_1}}{h} \cdot (h\mathbf{a_1}^* + k\mathbf{a_2}^* + l\mathbf{a_3}^*) = 1 = d_{hkl}|\mathbf{g}|. \tag{2.7}$$

This shows that the length of a reciprocal lattice vector $\mathbf{g}$ is equal to the inverse of the spacing between the corresponding lattice planes: $|\mathbf{g}| = \frac{1}{d_{hkl}}$.

Now to compute angles and distances in the dual space, as we did in real space, we introduce the dual metric tensor:

$$\mathbb{G}^* \equiv (\mathbf{a_i}^* \cdot \mathbf{a_j}^*)_{i,j\in\{1,2,3\}} = \begin{bmatrix} \mathbf{a_1}^* \cdot \mathbf{a_1}^* & \mathbf{a_1}^* \cdot \mathbf{a_2}^* & \mathbf{a_1}^* \cdot \mathbf{a_3}^* \\ \mathbf{a_2}^* \cdot \mathbf{a_1}^* & \mathbf{a_2}^* \cdot \mathbf{a_2}^* & \mathbf{a_2}^* \cdot \mathbf{a_3}^* \\ \mathbf{a_3}^* \cdot \mathbf{a_1}^* & \mathbf{a_3}^* \cdot \mathbf{a_2}^* & \mathbf{a_3}^* \cdot \mathbf{a_3}^* \end{bmatrix} = (\mathbb{G})^{-1}. \tag{2.8}$$

This way we have that the length of a reciprocal lattice vector $\mathbf{g}$ is:

$$\frac{1}{d_{hkl}} = |\mathbf{g}| = \sqrt{g_i(\mathbf{a_i}^* \cdot \mathbf{a_j}^*)g_j}$$

and the angle between two vectors $\mathbf{g}, \mathbf{p}$ is given by: $\theta = \cos^{-1}\left(\frac{p_i(\mathbf{a_i}^* \cdot \mathbf{a_j}^*)g_j}{\sqrt{p_i(\mathbf{a_i}^* \cdot \mathbf{a_j}^*)p_j}\sqrt{g_i(\mathbf{a_i}^* \cdot \mathbf{a_j}^*)g_j}}\right)$.

We should by now understand that our specimen has a crystal structure and we can describe this via the direct space. We can find the positions of atoms and the distances between them. Then we have a second reference frame, the dual space. This corresponds to the image space. We can go from the direct space to the dual and back, by the duality relation in (2.8). If this is clear then we are ready to move on. The periodic structure of our specimen is the reason that the beams are diffracted in discrete directions. So, the next thing we need to understand is how to find these directions. For this, we need Bragg's equation and the notion of the Ewald sphere.

2.2 Bragg's equation and Ewald sphere

In Figure 2.6 we have an incoming wave with wavevector $\mathbf{k_0}$, which is incident to a set of parallel planes with Miller indices (hkl), and incidence angle θ. Part of the incident wave will pass through the plane and part will be reflected. Snell's law states that the incident and reflected angles are equal and the diffracted beam, the incoming beam and the normal vector are co-planar. A second wave is shown, with the same incident angle. These two waves are in phase, when the path difference between the two waves is equal to an integer multiple of the wavelength λ [De 03, Ch.2, p 96]:

$$2d_{\text{hkl}}\sin\theta = n\lambda. \tag{2.9}$$

This equation describes the n-th order diffraction from the plane (hkl). Equivalently, we can talk about the first order diffraction from the plane $(\hat{h}\hat{k}\hat{l}) = (nh\ nk\ nl)$, which

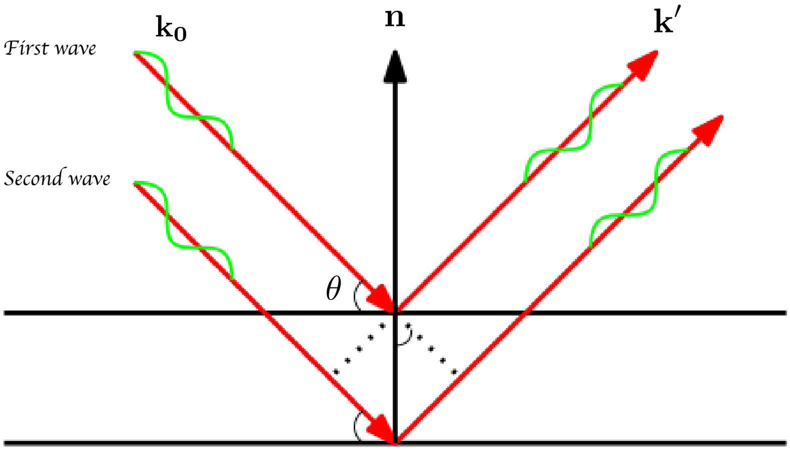

Figure 2.6: Bragg's condition in real space: For in-phase arrival of the two waves the path differences between them must equal to an integral number of wavelengths, leading to Equation (2.9).

is parallel to the plane (hkl) and has an interplanar spacing $d_{\hat{h}\hat{k}\hat{l}} = \frac{d_{hkl}}{n}$, and write the equation as:

$$2d_{\hat{h}\hat{k}\hat{l}}\sin\theta = \lambda.$$

This is Bragg's equation in real space. It is useful when we want to find the diffraction angle, but it does not give us any information about the absolute directions of the wave. For that, we transform the equation into the reciprocal space, which leads to the construction of the Ewald sphere, see Figure 2.7. As in Figure 2.6, $\mathbf{k_0}$ and $\mathbf{k'}$ denote the wavevectors of the incoming and the diffracted wave respectively. First, we translate the vector $\mathbf{k'}$ parallel to itself, until its starting point coincides with the starting point of $\mathbf{k_0}$, let us call it $\mathbf{C}$. Then we have:

$$\mathbf{k'} = \mathbf{k_0} + \mathbf{g} \text{ with } \mathbf{g} \in \Lambda^*. \tag{2.10}$$

This is Bragg's equation in reciprocal space. When this condition is satisfied, it means that a diffracted wave with wavevector $\mathbf{k'}$ may occur. Diffraction is usually an elastic scattering event, which means that the incoming beam and the diffracted one have the same wavelength λ, giving $|\mathbf{k_0}| = |\mathbf{k'}| = \frac{1}{\lambda}$ (Ewald condition). This implies that the wavevectors $\mathbf{k_0}$ and $\mathbf{k'}$ have to lie on the surface of a sphere, known as the Ewald sphere [Ewa21]. When a reciprocal lattice point falls on this sphere, the Ewald condition is satisfied. As seen in Figure 2.7, we can have more than one diffracted beams. So, for an incoming beam with wavevector $\mathbf{k_0}$, we write the Ewald sphere as the set of reciprocal lattice points satisfying the Ewald condition:

$$\mathbb{S}_{\text{Ew}} := \left\{ \mathbf{g} \in \Lambda^* \;\middle|\; |\mathbf{k_0}|^2 - |\mathbf{k_0}+\mathbf{g}|^2 = 0 \right\}. \tag{2.11}$$

In general, $\mathbb{S}_{\text{Ew}} \cap \Lambda^*$ may be trivial, i.e. it only contains $\mathbf{g} = \mathbf{0}$. However, diffraction can occur even when the Ewald condition is not exactly satisfied, say for lattice points that are close, in some sense, to the Ewald sphere. The distance of a reciprocal lattice point $\mathbf{g}$ from

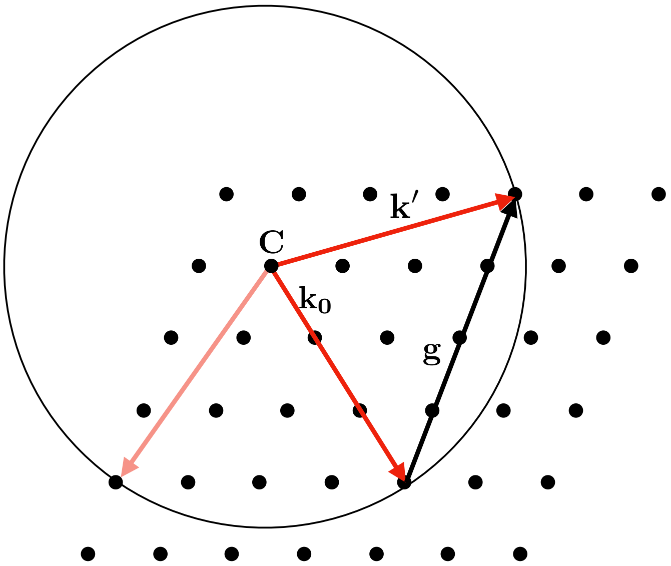

Figure 2.7: Ewald sphere construction: The reciprocal points that fall on this sphere satisfy the Bragg condition.

the Ewald sphere is usually expressed through a quantity called *excitation error* defined as:

$$s_{\mathbf{g}} = -\frac{\mathbf{g} \cdot (2\mathbf{k_0}+\mathbf{g})}{2|\mathbf{k_0}+\mathbf{g}|\cos\alpha} = \frac{|\mathbf{k_0}|^2 - |\mathbf{k_0}+\mathbf{g}|^2}{2(\mathbf{k_0}+\mathbf{g}) \cdot \boldsymbol{\nu}}, \tag{2.12}$$

where α is the angle between the vector $\mathbf{k_0} + \mathbf{g}$ and the foil normal $\boldsymbol{\nu}$. Maybe the term *error* does not sound good to mathematicians since it usually refers to some numerical error, which is not the case here, and *excitation parameter* would be better. However, to keep it consistent with the literature, I will refer to it as the *excitation error*, even though I see it more as a coefficient in an ordinary differential equation as we will see later. At the beginning of this chapter we said that the objective aperture can reduce the set of beams forming the image. Bragg's equation tells us which set of beams we should choose. Let us sum up what we know: We have a periodic structure. This makes beams diffract in discrete directions. We can find these directions by Bragg's equation. There is one last thing we need to know: the column approximation. Then we can fully understand how a TEM image is created.

2.3 Column approximation

In transmission electron microscopy, we deal with high energy electrons. This means that the scattering angles for electron diffraction are small. Put in simple words, electrons will not end up away from the projection of the entrance point on the exit plane. The

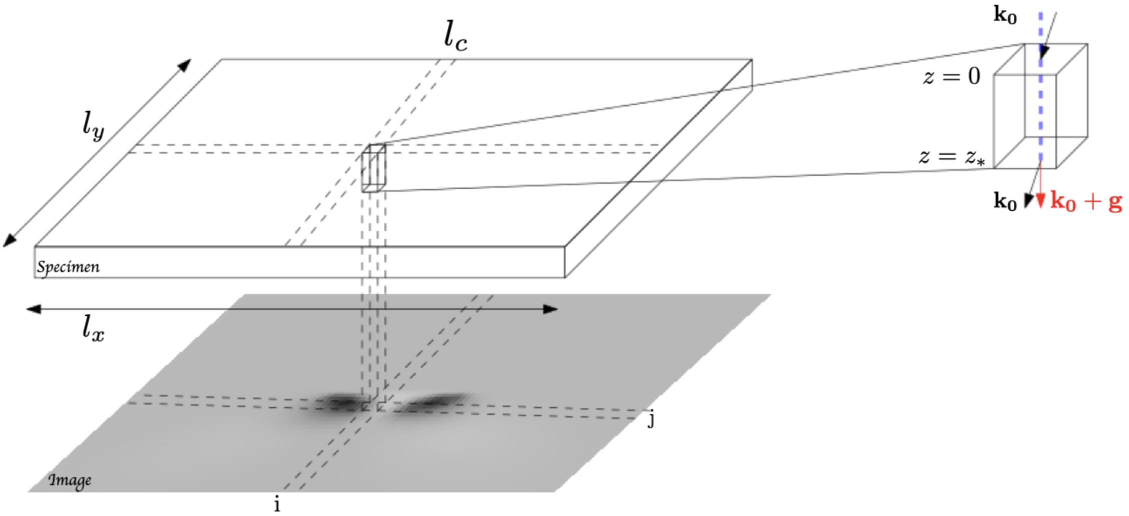

Figure 2.8: Column approximation: An incoming beam is assumed not to leave a column centered at the entering point. For this column, the intensity corresponding to the (i, j) pixel is obtained by propagating the beam along a line scan (blue line) in z-direction at position (x_i, y_j) to the exit plane.

diffraction angle becomes smaller with higher acceleration voltage. Because of this, M. Whelan and coworkers [WHHB57] introduced in 1957 the column approximation. The column approximation says that, due to the high energy, we can assume that an electron which enters the sample at one point will never leave a cylindrical column centered around the axis given by this point. In addition, it is assumed that electrons are not exchanged between columns. Then, we can solve the dynamical equations for each column in turn. We are now ready to understand how a TEM image is created. Imagine we have a rectangular specimen of horizontal dimensions l_y by l_x and vertical thickness z_*, see Figure 2.8. We divide this horizontal surface into squares of edge length l_c. We have that the total number of squares N created is:

$$N = \frac{l_y}{l_c} \times \frac{l_x}{l_c} = N_y \times N_x,$$

where N_y, N_x are the number of squares in the respective direction. Each square is the top of a column that we label by pairs (i, j). Then, a simulated TEM image is an array of $N_y \times N_x$ pixels, where every pixel (i, j) shows the intensity we calculated by solving the dynamical diffraction equations for that column, using as parameters the length of the column (which is the local thickness $z(i, j)$) and the orientation of the crystal along the column (which is described through the local excitation error $s_{\mathbf{g}}(i, j)$). Our final step is to use everything we learned until now and derive the equations that describe the electron propagation through the sample.

$\hbar = \frac{h}{2\pi}$	Planck's constant h divided by 2π
q	Elementary charge
E	Acceleration voltage
$\gamma = 1 + \frac{qE}{m_0 c_0^2}$	Relativistic mass ratio
$m = m_0\gamma$	Electron mass, where m_0 is electron rest mass
$\lambda_0 = h/\sqrt{2m_0 qE\left(1+\frac{qE}{2m_0 c_0^2}\right)}$	Electron wavelength
c_0	Speed of light

Table 2.1: Coefficients that appear in the Schrödinger Equations (2.13) and (2.14).

2.4 Dynamical electron scattering

We start with the *time-dependent Schrödinger* equation for the wave function $\psi(t, \mathbf{r})$:

$$\mathrm{i}\hbar\frac{\partial\psi(t,\mathbf{r})}{\partial t} = -\frac{\hbar^2}{2m}\Delta\psi(t,\mathbf{r}) - qV_{\mathrm{C}}(\mathbf{r})\psi(t,\mathbf{r}), \tag{2.13}$$

where V_{C} is a possibly complex periodic potential describing the electronic properties of the crystal. The rest of the coefficients are in Table 2.1. Looking for time-periodic solutions in the form $\psi(t,\mathbf{r}) = \mathrm{e}^{-\mathrm{i}4\pi^2\frac{\hbar}{2m}|\mathbf{k_0}|^2 t}\Psi(\mathbf{r})$ we obtain the *stationary Schrödinger* equation:

$$\Delta\Psi(\mathbf{r}) + (2\pi|\mathbf{k_0}|)^2\Psi(\mathbf{r}) = -4\pi^2\mathcal{U}(\mathbf{r})\Psi(\mathbf{r}), \tag{2.14}$$

where $\mathbf{k_0}$ is the wavevector of the incoming beam and $\mathcal{U}$ is the *reduced electrostatic potential* defined as $\mathcal{U}(\mathbf{r}) = \frac{2m_0 q}{\hbar^2}\gamma V_{\mathrm{C}}(\mathbf{r})$ with unit m^{-2}. The modulus of the wavevector is related to the (relativistic) wavelength by $|\mathbf{k_0}| = 1/\lambda_0$, with λ_0 given in Table 2.1.

We decompose $\mathbf{r} \in \mathbb{R}^d$ into an in-plane component $\mathbf{y} \in \mathbb{R}^{d-1}$ and a transversal component $z \in \mathbb{R}$, i.e. after rotating the coordinate axis we have $\mathbf{r} = (\mathbf{y}, z)$. The vertical coordinate $z \in [0, z_*]$ gives the depth inside the specimen, with $z = 0$ being the entry plane and $z = z_*$ the exit plane. To comply with physicists convention, the z direction is orientated roughly parallel to the electron beam. The outwards normal to the specimen at the exit plane $z = z_*$ is denoted by $\boldsymbol{\nu}$ and is assumed to be:

$$\boldsymbol{\nu} := (0, \ldots, 0, 1)^\top.$$

The direct lattice Λ and the dual lattice Λ^* are not necessarily aligned with one of the directions $\boldsymbol{\nu}$ or $\mathbf{k_0}$, but we always assume $\mathbf{k_0} \cdot \boldsymbol{\nu} > 0$, see Figure 2.9.

The column approximation restricts the focus to solutions of (2.14) that are exactly periodic in $\mathbf{y}$ and are slow modulations in z of a periodic profile in z. Hence, we seek solutions in the form:

$$\Psi(\mathbf{r}) = \Psi(\mathbf{y}, z) = \sum_{\mathbf{g}\in\Lambda^*} \psi_{\mathbf{g}}(z)\,\mathrm{e}^{\mathrm{i}\,2\pi\mathbf{k_0}\cdot\mathbf{r}}\,\mathrm{e}^{\mathrm{i}\,2\pi\mathbf{g}\cdot\mathbf{r}}, \tag{2.15}$$

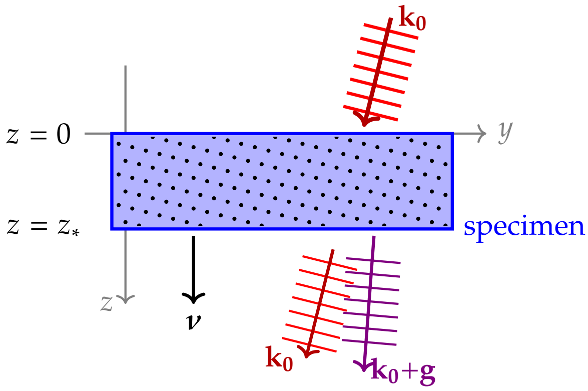

Figure 2.9: The incoming wave with wavevector $\mathbf{k}_0$ enters the specimen, is partially transmitted, and generates waves with nearby wavevectors $\mathbf{k}_0{+}\mathbf{g}$. Reprinted with permission from [KMM21, Fig. 1.1], published by the Society for Industrial and Applied Mathematics (SIAM). Copyright © by SIAM.

where $\psi_\mathbf{g}$ is the slowly varying envelope function of the beams in the directions of the vector $\mathbf{g} \in \Lambda^*$ (multi-beam ansatz). From a physics point of view, this multi-beam ansatz represents the diffraction of the incoming beam $\psi_\mathbf{0}$ in different discrete directions $\mathbf{g}$ (Bragg's law), given by the dual lattice. As was mentioned at the beginning of this chapter, the use of an objective aperture in TEM allows for restricting the set of transmitted beams forming the image in the microscope. Bright field and dark field imaging allow us to access the specific components $\psi_\mathbf{g}$ of the multi-beam ansatz.

The periodicity of the potential $\mathcal{U}$ is given by the direct lattice $\Lambda \subset \mathbb{R}^d$ via $\mathcal{U}(\mathbf{r}{+}\mathbf{q}) = \mathcal{U}(\mathbf{r})$ for all $\mathbf{r} \in \mathbb{R}^d$ and all lattice vectors $\mathbf{q} \in \Lambda$. With this, we are able to write $\mathcal{U}$ by its Fourier expansion $\mathcal{U}(\mathbf{r}) = \sum_{\mathbf{g}\in\Lambda^*} \mathrm{e}^{\mathrm{i}\,2\pi\mathbf{g}\cdot\mathbf{r}}\, U_\mathbf{g}$. Using the Fourier expansion of $\mathcal{U}$ we see that Ψ given in (2.15) solves the Schrödinger equation (2.14) if and only if the following system of ODEs is satisfied:

$$\begin{aligned}&\ddot{\psi}_\mathbf{g}(z) + \mathrm{i}4\pi\,\rho_\mathbf{g}\dot{\psi}_\mathbf{g}(z) + 4\pi^2\sigma_\mathbf{g}\psi_\mathbf{g}(z) = -4\pi^2 \sum_{\mathbf{h}\in\Lambda^*} U_{\mathbf{g}-\mathbf{h}}\psi_\mathbf{h}(z) \quad \text{for } \mathbf{g} \in \Lambda^*,\\ &\text{where } \rho_\mathbf{g} := (\mathbf{k}_0{+}\mathbf{g})\cdot\boldsymbol{\nu} \ \text{ and } \sigma_\mathbf{g} := |\mathbf{k}_0|^2 - |\mathbf{k}_0{+}\mathbf{g}|^2 = -|\mathbf{g}|^2{-}2\mathbf{k}_0\cdot\mathbf{g}.\end{aligned} \tag{2.16}$$

To simplify notation, we used the shorthand $\dot{\psi}_\mathbf{g}(z) = \partial_z\psi_\mathbf{g}(z) = \frac{\mathrm{d}}{\mathrm{d}z}\psi_\mathbf{g}(z)$. Recalling $\boldsymbol{\nu} = (0,\dots,1)^\top$, we see that $\rho_\mathbf{g}$ is positive for $\mathbf{g} \approx \mathbf{0}$, while $\sigma_\mathbf{g}$ changes sign in balls around $\mathbf{g} = \mathbf{0}$.

Next we use the fact that the variation in z is small such that $\partial_z^2\psi_\mathbf{g}$ is much smaller than typical values of $4\pi\rho_\mathbf{g}\partial_z\psi_\mathbf{g}$. Thus, we will neglect the second derivative (see Remark 2.4.1 for the justification) and are left with an infinite system of first-order ordinary differential equations, called *Darwin–Howie-Whelan (DHW) equation*, see e.g. [Dyc76, Eqn. (2.2.1)] or

[MNBL19, Eqn. (1)]:

$$\frac{\rho_{\mathbf{g}}}{\pi}\dot{\psi}_{\mathbf{g}}(z) - \mathrm{i}\sigma_{\mathbf{g}}\psi_{\mathbf{g}}(z) = \mathrm{i}\sum_{\mathbf{h}\in\Lambda^*} U_{\mathbf{g}-\mathbf{h}}\psi_{\mathbf{h}}(z) \quad \text{for } \mathbf{g}\in\Lambda^*. \tag{2.17}$$

Usually they are stated in the form:

$$\begin{aligned} &\dot{\psi}_{\mathbf{g}}(z) - 2\mathrm{i}\pi s_{\mathbf{g}}\psi_{\mathbf{g}}(z) = \mathrm{i}\frac{\pi}{\rho_{\mathbf{g}}}\sum_{\mathbf{h}\in\Lambda^*} U_{\mathbf{g}-\mathbf{h}}\psi_{\mathbf{h}}(z) \quad \text{for } \mathbf{g}\in\Lambda^*, \\ &\text{where } s_{\mathbf{g}} = \sigma_{\mathbf{g}}/(2\rho_{\mathbf{g}}) = \frac{|\mathbf{k}_0|^2 - |\mathbf{k}_0{+}\mathbf{g}|^2}{2(\mathbf{k}_0{+}\mathbf{g})\cdot\boldsymbol{\nu}} \text{ the excitation error.} \end{aligned} \tag{2.18}$$

However, we prefer (2.17) because of its mathematical symmetry structure. In experiments, the setup is done in such a way that the incoming beam, which will always be given by $\mathbf{g}=\mathbf{0}$, is diffracted in a few directions $\mathbf{k}_0{+}\mathbf{g}$ for $\mathbf{g}$ lying in a small subset Λ^*_m of Λ^*, where m is used to indicate the number of elements in Λ^*_m. Replacing Λ^* in (2.18) by Λ^*_m, we arrive at an m-beam model, which is an ODE for the vector $\boldsymbol{\psi} = (\psi_{\mathbf{g}})_{\mathbf{g}\in\Lambda^*_m} \in \mathbb{C}^m$ with the simple initial condition $\psi_{\mathbf{g}}(0) = \delta_{\mathbf{0},\mathbf{g}}$ (Kronecker symbol) for the incoming beam. Of special importance will be the:

$$\textit{two-beam model} \text{ with } \Lambda^*_2 = \{\mathbf{0}, \mathbf{g}'\},$$

which is widely used. From now on, we will denote by $\mathbf{g}'$ the diffracted beam in the two-beam approximation and by $\mathbf{g}_{\mathrm{ap}}$ the beam chosen by the objective aperture. For a bright field image we have $\mathbf{g}_{\mathrm{ap}} = \mathbf{0}$ and for a dark field image under two-beam approximation we have $\mathbf{g}_{\mathrm{ap}} = \mathbf{g}'$.

Taking a closer look on the derivation of the DHW equations, we notice that (2.18) for *all* $\mathbf{g}\in\Lambda^*$ is probably ill-posed, in particular, because of $\rho_{\mathbf{g}}$ changing sign and, even worse, becoming 0 or arbitrarily close to 0. It is clear that neglecting the term $\frac{1}{4\pi^2}\frac{\mathrm{d}^2}{\mathrm{d}z^2}\psi_{\mathbf{g}}(z)$ cannot be justified for such $\mathbf{g}$'s. Hence, one should realize that the DHW equation (2.18) is only useful for $\mathbf{g}$ where $\rho_{\mathbf{g}}$ is close to $\rho_{\mathbf{0}} = \mathbf{k}_0\cdot\boldsymbol{\nu} > 0$. The natural questions to occur are: What do we mean by close and how many beams are needed to obtain a reliable approximation for the solution of the Schrödinger equation, in particular for high-energy electron beams ($E \geq 100$ keV)?

These questions will be addressed in the next chapter, where we will investigate the reduction from the infinite lattice Λ^* to appropriate finite sets $\Lambda^*_m \subset \Lambda^*$.

Remark 2.4.1 (Justification of dropping $\partial_z^2\psi_{\mathbf{g}}$)**.** *In [Dyc76] the full Equation* (2.16) *including the second-order derivative with respect to z is abstractly written as:*

$$\frac{1}{4\pi^2}\ddot{\boldsymbol{\psi}} + \mathrm{i}R\dot{\boldsymbol{\psi}} + (\Sigma{+}\mathbb{U})\boldsymbol{\psi} = 0, \quad \boldsymbol{\psi} = (\psi_{\mathbf{g}})_{\mathbf{g}\in\mathbf{G}},$$

where $R = \mathrm{diag}\left(\frac{\rho_{\mathbf{g}}}{\pi}\right)_{\mathbf{g}\in\mathbf{G}}, \Sigma = \mathrm{diag}(\sigma_{\mathbf{g}})_{\mathbf{g}} \in \mathbf{G}$ *and* $\mathbb{U}\boldsymbol{\psi} = \left(\sum_{\mathbf{h}\in\mathbf{G}} U_{\mathbf{g}-\mathbf{h}}\psi_{\mathbf{h}}\right)_{\mathbf{g}\in\mathbf{G}}$. *The general solution can be written as the sum:*

$$\boldsymbol{\psi}(z) = \mathrm{e}^{M_1 z}C_1 + \mathrm{e}^{M_2 z}C_2, \quad \textit{where } \frac{1}{4\pi^2}M_j^2 + \mathrm{i}RM_j + (\Sigma{+}\mathbb{U})I = 0,$$

with potentially infinite matrices M_j *and vectors* C_j. *Unfortunately the set* $\mathbf{G} \subset \Lambda^*$ *of considered wavevectors is not specified. The boundary conditions are derived in [Dyc76, Sec. 2.4] from the free equations for* $z < 0$ *and* $z > z_*$ *(i.e.* $\mathbb{U} = 0$*) such that:*

$$\begin{aligned}
\boldsymbol{\psi}(0) &= \boldsymbol{\delta} + \boldsymbol{\psi}_{\text{reflect}}, & \frac{1}{2\pi^2}\dot{\boldsymbol{\psi}}(0) + \mathrm{i}R\boldsymbol{\psi}(0) &= \mathrm{i}R\boldsymbol{\delta} + \big(\mathrm{i}R+2\mathbb{S}'\big)\boldsymbol{\psi}_{\text{reflect}},\\
\boldsymbol{\psi}(z_*) &= \boldsymbol{\psi}_{\text{transm}}, & \frac{1}{2\pi^2}\dot{\boldsymbol{\psi}}(z_*) + \mathrm{i}R\boldsymbol{\psi}(z_*) &= \big(\mathrm{i}R+2\mathbb{S}\big)\boldsymbol{\psi}_{\text{transm}},
\end{aligned}$$

where $\mathbb{S}$ *and* $\mathbb{S}'$ *are suitable scattering matrices. It is then shown that* $\boldsymbol{\psi}(z)$ *differs from* $\boldsymbol{\psi}_{\text{DHW}}(z) = \mathrm{e}^{\mathrm{i}R^{-1}(\Sigma+\mathbb{U})z}\boldsymbol{\delta}$ *only by an amount that is proportional to* $1/|\mathbf{k_0}|$, *which is supposed to be negligible in most experimentally relevant cases.*

Chapter 3

On the Darwin–Howie–Whelan equations for the scattering of fast electrons

In the previous chapter, we introduced the Darwin-Howie-Whelan equations (2.17). They were derived from the Schrödinger equation (2.13) using Bragg's law (2.10) and the column approximation (2.15). Doing this step by step we ended up with a system for infinitely many beam amplitudes $\psi_{\mathbf{g}}$ with $\mathbf{g}$ running through the whole dual lattice Λ^*. In practice, for the numerical solution, we select a finite set $\Lambda^*_m \subset \Lambda^*$ of relevant beams, e.g. the classical two-beam approximation, see Section 3.4.3. The accuracy of such an approximation depends on the choice of Λ^*_m. The main goal of this chapter is to provide mathematical guidelines for optimal choices that are justified by exact error estimates. The results of this chapter are published in [KMM21] and the structure of the chapter follows closely the structure of that paper, with only a few changes in notation.

First, we write the equation in an appropriate form, see Section 3.1, in order to keep the symmetries related to self-adjointness of the Schrödinger equation, which will be useful for the analysis that follows, and we introduce the main structural assumptions for the coefficients (3.2). Once the setup is ready, we continue in Section 3.2 by defining two important sets of admissible beams Λ^{*M} and $\Lambda^{*\gamma}$, see (3.6). These sets are crucial for the analysis, because the DHW equation is well defined on them, as well as on any finite subset Λ^*_m. The mathematical analysis is then done in Section 3.3. We start by defining the appropriate Hilbert space with a corresponding norm and we prove existence and uniqueness of solutions in Proposition 3.3.1. In Section 3.3.2, we show that the solutions can be controlled by an exponentially weighted norm, see Theorem 3.3.4, using our main assumption that the Fourier coefficients of the potential decay exponentially, see (3.9). Using this result, we provide a first estimate between solutions in the sets of admissible beams, see Theorem 3.3.6, as well as any set $\Lambda^{*M} \subset \Lambda^*_{m_j} \subset \Lambda^{*\gamma}$, see Corollary 3.3.7. To further reduce the sets of beams, we use energy criteria in Section 3.3.4, that will allow us to split the set Λ^{*M} based on the size of the excitation error and lead us to a reduction on the Ewald sphere, see Theorem 3.3.10. Then in Section 3.4, we discuss special approximations that are commonly used in physics, like the two-beam approximation and the systematic-row approximation. The chapter ends with some numerical simulations in Section 3.5, where we relate the observed errors with the mathematical estimates developed before.

3.1 Setup of the model

First, we rewrite the equation (2.17) in a matrix-vector form for $\boldsymbol{\psi} = (\psi_{\mathbf{g}})_{\mathbf{g}\in\Lambda^*}$ and we get the system:

$$\begin{aligned} &R\dot{\boldsymbol{\psi}} = \mathrm{i}(\Sigma + \mathbb{U})\boldsymbol{\psi}, \text{ where} \\ &R = \operatorname{diag}\big(\tfrac{\rho_{\mathbf{g}}}{\pi}\big)_{\mathbf{g}\in\Lambda^*}, \quad \Sigma = \operatorname{diag}(\sigma_{\mathbf{g}})_{\mathbf{g}\in\Lambda^*}, \quad \mathbb{U}\boldsymbol{\psi} = \big(\textstyle\sum_{\mathbf{h}\in\Lambda^*} U_{\mathbf{g}-\mathbf{h}}\psi_{\mathbf{h}}\big)_{\mathbf{g}\in\Lambda^*} \end{aligned} . \tag{3.1}$$

Denoting by $\boldsymbol{\delta} := (\delta_{\mathbf{0},\mathbf{g}})_{\mathbf{g}\in\Lambda^*}$ the incoming beam, the solution $\boldsymbol{\psi}$ of the DHW equation can be written formally as $\boldsymbol{\psi}(z) = \mathrm{e}^{\mathrm{i}R^{-1}(\Sigma+\mathbb{U})z}\boldsymbol{\delta}$.

The following structural assumptions will be fundamental for the analysis:

$$\forall\, \mathbf{g} \in \Lambda^* : \quad \rho_{\mathbf{g}} \in \mathbb{R}, \quad \sigma_{\mathbf{g}} \in \mathbb{R}, \quad U_{-\mathbf{g}} = \overline{U}_{\mathbf{g}}. \tag{3.2}$$

Hence, the operator $\mathbb{U}$ is not only a simple convolution, but it is additionally Hermitian with respect to the standard complex scalar product. Modelling further effects, like dissipation via absorption or radiation, would break the Hermitian symmetry of $(U_{\mathbf{g}-\mathbf{h}})_{\mathbf{g},\mathbf{h}\in\Lambda^*}$.

The system (3.1) has a good structure because it keeps the symmetries related to self-adjointness of the Schrödinger equation. However, as is done in the physical literature it is often useful, e.g. for computational reasons, to write the system as an explicit first order equation in the form (2.18), which in a matrix form becomes:

$$\dot{\boldsymbol{\psi}} = \mathrm{i}(2\pi S + \mathbb{W})\boldsymbol{\psi} \quad \text{with } S = \operatorname{diag}(s_{\mathbf{g}})_{\mathbf{g}\in\Lambda^*} \text{ and } (\mathbb{W}\boldsymbol{\psi})_{\mathbf{g}} = \sum_{\mathbf{h}\in\Lambda^*} W_{\mathbf{g},\mathbf{h}}\,\psi_{\mathbf{h}}, \tag{3.3}$$
$$\text{where } s_{\mathbf{g}} = \sigma_{\mathbf{g}}/(2\rho_{\mathbf{g}}) \text{ and } W_{\mathbf{g},\mathbf{h}} = \pi U_{\mathbf{g}-\mathbf{h}}/\rho_{\mathbf{g}}.$$

In this form we see the *excitation errors* $s_{\mathbf{g}}$ which play a central role in TEM. They drive the phase of $\psi_{\mathbf{g}}(z) \in \mathbb{C}$ and can be interpreted as modulational wave numbers.

The multiplication by the inverse of the diagonal operator $R = \operatorname{diag}(\rho_{\mathbf{g}}/\pi)$, however, destroys two important properties of the operator $\mathbb{U}$. The scattering operator $\mathbb{W}$ is not described by a simple convolution anymore nor is it Hermitian. A serious problem then occurs because the factor $\rho_{\mathbf{g}} = (\mathbf{k}_0+\mathbf{g}) \cdot \boldsymbol{\nu}$ may become very small or even exactly 0.

This happens for $\mathbf{g}$ such that $\mathbf{k_0}+\mathbf{g}$ has no component in z-direction, i.e. the wave travels orthogonal to $\boldsymbol{\nu}$. Such waves are not relevant in TEM, and next we explain how $\mathbf{g}$ is restricted to exclude this case.

3.2 Sets of admissible beams

The fundamental observation is that the DHW equation for *all* $\mathbf{g} \in \Lambda^*$ is not really what is intended. The equation was derived with the aim to understand the behavior of $\psi_\mathbf{g}$ for $\mathbf{g}$ close to $\mathbf{g} = \mathbf{0}$, because in high-energy for reasonably thick specimens the diffraction remains small, i.e. we should only consider $\mathbf{g}$ with $|\mathbf{g}| \ll |\mathbf{k_0}|$.

Moreover, the assumption that the second derivative $\ddot{\psi}_\mathbf{g}$ can be dropped in comparison to the other terms $\rho_\mathbf{g}\dot{\psi}_\mathbf{g}$, $\sigma_\mathbf{g}\psi_\mathbf{g}$, and $(\mathbb{U}\boldsymbol{\psi})_\mathbf{g}$ is only justified if the excitation errors $s_\mathbf{g} = \sigma_\mathbf{g}/(2\rho_\mathbf{g})$ are small compared to 1. Indeed, if $\mathbb{U}$ is small with respect to $|\mathbf{k_0}|$, which will be one of our standing assumptions, then ignoring the term with the second derivative in the left-hand side of:

$$\frac{1}{4\pi\rho_\mathbf{g}}\ddot{\psi}_\mathbf{g} + \mathrm{i}\dot{\psi}_\mathbf{g} + 2\pi s_\mathbf{g}\psi_\mathbf{g} = -\frac{\pi}{\rho_\mathbf{g}}(\mathbb{U}\boldsymbol{\psi})_\mathbf{g} \tag{3.4}$$

leads to the explicit homogeneous solution $\psi_\mathbf{g}(z) = \mathrm{e}^{\mathrm{i}2\pi s_\mathbf{g} z}$. The term with the second derivative with respect to z is small relative to the other terms only if:

$$\begin{aligned} \Big|\frac{1}{4\pi\rho_\mathbf{g}}\ddot{\psi}_\mathbf{g}\Big| = \frac{\pi s_\mathbf{g}^2}{|\rho_\mathbf{g}|} \ \ll\ |\dot{\psi}_\mathbf{g}| + |2\pi\, s_\mathbf{g}\psi_\mathbf{g}| = 4\pi|s_\mathbf{g}| \\ \iff\ |s_\mathbf{g}| \ll |\rho_\mathbf{g}| \ \iff\ |\sigma_\mathbf{g}| \ll |\rho_\mathbf{g}|^2. \end{aligned} \tag{3.5}$$

An example of typical values of the left term $c^L_\mathbf{g}(z) = \big|\frac{1}{4\pi\rho_\mathbf{g}}\ddot{\psi}_\mathbf{g}(z)\big|$ and the right term $c^R_\mathbf{g}(z) = |\dot{\psi}_\mathbf{g}(z)| + |2\pi\, s_\mathbf{g}\psi_\mathbf{g}(z)|$ in the case of four beams is given Figure 3.1 and Table 3.1 for comparison. The four-beam simulation here is the same as the one in Section 3.5.

From now on, it will be essential that we restrict the DHW equation to a subset Λ^*_m that is part of the dual lattice Λ^*. Two classes of subsets will be used, for technical reasons and exact mathematical estimates, namely:

$$\Lambda^{*\gamma} := \big\{\, \mathbf{g} \in \Lambda^* \,\big|\, \rho_\mathbf{g} \geq \gamma\rho_\mathbf{0} \,\big\} \text{ and } \ \Lambda^{*M} := B_M(0) \cap \Lambda^* = \big\{\, \mathbf{g} \in \Lambda^* \,\big|\, |\mathbf{g}| \leq M \,\big\}. \tag{3.6}$$

Throughout we will assume $\gamma \in \,]0, 1[$, such that recalling $\rho_\mathbf{0} = \mathbf{k_0} \cdot \boldsymbol{\nu} > 0$ we see that $\Lambda^{*\gamma}$ lies above the hyperplane $\rho_\mathbf{g} = (\mathbf{k_0}+\mathbf{g})\cdot\boldsymbol{\nu} = 0$ and that $\mathbf{0} \in \Lambda^{*\gamma}$ because of $\gamma \leq 1$. While $\Lambda^{*\gamma}$ depends on $\mathbf{k_0}$ and contains infinitely many points, the set Λ^{*M} is finite and independent of $\mathbf{k_0}$. However, we will always assume $\Lambda^{*M} \subset \Lambda^{*\gamma}$ for some $\gamma > 0$, see Figure 3.2, then the possible values of M range from 0 to $\widehat{m}(\gamma, \mathbf{k_0}) \approx (1-\gamma)|\mathbf{k_0}|$. This way the DHW equation is well defined on the sets $\Lambda^{*\gamma}$ and Λ^{*M}, as well as on any finite subset Λ^*_m.

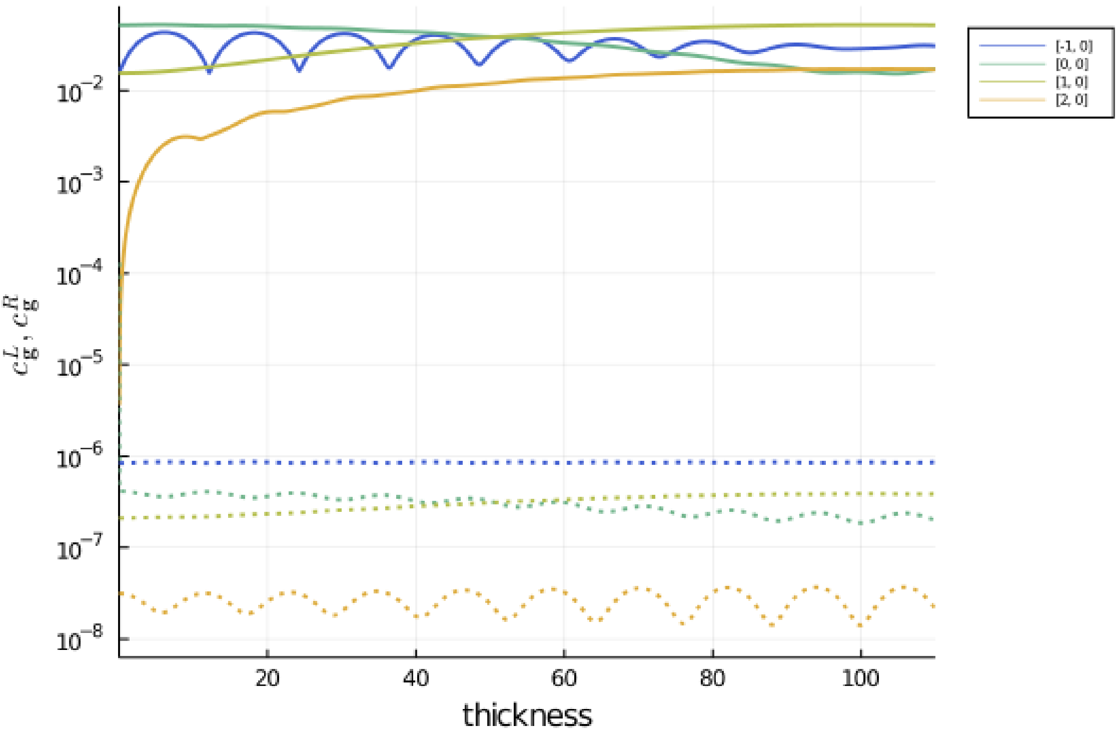

Figure 3.1: Plot of $c^L_{\mathbf{g}} = |\frac{1}{4\pi\rho_{\mathbf{g}}}\ddot{\psi}_{\mathbf{g}}(z)|$ (dotted lines) and $c^R_{\mathbf{g}} = |\dot{\psi}_{\mathbf{g}}(z)| + |2\pi\, s_{\mathbf{g}}\psi_{\mathbf{g}}(z)|$ (solid lines) in logarithmic scale for comparison. The simulation was done for the four beams indicated by the colors.

z	$\mathbf{g} = (-1,0)$	$\mathbf{g} = (0,0)$	$\mathbf{g} = (1,0)$	$\mathbf{g} = (2,0)$
20	0.0399943197	0.0499849218	0.0217044982	0.0058000188
40	0.0363582533	0.0435270409	0.0327706370	0.0099685772
60	0.0223780703	0.0331279555	0.0427286059	0.0136603201
80	0.0337702160	0.0225037398	0.0494867897	0.0162111446

z	$\mathbf{g} = (-1,0)$	$\mathbf{g} = (0,0)$	$\mathbf{g} = (1,0)$	$\mathbf{g} = (2,0)$
20	0.0000008562	0.0000003629	0.0000002329	0.0000000258
40	0.0000008574	0.0000003219	0.0000000283	0.0000000177
60	0.0000008574	0.0000003219	0.0000002838	0.0000000177
80	0.0000008508	0.0000002391	0.0000003708	0.0000003214

Table 3.1: Values of the term c^R (top table) and c^L (bottom table) for the four beam simulation shown in Figure 3.1.

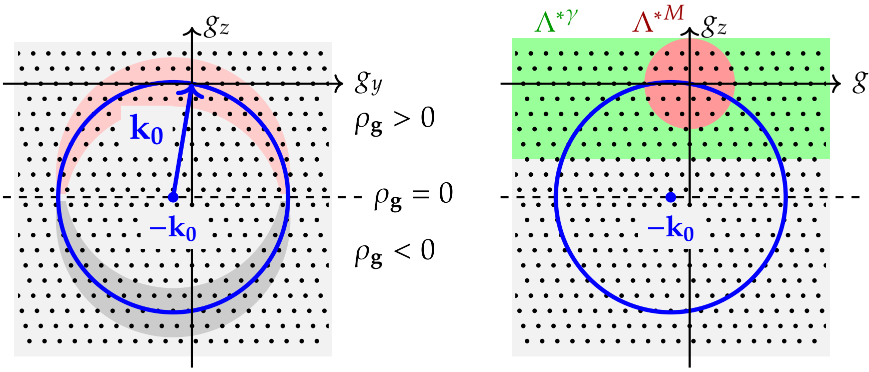

Figure 3.2: Ewald sphere $\mathbb{S}_{\mathrm{Ew}}$ (blue) is shown together with the points of the dual lattice. Left: The areas around the Ewald sphere show the regions where $|\sigma_{\mathbf{g}}| \leq 0.1\,|\rho_{\mathbf{g}}|^2$. Only the upper half with $\rho_{\mathbf{g}} > 0$ is relevant for the DHW equation. Right: The sets $\Lambda^{*\gamma}$ and Λ^{*M} lie above the hyperplane $\rho_{\mathbf{g}} = \mathbf{0}$ and contain $\mathbf{g} = 0$. Reprinted with permission from [KMM21, Fig. 2.2], published by the Society for Industrial and Applied Mathematics (SIAM). Copyright © by SIAM.

From now on, we will use the shorthand "$\mathrm{DHW}_{\Lambda^*_m}$" to denote the DHW equation, where the choice of wave vectors $\mathbf{g}$ is restricted to Λ^*_m, while all other $\psi_{\mathbf{h}}$ are ignored, i.e. we set $\psi_{\mathbf{h}} \equiv 0$ for $\mathbf{h} \notin \Lambda^*_m$:

$$\mathrm{DHW}_{\Lambda^*_m}: \qquad \mathrm{i}\,\frac{\rho_{\mathbf{g}}}{\pi}\,\dot{\psi}_{\mathbf{g}} + \sigma_{\mathbf{g}}\psi_{\mathbf{g}} = -\sum_{\mathbf{h}\in\Lambda^*_m} U_{\mathbf{g}-\mathbf{h}}\psi_{\mathbf{h}} \quad \text{for } \mathbf{g} \in \Lambda^*_m. \tag{3.7}$$

We will write this equation also in the compact form:

$$R_{\Lambda^*_m}\dot{\boldsymbol{\psi}} = \mathrm{i}\left(\Sigma_{\Lambda^*_m} + \mathbb{U}_{\Lambda^*_m}\right)\boldsymbol{\psi} \quad \text{for } \boldsymbol{\psi} = (\psi_{\mathbf{g}})_{\mathbf{g}\in\Lambda^*_m}.$$

However, whenever possible without creating confusion, we will drop the subscript Λ^*_m and simply write R, Σ, and $\mathbb{U}$. Throughout we will assume that $\mathbf{0} \in \Lambda^*_m \subset \Lambda^{*\gamma} \subset \Lambda^*$ for some $\gamma \in\,]0,1[$. Our estimates below will show that the difference in solutions for different sets $\Lambda^*_{m_1}$ and $\Lambda^*_{m_2}$ will be negligible as long as (i) they both contain a suitable ball $B_M(0) \cap \Lambda^*$ around $\mathbf{g} = \mathbf{0}$, (ii) they are both contained in $\Lambda^{*\gamma}$ for some $\gamma \in\,]0,1[$, and (iii) as long as z_* is not too big, see Corollary 3.3.7.

3.3 Mathematical estimates

Next, we will replace the infinite system (3.3) by a finite-dimensional one. First we insert a beam that uses very few modes, usually one or two. This means that the initial condition $\boldsymbol{\psi}(0)$ is strongly localized in the wave-vector space near $\mathbf{g} = \mathbf{0}$. Moreover, we may assume that the scattering kernel $U_{\mathbf{g}-\mathbf{h}}$ decays exponentially in the distance $|\mathbf{g} - \mathbf{h}|$. Then, in Section 3.3.2 we will show that the solution $\boldsymbol{\psi}(z)$ remains localized on Λ^* around the initial beams for all $z \in [0, z_*]$. Thus, we can show that cutting away modes with $|\mathbf{g}| > M$, we obtain an error that decays like $\mathrm{e}^{-\lambda M}$ with $\lambda > 0$.

The first result concerns the preservation of a specific quadratic form that can be used as a norm if we restrict the system to a region in Λ^* where $\rho_{\mathbf{g}} > 0$. An additional reduction of the number of relevant modes is discussed in Section 3.3.4. It concerns averaging effects that occur by large excitation errors $s_{\mathbf{g}} = \sigma_{\mathbf{g}}/(2\rho_{\mathbf{g}})$. For this we use the Ewald sphere as defined in (2.11):

$$\mathbb{S}_{\mathrm{Ew}} := \left\{ \mathbf{g} \in \mathbb{R}^d \,\middle|\, |\mathbf{k_0}+\mathbf{g}|^2 = |\mathbf{k_0}|^2 \right\}.$$

For wave vectors $\mathbf{g} \in \Lambda^*$ lying on or near $\mathbb{S}_{\mathrm{Ew}}$ the excitation error $s_{\mathbf{g}}$ is 0 or small, respectively. The condition $s_{\mathbf{g}} = 0$ means that the Bragg condition for diffraction holds.

However, for $\mathbf{g}$ lying far way from $\mathbb{S}_{\mathrm{Ew}}$ we have $|s_{\mathbf{g}}| \geq s_* \gg 1$, which leads to fast oscillations that make the amplitudes of these modes small.

3.3.1 Conservation of norms

We now turn to the analysis of the DHW equation (3.7) for a subset Λ^*_m which may be a system of finite or of infinitely many coupled linear ODEs. One major impact of restriction to $\Lambda^*_m \subset \Lambda^{*\gamma}$ lies in the fact that *all* $\rho_{\mathbf{g}}$ are now positive. Thus, we can introduce the norm:

$$\|\psi\|_{\Lambda^*_m} := \Big(\sum_{\mathbf{g}\in\Lambda^*_m} \rho_{\mathbf{g}}\, |\psi_{\mathbf{g}}|^2 \Big)^{1/2} = \Big(\big\langle \pi R \boldsymbol{\psi}, \boldsymbol{\psi} \big\rangle \Big)^{1/2}$$

The square $\|\boldsymbol{\psi}\|^2_{\Lambda^*_m}$ can be related to the wave flux in the static Schrödinger equation, see Remark 3.3.2. We define the Hilbert spaces:

$$\mathfrak{H}(\Lambda^*_m) := \left\{ A \in \ell^2(\Lambda^*_m) \,\middle|\, \|A\|_{\Lambda^*_m} < \infty \right\} \text{ with scalar product } \big\langle A, B \big\rangle_{\Lambda^*_m} := \sum_{\mathbf{g}\in\Lambda^*_m} \rho_{\mathbf{g}}\, A_{\mathbf{g}} \overline{B}_{\mathbf{g}}.$$

The following classical result states the existence and uniqueness of solutions for $\mathrm{DHW}_{\Lambda^*_m}$ together with the property that the associated evolution preserves the Hilbert-space norm as well as the energy norm.

Proposition 3.3.1 (Existence, uniqueness, and conservation of norms). *Assume that* $\rho_{\mathbf{g}}$ *and* $\sigma_{\mathbf{g}}$ *are given as in* (2.16) *and that* $\mathbb{U} = (U_{\mathbf{g}-\mathbf{h}})$ *satisfies* $U_{-\mathbf{g}} = \overline{U}_{\mathbf{g}}$ *and* $|U_{\mathbf{g}}| \leq C_{\mathbb{U}} < \infty$. *Then,* $\mathrm{DHW}_{\Lambda^*_m}$ *as given in* (3.7) *has for each* $\boldsymbol{\psi}(0) \in \mathfrak{H}(\Lambda^*_m)$ *a unique solution* $\boldsymbol{\psi} \in \mathrm{C}^0(\mathbb{R}; \mathfrak{H}(\Lambda^*_m))$. *Moreover, the solution satisfies:*

$$\|\boldsymbol{\psi}(z)\|^2_{\Lambda^*_m} = \|\boldsymbol{\psi}(0)\|^2_{\Lambda^*_m} \quad \text{and} \quad \|H\boldsymbol{\psi}(z)\|^2_{\Lambda^*_m} = \|H\boldsymbol{\psi}(0)\|^2_{\Lambda^*_m} \qquad \text{for all } z \in \mathbb{R}, \tag{3.8}$$

where $H = R^{-1}(\Sigma+\mathbb{U})$.

Proof. The result is a direct consequence of the standard theory of the generation of strongly continuous, unitary groups $\mathrm{e}^{\mathrm{i}zH}$, where $H = R^{-1}(\Sigma+\mathbb{U})$ is self-adjoint on $\mathfrak{H}(\Lambda^*_m)$ equipped with the scalar product $\langle\cdot,\cdot\rangle_{\Lambda^*_m}$. □

The following remark shows that the conservation of the norm $\|\boldsymbol{\psi}\|_{\Lambda^*_m}$ is not related to the classical mass conservation in the Schrödinger equation, but should be interpreted as a wave-flux conservation, which is only approximately true in the Schrödinger equation, but becomes exact under the DHW approximation, i.e. by ignoring the term involving $\frac{\mathrm{d}^2}{\mathrm{d}z^2}\psi_{\mathbf{g}}$ in (3.4).

Remark 3.3.2 (Wave flux in the static Schrödinger equation)**.** *For general solutions $\psi(t,\mathbf{r})$ of the time-dependent Schrödinger equation (2.13), we can introduce the probability density $\varrho(t,\mathbf{r}) = |\psi(t,\mathbf{r})|^2$ and obtain the conservation law*

$$\frac{\partial\rho}{\partial t} + \operatorname{div}\mathbf{J} = -\frac{2q}{\hbar}\operatorname{Im}(V_{\mathrm{C}})\rho \quad \textit{with } \mathbf{J} = \frac{\hbar}{m}\operatorname{Im}\left(\overline{\psi}\,\nabla\psi\right) \in \mathbb{R}^d,$$

where $\mathbf{J}$ is called electron-flux vector, see e.g. [De 03, p.125]. Because of our assumption (3.2), we have $\operatorname{Im}(V_{\mathrm{C}}) \equiv 0$, such that for solutions Ψ of the static Schrödinger equation the electron flux satisfies $\operatorname{div}\mathbf{J} \equiv 0$.

Moreover, by column approximation (2.15) $\Psi(\mathbf{r}) = \Psi(\mathbf{y},z)$ is exactly periodic in $\mathbf{y} = (y_1,\dots,y_{d-1})$ and a slowly varying periodic function in z. We denote by $\mathcal{P} = \mathcal{P}'_y{\times}[0,a_0] \subset \mathbb{R}^d$ the periodicity cell of the crystal, where a_0 is the lattice constant. Choosing $z_1, z_2 \in [0,z_*]$ and recalling $\boldsymbol{\nu} = (0,\dots,0,1)^\top$, the divergence theorem gives:

$$\begin{aligned} 0 &= \int_{z_1}^{z_2}\int_{(0,z)+\mathcal{P}} \operatorname{div}\mathbf{J}\,\mathrm{d}\mathbf{r}\,\mathrm{d}z = \int_{z_1}^{z_2}\int_{(0,z)+\partial\mathcal{P}} \mathbf{J}\cdot\hat{n}\,\mathrm{d}a\,\mathrm{d}z \\ &= \int_{z_1}^{z_2}\Big(\int_{\mathcal{P}_y\times\{z+a_0\}} \mathbf{J}\cdot\boldsymbol{\nu}\,\mathrm{d}a - \int_{\mathcal{P}_y\times\{z\}} \mathbf{J}\cdot\boldsymbol{\nu}\,\mathrm{d}a\Big)\,\mathrm{d}z = \int_{(0,z_2)+\mathcal{P}} \mathbf{J}\cdot\boldsymbol{\nu}\,\mathrm{d}\mathbf{r} - \int_{(0,z_1)+\mathcal{P}} \mathbf{J}\cdot\boldsymbol{\nu}\,\mathrm{d}\mathbf{r}. \end{aligned}$$

Thus, we conclude that the wave flux $\mathrm{WF}(z)$ is independent of $z \in [0,z_*]$, where:

$$\mathrm{WF}(z) := \int_{(0,z)+\mathcal{P}} \mathbf{J}\cdot\boldsymbol{\nu}\,\mathrm{d}\mathbf{r} = \frac{\hbar}{m}\int_{(0,z)+\mathcal{P}} \operatorname{Im}\left(\overline{\Psi}\frac{\partial}{\partial z}\Psi\right)\mathrm{d}\mathbf{r}.$$

Inserting the Fourier expansion (2.15) into $\operatorname{Im}\left(\overline{\Psi}\frac{\partial}{\partial z}\Psi\right)$ we find that:

$$\begin{aligned} \frac{m}{\hbar}\mathrm{WF}(z) &= \int_{(0,z)+\mathcal{P}} \operatorname{Im}\left(\overline{\Psi}(y,\hat{z})\frac{\partial}{\partial\hat{z}}\Psi(y,\hat{z})\right)\mathrm{d}(y,\hat{z}) \\ &= \sum_{\mathbf{g}\in\Lambda^*} \operatorname{Im}\Big(\overline{\psi}_{\mathbf{g}}(z)\left(\dot{\psi}_{\mathbf{g}}(z) + \mathrm{i}\,2\pi(\mathbf{k_0}{+}\mathbf{g})\psi_{\mathbf{g}}(z)\right)\Big) \\ &= 2\pi\sum_{\mathbf{g}\in\Lambda^*}(\mathbf{k_0}{+}\mathbf{g})|\psi_{\mathbf{g}}(z)|^2 \;+\; \sum_{\mathbf{g}\in\Lambda^*}\operatorname{Im}\left(\overline{\psi}_{\mathbf{g}}(z)\,\dot{\psi}_{\mathbf{g}}(z)\right). \end{aligned}$$

We see that the first sum corresponds to our conserved norm $\|\boldsymbol{\psi}(z)\|^2_{\Lambda^*_m}$ if the contributions of $\psi_{\mathbf{g}}(z)$ for $\mathbf{g} \in \Lambda^*\backslash\Lambda^*_m$ are negligible. The second sum is much smaller than the first sum, because of our assumption of slowly varying amplitudes, namely $|\dot{\psi}_{\mathbf{g}}| \ll |\mathbf{k_0}\psi_{\mathbf{g}}|$, see (3.5).

Remark 3.3.3 (Dissipative version of the DHW equation)**.** *Often the system* (2.18) *or* (3.3) *is modified on a phenomenological level to account for dissipative effects like absorption by making* V_{C} *complex. Hence,* $U_{\mathbf{g}}$ *is replaced by* $U_{\mathbf{g}} + \mathrm{i}U'_{\mathbf{g}}$ *with a suitable* $U'_{\mathbf{g}}$*. Under this assumption, the above flux conservation is no longer true, but for most modeling choices (e.g. in the case that* $(U'_{\mathbf{g}-\mathbf{h}})_{\mathbf{g},\mathbf{h}\in\Lambda^*_m}$ *is negative definite) one can achieve the estimate* $\|\boldsymbol{\psi}(z)\|^2_{\Lambda^*_m} \le \|\boldsymbol{\psi}(0)\|^2_{\Lambda^*_m}$ *for* $z \ge 0$*, i.e. the wave flux decays.*

3.3.2 Exponential decay of modes

We first show that the solutions can be controlled in an exponentially weighted norm $\|\cdot\|_\alpha$ with $\alpha \in \mathbb{R}$, where the case $\alpha = 0$ would correspond to the usual norm $\|\cdot\|_{\Lambda^*_m}$ in $\mathfrak{H}(\Lambda^*_m)$. We define:

$$\|\boldsymbol{\psi}\|^2_\alpha := \sum_{\mathbf{g}\in\Lambda^*} \mathrm{e}^{2\alpha|\mathbf{g}|}\rho_{\mathbf{g}}|\psi_{\mathbf{g}}|^2.$$

Introducing this norm will destroy the Hamiltonian structure of the system.

Our main assumption is that the potential operator $\mathbb{U}$ acts in such a way that the Fourier coefficients have exponential decay, namely:

$$\exists\, C_{\mathbb{U}} > 0,\ \alpha_{\mathbb{U}} > 0\ \forall\, \mathbf{g} \in \Lambda^* : \quad |U_{\mathbf{g}}| \le C_{\mathbb{U}}\,\mathrm{e}^{-\alpha_{\mathbb{U}}|\mathbf{g}|}. \tag{3.9}$$

Indeed, the scattering potential can be approximated by:

$$U_{\mathbf{g}} \propto \sum_{\nu} f_\nu(\mathbf{g})\mathrm{e}^{2\pi i\mathbf{g}\cdot\mathbf{x}_\nu}\mathrm{e}^{-M_\nu|\mathbf{g}|^2}, \tag{3.10}$$

where $\mathbf{x}_\nu$ denotes the position of the atom ν in the unit cell, f_ν the atomic scattering factors, and $M_\nu > 0$ is the Debye-Waller factor, see [WK91] and [SRTL09], respectively. The symbol $\propto$ indicates proportionality. Thus, assumption (3.9) is automatically satisfied. Figure 3.3 gives an example for GaAs.

With this assumption, we are now able to control the size of the solutions of (3.3) in the weighted norm if $|\alpha| < \alpha_{\mathbb{U}}$. In the following result, α may be positive or negative, but later on we are interested in $\alpha > 0$.

Theorem 3.3.4 (Weighted norms)**.** *Consider the* $\mathrm{DHW}_{\Lambda^*_m}$ *as in* (3.7) *with* $\Lambda^*_m \subset \Lambda^{*\gamma} \subset \Lambda^*$ *with* $\gamma \in\ ]0,1[$*. Moreover, assume that* $\mathcal{U}$ *satisfies* (3.9)*. Then, for all* $\alpha \in\ ]-\alpha_{\mathbb{U}}, \alpha_{\mathbb{U}}[$ *and all initial conditions* $\boldsymbol{\psi}^0 \in \mathfrak{H}(\Lambda^*_m)$ *with* $\|\boldsymbol{\psi}^0\|_\alpha < \infty$ *the unique solution* $\boldsymbol{\psi}$ *of* (3.7) *with* $\boldsymbol{\psi}(0) = \boldsymbol{\psi}^0$ *satisfies the estimate:*

$$\|\boldsymbol{\psi}(z)\|_\alpha \le \mathrm{e}^{\kappa(\alpha)|z|}\|\boldsymbol{\psi}^0\|_\alpha \quad \text{for } z \in \mathbb{R}, \tag{3.11}$$

where the exponential growth rate $\kappa(\alpha)$ *is explicitly given by:*

$$\kappa(\alpha) = \frac{\pi C_{\mathbb{U}}}{\gamma\rho_0}\,|\alpha|\,\mathfrak{S}_1(\alpha_{\mathbb{U}}-|\alpha|), \quad \text{where } \mathfrak{S}_m(\beta) := \sum_{\varkappa\in\Lambda^*} |\varkappa|^m\mathrm{e}^{-\beta|\varkappa|}.$$

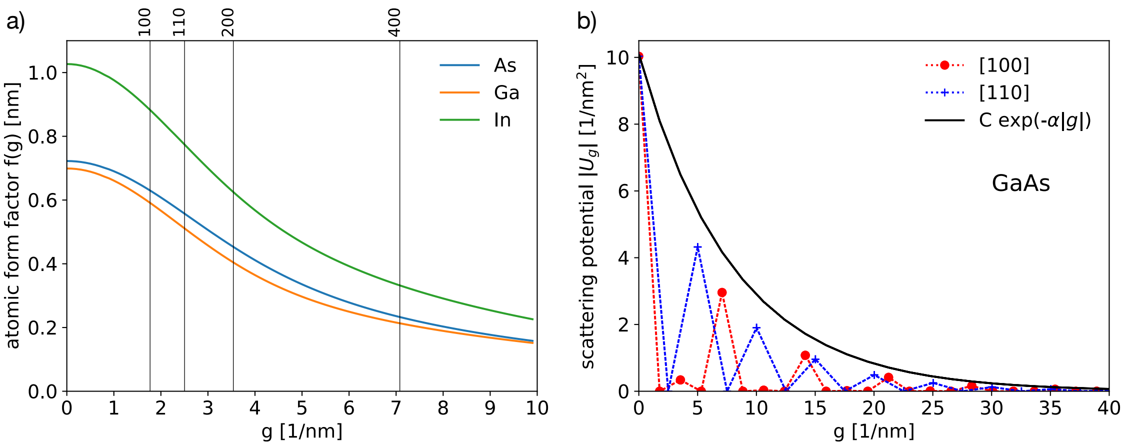

Figure 3.3: Atomic form factors and scattering potential: (a) atomic form factors in dependence on the wave vector $\mathbf{g}$ for Ga, As, and In following [WK91]. The vertical lines indicate positions of the lattice planes (100), (110), (200) and (400) in GaAs. (b) Fourier coefficients of the scattering potential for GaAs along the [100]- (red) and [110]-crystallographic directions (blue) as computed by pyTEM [Nie19] using (3.10). The blue and red lines are only for guiding of the eye. An exponential decay (solid black) as assumed in (3.9) can be observed with $C = 10.1\,1/\mathrm{nm}^2$ and $\alpha = 0.125$ nm. Reprinted with permission from [KMM21, Fig. 3.1], published by the Society for Industrial and Applied Mathematics (SIAM). Copyright © by SIAM.

Proof. Step 1. Transformation of the equation: We introduce the new variables $B_{\mathbf{g}} = \mathrm{e}^{\alpha|\mathbf{g}|}\psi_{\mathbf{g}}$ such that $\|\boldsymbol{\psi}\|_\alpha = \|B\|_{\Lambda^*_m}$. In terms of B we can rewrite DHW$_{\Lambda^*_m}$ as:

$$\mathrm{i}R\dot{B} + \Sigma B = -\mathbb{U}^{(\alpha)}B = -\mathbb{U}B + \mathbb{P}^{(\alpha)}B \quad \text{with } \mathbb{P}^{(\alpha)}_{\mathbf{g},\mathbf{h}} = \big(1-\mathrm{e}^{\alpha(|\mathbf{g}|-|\mathbf{h}|)}\big)U_{\mathbf{g}-\mathbf{h}}. \tag{3.12}$$

Here, we used that R and Σ are diagonal operators, and hence commute with the multiplication of the exponential factor. Using the bound (3.9) for $U_{\mathbf{g}}$, the coefficients of the perturbation operator $\mathbb{P}^{(\alpha)}$ can be bounded by:

$$|\mathbb{P}^{(\alpha)}_{\mathbf{g},\mathbf{h}}| \le C_{\mathbb{U}}\big(1-\mathrm{e}^{|\alpha|\,|\mathbf{g}-\mathbf{h}|}\big)\mathrm{e}^{-\alpha_{\mathbb{U}}|\mathbf{g}-\mathbf{h}|} \le C_{\mathbb{U}}\,\min\{1,|\alpha|\,|\mathbf{g}-\mathbf{h}|\}\,\mathrm{e}^{-(\alpha_{\mathbb{U}}-|\alpha|)|\mathbf{g}-\mathbf{h}|}. \tag{3.13}$$

Step 2. Operator norm of $R^{-1}\mathbb{P}^{(\alpha)}$ in $\mathfrak{H}(\Lambda^*_m)$. To control the perturbation $R^{-1}\mathbb{P}^{(\alpha)}B$ in terms of $\|B\|_{\Lambda^*_m}$, we employ Lemma 3.3.5 to obtain $\|R^{-1}\mathbb{P}^{(\alpha)}B\|_{\Lambda^*_m} \le C^{(\alpha)}_{\mathbb{P}}\|B\|_{\Lambda^*_m}$ with:

$$C^{(\alpha)}_{\mathbb{P}} := \Big(\sup_{\mathbf{g}\in\Lambda^*_m}\sum_{\mathbf{h}\in\Lambda^*_m}\frac{\pi|\mathbb{P}^{(\alpha)}_{\mathbf{g},\mathbf{h}}|}{|\rho_{\mathbf{g}}\rho_{\mathbf{h}}|^{1/2}}\Big)^{1/2}\Big(\sup_{\mathbf{h}\in\Lambda^*_m}\sum_{\mathbf{g}\in\Lambda^*_m}\frac{\pi|\mathbb{P}^{(\alpha)}_{\mathbf{g},\mathbf{h}}|}{|\rho_{\mathbf{g}}\rho_{\mathbf{h}}|^{1/2}}\Big)^{1/2}.$$

Because of $\rho_{\mathbf{g}}, \rho_{\mathbf{h}} \in \Lambda^*_m \subset \Lambda^{*\gamma}$, and (3.13) this yields:

$$C^{(\alpha)}_{\mathbb{P}} \le \pi C_{\mathbb{U}}\sup_{\mathbf{g}\in\Lambda^*_m}\sum_{\mathbf{h}\in\Lambda^*_m}\frac{|\alpha|\,|\mathbf{g}-\mathbf{h}|}{\gamma\rho_0}\,\mathrm{e}^{-(\alpha_{\mathbb{U}}-|\alpha|)|\mathbf{g}-\mathbf{h}|} \le \frac{\pi C_{\mathbb{U}}}{\gamma\rho_0}\,|\alpha|\,\mathfrak{S}_1(\alpha_{\mathbb{U}}-\alpha) = \kappa(\alpha).$$

Step 3. Gronwall estimate. We now apply the variation-of-constants formula (Duhamel's principle) to the solution B for (3.12) in the $\mathfrak{H}(\Lambda^*_m)$, where $H = R^{-1}(\Sigma - \mathbb{U})$ is the generator of the norm-preserving C_0 group $\mathrm{e}^{\mathrm{i}zH}$:

$$\begin{aligned}\|B(z)\|_{\Lambda^*_m} &\leq \|\mathrm{e}^{iHz}B(0)\|_{\Lambda^*_m} + \int_0^z \|\mathrm{e}^{i(z-\zeta)H}\|_{\Lambda^*_m}\|R^{-1}\mathbb{P}^{(\alpha)}B(\zeta)\|_{\Lambda^*_m}\,\mathrm{d}\zeta \\ &\leq \|\boldsymbol{\psi}(0)\|_\alpha + \int_0^z \kappa(\alpha)\,\|B(\zeta)\|_{\Lambda^*_m}\,\mathrm{d}\zeta.\end{aligned}$$

Now, Gronwall's estimate gives $\|\boldsymbol{\psi}(z)\|_\alpha = \|B(z)\|_{\Lambda^*_m} \leq \mathrm{e}^{\kappa(\alpha)z}\|\boldsymbol{\psi}(0)\|_\alpha$, and the proof is completed. □

Step 2 of the above proof relies on the following elementary lemma, which will be used again to calculate the norm of convolution-type operators involving $\mathbb{U}$.

Lemma 3.3.5 (Operator norm). *Consider* $\Lambda^*_{m_1}, \Lambda^*_{m_2} \subset \Lambda^{*\gamma}$ *with* $\gamma > 0$ *and* $\mathbb{B} : \mathfrak{H}(\Lambda^*_{m_1}) \to \mathfrak{H}(\Lambda^*_{m_2})$ *with* $(\mathbb{B}A)_{\mathbf{g}} = \sum_{\mathbf{h}\in\Lambda^*_{m_1}} B_{\mathbf{gh}}A_{\mathbf{h}}$. *Setting* $\widetilde{B}_{\mathbf{gh}} = \sqrt{\rho_{\mathbf{g}}/\rho_{\mathbf{h}}}\,B_{\mathbf{gh}}$ *gives:*

$$\|\mathbb{B}A\|_{\Lambda^*_{m_2}} \leq C_{\mathbb{B}}\|A\|_{\Lambda^*_{m_1}}, \quad C_{\mathbb{B}} = \Big(\sup_{\mathbf{h}\in\Lambda^*_{m_1}}\sum_{\mathbf{g}\in\Lambda^*_{m_2}}|\widetilde{B}_{\mathbf{gh}}|\Big)^{1/2}\Big(\sup_{\mathbf{g}\in\Lambda^*_{m_2}}\sum_{\mathbf{h}\in\Lambda^*_{m_1}}|\widetilde{B}_{\mathbf{gh}}|\Big)^{1/2}, \tag{3.14}$$

which is the square root of the product of the row-sum and column-sum norm.

Proof. With $r_{\mathbf{g}} = \rho_{\mathbf{g}}^{1/2}$ the desired result is obtained as follows:

$$\begin{aligned}\|\mathbb{B}A\|^2_{\Lambda^*_{m_2}} &= \sum_{\mathbf{g}\in\Lambda^*_{m_2}} r_{\mathbf{g}}^2\Big(\sum_{\mathbf{h}\in\Lambda^*_{m_1}} B_{\mathbf{gh}}A_{\mathbf{h}}\Big)\overline{(\mathbb{B}A)}_{\mathbf{g}} \leq \sum_{\mathbf{g}\in\Lambda^*_{m_2}}\sum_{\mathbf{h}\in\Lambda^*_{m_1}} r_{\mathbf{h}}|\widetilde{B}_{\mathbf{gh}}|^{1/2}|A_{\mathbf{h}}|r_{\mathbf{g}}|\widetilde{B}_{\mathbf{gh}}|^{1/2}|(\mathbb{B}A)_{\mathbf{g}}| \\ &\leq_{\text{CaSch}} \Big(\sum_{\mathbf{g}\in\Lambda^*_{m_2}}\sum_{\mathbf{h}\in\Lambda^*_{m_1}}|\widetilde{B}_{\mathbf{gh}}|\,r_{\mathbf{h}}^2|A_{\mathbf{h}}|^2\Big)^{1/2}\Big(\sum_{\mathbf{g}\in\Lambda^*_{m_2}}\sum_{\mathbf{h}\in\Lambda^*_{m_1}}|\widetilde{B}_{\mathbf{gh}}|\,r_{\mathbf{g}}^2|(\mathbb{B}A)_{\mathbf{g}}|^2\Big)^{1/2} \\ &\leq \Big(\sup_{\mathbf{h}\in\Lambda^*_{m_1}}\Big(\sum_{\mathbf{g}\in\Lambda^*_{m_2}}|\widetilde{B}_{\mathbf{gh}}|\Big)\Big)^{1/2}\|A\|_{\Lambda^*_{m_1}}\Big(\sup_{\mathbf{g}\in\Lambda^*_{m_2}}\Big(\sum_{\mathbf{h}\in\Lambda^*_{m_1}}|\widetilde{B}_{\mathbf{gh}}|\Big)\Big)^{1/2}\|\mathbb{B}A\|_{\Lambda^*_{m_2}} \\ &= C_{\mathbb{B}}\|A\|_{\Lambda^*_{m_1}}\|\mathbb{B}A\|_{\Lambda^*_{m_2}}.\end{aligned}$$

Thus, Lemma 3.3.5 is established. □

The importance of Theorem 3.3.4 is that the growth rate $\kappa(\alpha)$ is completely independent of the domain Λ^*_m as long as Λ^*_m is contained in $\Lambda^{*\gamma}$. Thus, we will have the option to compare solutions obtained for different wave-vector sets Λ^*_m.

As a first consequence we obtain that for all $z \in [0, z_*]$ the solutions $\boldsymbol{\psi}(z) = (\psi_{\mathbf{g}}(z))_{\mathbf{g}\in\Lambda^*_m}$ decay with $|\mathbf{g}| \to \infty$. Indeed, recalling that the initial condition is given by the incoming wave encoded in the $\boldsymbol{\delta} = (\delta_{\mathbf{0},\mathbf{g}})_{\mathbf{g}\in\Lambda^*_m}$ (Kronecker symbol) we have:

$$\|\boldsymbol{\psi}(0)\|_\alpha = \|\boldsymbol{\psi}(0)\|_{\Lambda^*_m} = \|\boldsymbol{\delta}\|_{\Lambda^*_m} = \sqrt{\rho_{\mathbf{0}}} = \sqrt{\mathbf{k_0}\cdot\boldsymbol{\nu}} \approx \sqrt{|\mathbf{k_0}|}, \tag{3.15}$$

which is independent of the exponential weighting by α. With this and $\alpha \in \,]0, \alpha_{\mathbb{U}}[$ we obtain:

$$|\psi_{\mathbf{g}}(z)| \;\le\; \frac{\mathrm{e}^{-\alpha|\mathbf{g}|}}{\sqrt{\rho_{\mathbf{g}}}}\|\boldsymbol{\psi}(z)\|_\alpha \;\le\; \mathrm{e}^{\kappa(\alpha)|z|-\alpha|\mathbf{g}|}\sqrt{\frac{\rho_{\mathbf{0}}}{\rho_{\mathbf{g}}}}.$$

Thus, the exponential factor $\mathrm{e}^{\kappa(\alpha)|z|-\alpha|\mathbf{g}|}$ shows that the solution $\boldsymbol{\psi}(z)$ can only have a nontrivial effect at $\mathbf{g} \neq \mathbf{0}$ if $|z| > \alpha/\kappa(\alpha)\;|\mathbf{g}|$. We may consider the quotient $\alpha/\kappa(\alpha)$ as a collective scattering length that describes how fast a beam has to travel through the specimen to generate nontrivial amplitudes at neighboring wave vectors $\mathbf{g}$. In contrast, the extinction length $\xi_{\mathbf{g}}$ is defined for each individual $\mathbf{g} \in \Lambda^*$ (see [De 03, p.309]):

$$\frac{\alpha}{\kappa(\alpha)} = \frac{\gamma\,\mathbf{k_0}\cdot\boldsymbol{\nu}}{\pi C_{\mathbb{U}}\mathfrak{S}_1(\alpha_{\mathbb{U}}-\alpha)} \quad \text{versus the extinction length } \xi_g := \frac{|\rho_{\mathbf{g}}|}{|U_{\mathbf{g}}|}.$$

Hence, for doing a reasonable TEM experiment, one wants $\kappa(\alpha)z_*$ to be big enough to see some effect of scattering. However, it should not be too big such that the radius of possibly activated wave vectors with $|\psi_{\mathbf{g}}| \ge \varepsilon$ is not too small, namely those with $|\mathbf{g}| \le \frac{1}{\alpha}\big(\kappa(\alpha)z_* + \log(1/\varepsilon)\big)$. In addition we define the excitation length to be $\ell_{\text{excit}}(s_g) = 1/|s_{\mathbf{g}}|$, which describes the period of the phase oscillation of $\psi_{\mathbf{g}}(z)$.

3.3.3 Error estimates for finite-dimensional approximations

We now compare the DHW equations on different sets $\Lambda^*_{m_1}$ and $\Lambda^*_{m_2}$, both contained in $\Lambda^{*\gamma} \subset \Lambda^*$. We denote by $\boldsymbol{\psi}^{(j)}$ the solution of $\mathrm{DHW}_{\Lambda^*_{m_j}}$ with the initial condition $\boldsymbol{\psi}^{(j)}(0) = \boldsymbol{\delta}$. Assuming $\Lambda^*_{m_1} \subset \Lambda^*_{m_2}$, we can decompose $\boldsymbol{\psi}^{(2)}$ into two pieces, namely:

$$\boldsymbol{\psi}^{(2)} = (B, C) \quad \text{with } B = \boldsymbol{\psi}^{(2)}|_{\Lambda^*_{m_1}} := (\psi_{\mathbf{g}})_{\mathbf{g}\in\Lambda^*_{m_1}} \text{ and } C = \boldsymbol{\psi}^{(2)}|_{\Lambda^*_{m_2}\setminus\Lambda^*_{m_1}}.$$

We may rewrite the $\mathrm{DHW}_{\mathbf{G}^{(2)}}$ in block structure via:

$$R_{(1)}\dot{B} = \mathrm{i}\big(\;\Sigma_{(1)}B \;+ \mathbb{U}_{BB}B + \mathbb{U}_{BC}C\big), \qquad B(0) = (\delta_{\mathbf{0},\mathbf{g}})_{\mathbf{g}\in\Lambda^*_{m_1}}, \tag{3.16a}$$

$$R_{(2)\setminus(1)}\dot{C} = \mathrm{i}\big(\Sigma_{(2)\setminus(1)}B + \mathbb{U}_{CB}B + \mathbb{U}_{CC}C\big), \qquad C(0) = \mathbf{0}. \tag{3.16b}$$

Here, we used that the initial condition $\boldsymbol{\psi}(0)$ is localized in the incoming beam such that $\psi_{\mathbf{g}}(0) = 0$ for $\mathbf{g} \in \Lambda^*_{m_2} \setminus \Lambda^*_{m_1}$. Moreover, the $\mathrm{DHW}_{\Lambda^*_{m_1}}$ is given by (3.16a) if we omit the coupling term " $+\mathbb{U}_{BC}C$ ":

$$R_{(1)}\dot{\boldsymbol{\psi}}^{(1)} = \mathrm{i}\,\big(\Sigma_{(1)} + \mathbb{U}_{BB}\big)\boldsymbol{\psi}^{(1)}, \quad \boldsymbol{\psi}^{(1)}(0) = (\delta_{\mathbf{0},\mathbf{g}})_{\mathbf{g}\in\Lambda^*{}_{m_1}}. \tag{3.17}$$

The following result provides a first estimate between the solution $\boldsymbol{\psi}^{(2)} = (B, C)$ on the larger wave-vector set $\Lambda^*_{m_2}$ and $\boldsymbol{\psi}^{(1)}$ on the smaller set $\Lambda^*_{m_1}$ by exploiting the exponential decay estimates established in Theorem 3.3.4. In this first case, we consider only the model sets $\Lambda^*_{m_1} = \Lambda^{*M}$ and $\Lambda^*_{m_2} = \Lambda^{*\gamma}$ with $\Lambda^{*M} \subset \Lambda^{*\gamma}$, see (3.6).

Theorem 3.3.6 (Control of approximation errors)**.** *Assume that the assumptions* (3.2) *and* (3.9) *hold and that* $\mathbf{k_0}$, M *and* $\gamma \in \,]0,1[$ *are such that* $\Lambda^{*M} \subset \Lambda^{*\gamma}$. *Then, for* $\alpha \in \,]0, \alpha_{\mathbb{U}}[$ *the solutions* $\boldsymbol{\psi}^{\gamma}$ *and* $\boldsymbol{\psi}^{M}$ *of* $\mathrm{DHW}_{\Lambda^{*\gamma}}$ *and* $\mathrm{DHW}_{\Lambda^{*M}}$ *with initial condition* $\boldsymbol{\delta}$ *satisfy the estimates*

$$\left\|\boldsymbol{\psi}^M(z) - \boldsymbol{\psi}^{\gamma}(z)|_{\Lambda^{*M}}\right\|_{\Lambda^{*M}} \le \frac{\mathfrak{S}_0(\alpha_{\mathbb{U}}) - 1}{\alpha\, \mathfrak{S}_1(\alpha_{\mathbb{U}} - \alpha)}\, \mathrm{e}^{\kappa(\alpha)|z| - \alpha M}\, \|\boldsymbol{\delta}\| \quad \textit{and} \tag{3.18a}$$

$$\left\|\boldsymbol{\psi}^{\gamma}(z)|_{\Lambda^{*\gamma}\setminus\Lambda^{*M}}\right\|_{\Lambda^{*\gamma}\setminus\Lambda^{*M}} \le \mathrm{e}^{\kappa(\alpha)|z| - \alpha M}\|\boldsymbol{\delta}\| \quad \textit{for all } z \in \mathbb{R}, \tag{3.18b}$$

where as before $\mathfrak{S}_m(\beta) := \sum_{\varkappa \in \Lambda^*} |\varkappa|^m\, \mathrm{e}^{-\beta|\varkappa|}$.

Proof. We denote by $\Lambda^*_{\mathrm{O}} := \Lambda^{*\gamma} \setminus \Lambda^{*M}$ the set of outer wave vectors.

Step 1: Estimate of C. The solution $\boldsymbol{\psi}^{\gamma} = (B, C)$ satisfies all assumptions of Theorem 3.3.4. Hence, we can rely on the exponential estimate and obtain:

$$\begin{aligned} \|C(z)\|^2_{\Lambda^*_{\mathrm{O}}} &= \sum_{\mathbf{h} \in \Lambda^*_{\mathrm{O}}} \rho_{\mathbf{h}}\, |\psi_{\mathbf{h}}(z)|^2 \;\le\; \mathrm{e}^{-2\alpha M} \sum_{\mathbf{g} \in \Lambda^{*\gamma}} \rho_{\mathbf{g}}\, \mathrm{e}^{2\alpha|\mathbf{g}|}\, |\psi_{\mathbf{g}}(z)|^2 \\ &= \mathrm{e}^{-2\alpha M} \|\boldsymbol{\psi}^M(z)\|^2_{\alpha} \;\le\; \mathrm{e}^{2\kappa(\alpha)|z| - 2\alpha M} \|\boldsymbol{\psi}^M(0)\|^2_{\alpha} \;=\; \mathrm{e}^{2\kappa(\alpha)|z| - 2\alpha M}\|\boldsymbol{\delta}\|^2, \end{aligned}$$

which is the desired result (3.18b).

Step 2. Estimate between B *and* $\boldsymbol{\psi}^M$. For comparing B and $\boldsymbol{\psi}^M$, we define $A = B - \boldsymbol{\psi}^M$ and see that A satisfies:

$$R_M \dot{A}(z) = \mathrm{i}\big(\Sigma_M A(z) + \mathbb{U}_{BB} A(z) + \mathbb{U}_{BC} C(z)\big), \qquad A(0) = \mathbf{0}, \tag{3.19}$$

where now the initial condition is 0. Using the unitary group $\mathrm{e}^{\mathrm{i}zH_M}$ on $\mathfrak{H}(\Lambda^{*M})$ defined via $H_M = R_M^{-1}(\Sigma_M + \mathbb{U}_{BB})$, the solution is given in terms of Duhamel's principle via $A(z) = \int_0^z \mathrm{e}^{\mathrm{i}(z-\zeta)H_M} R_M^{-1} \mathbb{U}_{BC} C(\zeta)\,\mathrm{d}\zeta$. Taking the norm in $\mathfrak{H}(\Lambda^{*M})$, we arrive at:

$$\|A(z)\|_{\Lambda^{*M}} \le \int_0^z \|R_M^{-1}\mathbb{U}_{BC} C(\zeta)\|_{\Lambda^{*M}}\,\mathrm{d}\zeta \le \|R_M^{-1}\mathbb{U}_{BC}\|_{\mathfrak{H}(\Lambda^*_{\mathrm{O}}) \to \mathfrak{H}(\Lambda^{*M})} \int_0^z \|C(\zeta)\|_{\Lambda^*_{\mathrm{O}}}\,\mathrm{d}\zeta.$$

Using Lemma 3.3.5, the operator norm $N_{\mathrm{cpl}} = \|R_M^{-1}\mathbb{U}_{BC}\|$ can be estimated by:

$$N_{\mathrm{cpl}} \le \Big(\sup_{\mathbf{h} \in \Lambda^{*M}} \sum_{\mathbf{g} \in \Lambda^*_{\mathrm{O}}} \frac{\pi|U_{\mathbf{g}-\mathbf{h}}|}{\sqrt{\rho_{\mathbf{g}}\rho_{\mathbf{h}}}}\Big)^{1/2} \Big(\sup_{\mathbf{g} \in \Lambda^*_{\mathrm{O}}} \sum_{\mathbf{h} \in \Lambda^{*M}} \frac{\pi|U_{\mathbf{g}-\mathbf{h}}|}{\sqrt{\rho_{\mathbf{g}}\rho_{\mathbf{h}}}}\Big)^{1/2} \le \frac{\pi}{\gamma\rho_{\mathbf{0}}} \sup_{\mathbf{g} \in \Lambda^*} \sum_{\mathbf{h} \in \Lambda^* \setminus \{\mathbf{g}\}} C_{\mathbb{U}} \mathrm{e}^{-\alpha_{\mathbb{U}}|\mathbf{g}-\mathbf{h}|},$$

where we used $\mathbf{g} \in \Lambda^{*\gamma}$ and (3.9). We also increased the sets Λ^{*M} and Λ^*_{O} but kept the information that they are disjoint by summing only over $\mathbf{h}$ different from $\mathbf{g}$. Thus, we find $N_{\mathrm{cpl}} \le \pi C_{\mathbb{U}}\big(\mathfrak{S}_0(\alpha_{\mathbb{U}}) - 1\big)/(\gamma\rho_{\mathbf{0}})$.

Inserting this into the bound for $\|A(z)\|_{\Lambda^{*M}}$ and integrating the bound (3.18b) for $C(\zeta)$ we see cancellations in the factor $N_{\mathrm{cpl}}/\kappa(\alpha)$, and the result (3.18a) follows. □

The next result is dedicated to the case of two general sets $\Lambda^*_{m_1}$ and $\Lambda^*_{m_2}$ both of which satisfy $\Lambda^{*M} \subset \Lambda^*_{m_j} \subset \Lambda^{*\gamma}$ for $j = 1, 2$. Denoting by $\boldsymbol{\psi}^{(j)} : [0, z_*] \to \mathfrak{H}(\Lambda^*_{m_j})$ the solutions of $\mathrm{DHW}_{DLL_{m_j}}$, we will see that their restrictions to Λ^{*M} will be exponentially close with a factor $\mathrm{e}^{-\alpha M}$. This explains why the exact choice of the subset Λ^*_m of the wave vectors is not relevant as long as it contains a sufficiently large subset Λ^{*M}.

Corollary 3.3.7 (Arbitrary sets $\Lambda^*_{m_j}$ of wave vectors)**.** *Consider* $\mathbf{k_0}$*,* γ*, and* M *as in Theorem 3.3.6 and consider two subsets* $\Lambda^*_{m_j} \subset \Lambda^*$ *satisfying* $\Lambda^{*M} \subset \Lambda^*_{m_j} \subset \Lambda^{*\gamma}$ *for* $j = 1, 2$*. Then, the solutions* $\boldsymbol{\psi}^{(j)}$ *of* $\mathrm{DHW}_{\Lambda^*_{m_j}}$ *with initial condition* $\boldsymbol{\psi}^{(j)}(0) = \boldsymbol{\delta}$ *satisfy the estimate:*

$$\Big\|\boldsymbol{\psi}^{(1)}(z)|_{\Lambda^{*M}} - \boldsymbol{\psi}^{(2)}(z)|_{\Lambda^{*M}}\Big\|_{\Lambda^{*M}} \le \frac{2\,\big(\mathfrak{S}_0(\alpha_{\mathbb{U}})-1\big)}{\alpha\,\mathfrak{S}_1(\alpha_{\mathbb{U}}-\alpha)}\,\mathrm{e}^{\kappa(\alpha)|z|-\alpha M}\,\|\boldsymbol{\delta}\| \quad \textit{for all } z \in \mathbb{R}\,.$$

Proof. The proof follows simply by observing that Theorem 3.3.6 can easily be generalized by replacing the bigger set $\Lambda^{*\gamma}$ by any set Λ^*_m between Λ^{*M} and $\Lambda^{*\gamma}$. Hence, we can compare the two solutions $\boldsymbol{\psi}^{(j)}$ on Λ^{*M} with the solution $\boldsymbol{\psi}^M$ of $\mathrm{DHW}_{\Lambda^{*M}}$. Now the result follows by:

$$\|\boldsymbol{\psi}^{(1)}|_{\Lambda^{*M}} - \boldsymbol{\psi}^{(2)}|_{\Lambda^{*M}}\|_{\Lambda^{*M}} \le \|\boldsymbol{\psi}^{(1)}|_{\Lambda^{*M}} - \boldsymbol{\psi}^{M}\|_{\Lambda^{*M}} + \|\boldsymbol{\psi}^{M} - \boldsymbol{\psi}^{(2)}|_{\Lambda^{*M}}\|_{\Lambda^{*M}},$$

and applying (3.18a) with $\|\boldsymbol{\psi}(0)\|_\alpha = \|\boldsymbol{\delta}\| = \rho_{\mathbf{0}}^{1/2}$. □

From now on we will always choose $\alpha = \alpha_{\mathbb{U}}/2$, which is the intermediate value that makes all sums $\mathfrak{S}_m\big(\alpha_{\mathbb{U}}/2\big)$ finite. Thus, the critical exponential error term takes the form:

$$\mathrm{e}^{\kappa(\alpha_{\mathbb{U}}/2)z - M\alpha_{\mathbb{U}}/2} \quad \text{for } z \in [0, z_*].$$

From a practical perspective, there is no reason of doing a calculation in a set Λ^*_m bigger than Λ^{*M}, since increasing the number of ODEs without a gain in accuracy is useless. Moreover, it is desirable to reduce M as much as possible as the number of ODEs in $\mathrm{DHW}_{\Lambda^{*M}}$ with $M = \mu|\mathbf{k_0}|$ is proportional to M^d. However, in a true experiment we want to see the effect of scattering such that $\kappa(\alpha)z_*$ needs to be big enough. The way to make this work is to choose M proportional to a small power of $|\mathbf{k_0}|$:

$$M \sim |\mathbf{k_0}|^\eta \quad \text{with } \eta \in \,]0, 1[.$$

For instance, the first few Laue zones (see below) can be obtained by $\eta = 1/2$.

While in a ball Λ^{*M} of radius M the number of wave vectors scales with M^d, there are further physical reasons that many of these wave vectors are not relevant, as they cannot be activated because of energetic criteria as discussed next.

3.3.4 Averaging via conservation of the energy norm

The relevance of the Ewald sphere lies in the fact that on $\mathbb{S}_{\mathrm{Ew}}$ the excitation error $s_{\mathbf{g}} = \sigma_{\mathbf{g}}/(2\rho_{\mathbf{g}})$ equals 0. This means that beams propagating with wave vectors $\mathbf{g} \in \mathbb{S}_{\mathrm{Ew}}$ have much lower energy, because they have only little phase oscillations. Beams with wave vectors that are not close to the Ewald sphere will necessarily have much smaller amplitudes, because they have much larger phase oscillations than beams with wave vectors near the Ewald sphere. Mathematically, this can be manifested by conservation of suitable energies. Another way of obtaining this result would be by performing a temporal averaging for the functions $\psi_{\mathbf{g}}$ with large $|s_{\mathbf{g}}|$.

We return to the DHW equation on $\Lambda^*_m = \Lambda^{*M} \subset \Lambda^{*\gamma}$. The linear finite-dimensional Hamiltonian system:

$$R\dot{\boldsymbol{\psi}} = \mathrm{i}\big(\Sigma{+}\mathbb{U}\big)\boldsymbol{\psi}, \quad \boldsymbol{\psi}(0) = \boldsymbol{\delta} \in \mathfrak{H}(\Lambda^{*M}), \tag{3.20}$$

can be rewritten via the transformation $\widetilde{R} = R^{1/2} = \mathrm{diag}\,\big((\rho_{\mathbf{g}}/\pi)^{1/2}\big)_{\mathbf{g}\in\Lambda^*_m}$. Setting $A = \widetilde{R}\boldsymbol{\psi}$, system (3.20) takes the standard Hamiltonian form:

$$\dot{A} = \mathrm{i}\,\mathbb{H}A \quad \text{with } \mathbb{H} = \widetilde{R}^{-1}\,\big(\Sigma{+}\mathbb{U}\big)\,\widetilde{R}^{-1}, \tag{3.21}$$

where $\mathbb{H}$ is now a Hermitian operator on $\ell^2(\Lambda^{*M})$, now using the standard scalar product. This provides the explicit solution $A(z) = \mathrm{e}^{\mathrm{i}z\mathbb{H}}A(0)$ via the unitary group $z \mapsto \mathrm{e}^{\mathrm{i}z\mathbb{H}}$. An easy consequence is the invariance of the hierarchy of norms:

$$\forall\, k \in \mathbb{N}_0\; \forall\, z \in \mathbb{R}: \quad \big\langle \mathbb{H}^k A(z), A(z)\big\rangle = \big\langle \mathbb{H}^k A(0), A(0)\big\rangle\,.$$

For $k = 0$ this is the simple wave-flux conservation established in Proposition 3.3.1. The result for $k = 1$ is not useful, because the operator $\mathbb{H}$ is indefinite, since $\mathbb{U}$ is bounded and Σ has many positive (associated with $\mathbf{g}$ inside the Ewald sphere) and many negative eigenvalues (associated with $\mathbf{g}$ outside the Ewald sphere).

Hence, we concentrate on the case $k = 2$, where:

$$0 \le \mathbb{H}^2 = \widetilde{\Sigma}^2 + \widetilde{\mathbb{U}}\widetilde{\Sigma} + \widetilde{\Sigma}\widetilde{\mathbb{U}} + \widetilde{\mathbb{U}}^2, \quad \text{with } \widetilde{\Sigma} := \widetilde{R}^{-1}\Sigma\widetilde{R}^{-1} = R^{-1}\Sigma \text{ and } \widetilde{\mathbb{U}} := \widetilde{R}^{-1}\mathbb{U}\widetilde{R}^{-1}.$$

The following, rather trivial result highlights that $\mathbb{H}^2$ has suitable definiteness properties that will then be useful for estimating the solutions of the DHW equation.

Lemma 3.3.8 (Energy estimate). *Let* $\mathbb{H} = \widetilde{\Sigma} + \widetilde{\mathbb{U}}$ *where* $\widetilde{\Sigma}$ *and* $\mathbb{H}$ *are Hermitian, then we have the estimate:*

$$\|\mathbb{H}A\|^2 = \big\langle \mathbb{H}^2 A, A\big\rangle \ge \frac{1}{2}\|\widetilde{\Sigma}A\|^2 - \|\widetilde{\mathbb{U}}A\|^2 \quad \textit{for all } A \in \ell^2(\Lambda^{*M}). \tag{3.22}$$

Proof. We expand $\mathbb{H}^2$ in a suitable way:

$$\begin{aligned}\mathbb{H}^2 = (\widetilde{\Sigma} + \widetilde{\mathbb{U}})^2 &= \frac{1}{2}\widetilde{\Sigma}^2 + \big(\frac{1}{2}\widetilde{\Sigma}^2 + \widetilde{\Sigma}\widetilde{\mathbb{U}} + \widetilde{\mathbb{U}}\widetilde{\Sigma} + 2\widetilde{\mathbb{U}}^2\big) - \widetilde{\mathbb{U}}^2 \\ &= \frac{1}{2}\widetilde{\Sigma}^2 + \Big(\frac{1}{\sqrt{2}}\widetilde{\Sigma} + \sqrt{2}\widetilde{\mathbb{U}}\Big)^2 - \widetilde{\mathbb{U}}^2 \;\geq\; \frac{1}{2}\widetilde{\Sigma}^2 - \widetilde{\mathbb{U}}^2.\end{aligned}$$

This is the desired result. □

It is instructive to transform estimate (3.22) back to the original variable $\boldsymbol{\psi}$ and the operator $H = R^{-1}(\Sigma{+}\mathbb{U})$, which yields:

$$\|R^{-1}\Sigma\boldsymbol{\psi}\|^2_{\Lambda^{*M}} \;\leq\; 2\,\|H\boldsymbol{\psi}\|^2_{\Lambda^{*M}} + 2\,\|R^{-1}\mathbb{U}\boldsymbol{\psi}\|^2_{\Lambda^{*M}}. \tag{3.23}$$

Since along solutions $z \mapsto \boldsymbol{\psi}(z) \in \mathfrak{H}(\Lambda^{*M})$ of $\mathrm{DHW}_{\Lambda^{*M}}$ the energy $\|H\boldsymbol{\psi}(z)\|^2_{\Lambda^{*M}}$ is constant, see (3.8), we can use this for bounding $\|R^{-1}\Sigma\boldsymbol{\psi}(z)\|^2_{\Lambda^{*M}}$.

Proposition 3.3.9 (Energy bound for solutions)**.** *Consider* $\mathbf{k_0}$, γ, *and* M *such that* $\Lambda^{*M} \subset \Lambda^{*\gamma}$. *Let* $\boldsymbol{\psi}$ *be the solution of* $\mathrm{DHW}_{\Lambda^{*M}}$ *with initial condition* $\boldsymbol{\psi}(0) = \boldsymbol{\delta}$. *Then,* $\boldsymbol{\psi}$ *satisfies the estimate:*

$$\|R^{-1}\Sigma\boldsymbol{\psi}(z)\|_{\Lambda^{*M}} \leq \frac{2\pi\, C_{\mathbb{U}}\mathfrak{S}_0(\alpha_{\mathbb{U}})}{\gamma\rho_{\mathbf{0}}}\|\boldsymbol{\delta}\|_{\Lambda^{*M}} \quad \textit{for all } z \in \mathbb{R}.$$

Proof. Lemma 3.3.5 yields $\|R^{-1}\mathbb{U}\boldsymbol{\psi}\|_{\Lambda^{*M}} \leq N_1\|\boldsymbol{\psi}\|_{\Lambda^{*M}}$ with $N_1 = \pi\, C_{\mathbb{U}}\mathfrak{S}_0(\alpha_{\mathbb{U}})/(\gamma\rho_{\mathbf{0}})$. Exploiting (3.23) and the conservation of $\|H\boldsymbol{\psi}(z)\|^2_{\Lambda^{*M}}$ and $\|\boldsymbol{\psi}(z)\|^2_{\Lambda^{*M}}$ we find

$$\begin{aligned}\|R^{-1}\Sigma\boldsymbol{\psi}(z)\|^2_{\Lambda^{*M}} &\leq 2\|H\boldsymbol{\psi}(z)\|^2_{\Lambda^{*M}} + 2N_1^2\|\boldsymbol{\psi}(z)\|^2_{\Lambda^{*M}} \\ &= 2\|H\boldsymbol{\psi}(0)\|^2_{\Lambda^{*M}} + 2N_1^2\|\boldsymbol{\psi}(0)\|^2_{\Lambda^{*M}} = 2\|R^{-1}\mathbb{U}\boldsymbol{\delta}\|^2_{\Lambda^{*M}} + 2N_1^2\rho_{\mathbf{0}} \leq 4N_1^2\rho_{\mathbf{0}},\end{aligned}$$

where we used $\boldsymbol{\psi}(0) = \boldsymbol{\delta}$ and $\sigma_{\mathbf{0}} = 0$. This shows the desired assertion. □

Using the energy bound, we can split the set Λ^{*M} according to the size of the excitation errors $s_{\mathbf{g}} = \sigma_{\mathbf{g}}/(2\rho_{\mathbf{g}})$ using a cut-off value $\widetilde{s}_*$ to be chosen later:

$$\begin{aligned}\Lambda^{*M} = \Lambda^{*M}_{\mathrm{Ew}} \,\dot{\cup}\, \Lambda^{*M}_{\mathrm{far}} \quad \text{with } \Lambda^{*M}_{\mathrm{Ew}} &:= \big\{\mathbf{g} \in \Lambda^{*M} \,\big|\, |\sigma_{\mathbf{g}}|/(2\rho_{\mathbf{g}}) < \widetilde{s}_*\big\} \\ \text{and } \Lambda^{*M}_{\mathrm{far}} &:= \big\{\mathbf{g} \in \Lambda^{*M} \,\big|\, |\sigma_{\mathbf{g}}|/(2\rho_{\mathbf{g}}) \geq \widetilde{s}_*\big\}.\end{aligned}$$

Of course, we always have $\mathbf{g} = \mathbf{0} \in \Lambda^{*M}_{\mathrm{Ew}}$, as $\sigma_{\mathbf{0}} = 0$ and $\widetilde{s}_* > 0$.

Using the energy bound from Proposition 3.3.9 and $R^{-1}\Sigma = \mathrm{diag}(\pi\sigma_{\mathbf{g}}/\rho_{\mathbf{g}})$, we immediately see that solutions $\boldsymbol{\psi}$ of $\mathrm{DHW}_{\Lambda^{*M}}$ satisfy:

$$\|\boldsymbol{\psi}^M(z)|_{\Lambda^{*M}_{\mathrm{far}}}\|_{\Lambda^{*M}_{\mathrm{far}}} \leq \frac{1}{\widetilde{s}_*}\,\frac{C_{\mathbb{U}}\,\mathfrak{S}_0(\alpha_{\mathbb{U}})}{\gamma\rho_{\mathbf{0}}}\|\boldsymbol{\delta}\|_{\Lambda^{*M}} \quad \text{for all } z \in \mathbb{R}. \tag{3.24}$$

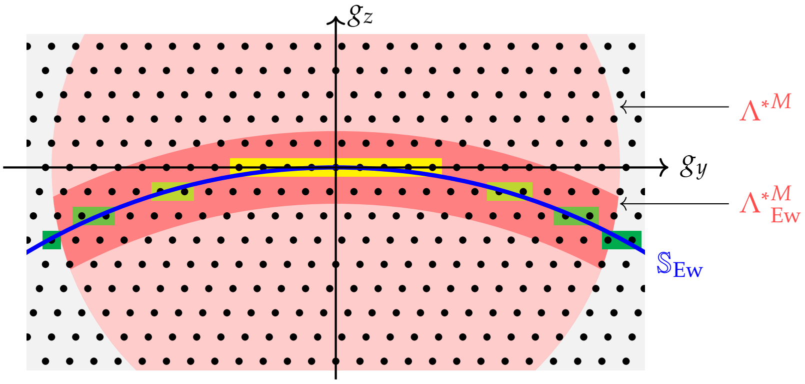

Figure 3.4: Ewald sphere $\mathbb{S}_{\mathrm{Ew}}$ (blue), dual lattice Λ^* (black dots), and the decomposition of Λ^{*M} (light red ball) into $\Lambda^{*M}_{\mathrm{Ew}}$ (red annular arc, for $\widetilde{s}_* = 3\pi$) and $\Lambda^{*M}_{\mathrm{far}}$. The boxes indicate the Laue zones: lowest order (yellow) to third order (green). Reprinted with permission from [KMM21, Fig. 4.1], published by the Society for Industrial and Applied Mathematics (SIAM). Copyright © by SIAM.

The factor in front of $\|\boldsymbol{\delta}\|_{\Lambda^{*M}} = \rho_{\mathbf{0}}$ is small if the "cut-off" excitation length $\ell_{\mathrm{excit}}(s_*) = 1/\widetilde{s}_*$ is small with respect to the global scattering length $\ell_{\mathrm{scatt}} = \rho_{\mathbf{0}}/C_{\mathbb{U}}$. In such a case, it may be reasonable to neglect these wave vectors and solve DHW on the much smaller set $\Lambda^{*M}_{\mathrm{Ew}}$ instead in all of Λ^{*M}. The error is controlled in the following result.

Theorem 3.3.10 (Reduction to Ewald sphere)**.** *Under the above assumptions consider the solutions $\boldsymbol{\psi}^M$ and $\boldsymbol{\psi}^M_{\mathrm{Ew}}$ of* $\mathrm{DHW}_{\Lambda^{*M}}$ *and* $\mathrm{DHW}_{\Lambda^{*M}_{\mathrm{Ew}}}$ *with initial condition $\boldsymbol{\delta}$, respectively. If $\Lambda^{*M}_{\mathrm{Ew}}$ is given by $\widetilde{s}_*$, then for all $z \in \mathbb{R}$ we have the error estimate:*

$$\|\boldsymbol{\psi}^M_{\mathrm{Ew}}(z) - \boldsymbol{\psi}^M(z)|_{\Lambda^{*M}_{\mathrm{Ew}}}\|_{\Lambda^{*M}_{\mathrm{Ew}}} \le |z|\, \frac{\pi}{\widetilde{s}_*}\, \frac{C_{\mathbb{U}}^2\,(\mathfrak{S}_0(\alpha_{\mathbb{U}})-1)\,\mathfrak{S}_0(\alpha_{\mathbb{U}})}{\gamma^2\,\rho_{\mathbf{0}}^2}\, \|\boldsymbol{\delta}\|_{\Lambda^{*M}}\,. \tag{3.25}$$

Proof. We proceed exactly as in the proof of Theorem 3.3.6, but the nested couple $(\Lambda^{*M}, \Lambda^{*\gamma})$ is replaced here by the nested couple $(\Lambda^{*M}_{\mathrm{Ew}}, \Lambda^{*M})$. The bound in Step 1 is replaced by the bound for $\boldsymbol{\psi}^M(z)|_{\Lambda^{*M}_{\mathrm{far}}}$ in (3.24). In Step 2 the norm of the coupling operator can be estimated by the same constant N_{cpl}. Now:

$$\|\boldsymbol{\psi}^M_{\mathrm{Ew}}(z) - \boldsymbol{\psi}^M(z)|_{\Lambda^{*M}_{\mathrm{Ew}}}\|_{\Lambda^{*M}_{\mathrm{Ew}}} \le \int_0^z N_{\mathrm{cpl}} \|\boldsymbol{\psi}^M(\zeta)|_{\Lambda^{*M}_{\mathrm{far}}}\|_{\Lambda^{*M}_{\mathrm{far}}}\, \mathrm{d}\zeta$$

gives the desired result. □

Estimate (3.25) for $z \in [0, z_*]$ contains the main error term $\frac{z_*}{\ell_{\mathrm{scatt}}} \frac{\ell_{\mathrm{excit}}(\widetilde{s}_*)}{\ell_{\mathrm{scatt}}}$. Because of $z_* \approx \ell_{\mathrm{scatt}}$, it is important to have $\widetilde{s}_*$ big enough to obtain $\ell_{\mathrm{excit}}(\widetilde{s}_*) = 1/\widetilde{s}_* \ll \ell_{\mathrm{scatt}}$.

However, using the fact that $|\sigma_{\mathbf{g}}| \approx 2|\mathbf{k}_0|\,\mathrm{dist}(\mathbf{g}, \mathbb{S}_{\mathrm{Ew}})$ and $|\rho_{\mathbf{g}}| \approx |\mathbf{k}_0|$, we see that the number of wave vectors in $\Lambda^{*M}_{\mathrm{Ew}}$ is proportional to $O(\widetilde{s}_* M^{d-1})$, while the number of wave vectors in Λ^{*M} scales like $O(M^d)$. Thus, it is desirable to make $\widetilde{s}_*$ even less than 1, which means one spacing in Λ^* perpendicular to $\mathbb{S}_{\mathrm{Ew}}$ (recall that $\widetilde{s}_*$ has the physical dimension of $|\mathbf{k_0}|$ which is an inverse length).

3.4 Special approximations

Here, we discuss approximations that are commonly used in the physical literature to interpret TEM measurements, see [Jam90; De 03; Kir20]. We start with an easy case where only the incoming beam is considered, see 3.4.1. Then we consider the cases of the lowest-order Laue zone 3.4.2, the two-beam approximation 3.4.3 and the systematic-row approximation 3.4.4.

3.4.1 Free-beam approximation

For a mathematical comparison, it is instructive to consider the trivial approximation, where only the incoming beam is considered, i.e. we use $\Lambda^*_1 = \{\mathbf{0}\}$, i.e. the equation $\mathrm{DHW}_{\{\mathbf{0}\}}$ consists of the single ODE:

$$\frac{\rho_\mathbf{0}}{\pi}\,\dot{\psi}_\mathbf{0} = \mathrm{i}(\sigma_\mathbf{0}+U_\mathbf{0})\psi_\mathbf{0}, \quad \psi_\mathbf{0}(0) = 1. \tag{3.26}$$

Using $\sigma_\mathbf{0} = 0$, we obtain the trivial solution $\psi_\mathbf{0}(z) = \mathrm{e}^{\mathrm{i}z\pi U_\mathbf{0}/\rho_\mathbf{0}}$ and obtain that the intensity $I_\mathbf{0}$ remains constant: $I_\mathbf{0}(z) = |\psi_\mathbf{0}(z)|^2 = 1$. We will see that this is a reasonable approximation for $z \in [0, z_*]$, if $z_* C_\mathbb{U}/|\mathbf{k_0}| = z_*/\ell_{\mathrm{scatt}} \ll 1$, which means that the scattering length is small compared to the thickness z_* of the specimen.

Lemma 3.4.1 (Free beam)**.** *Choose* $\gamma \in\,]0,1[$ *and consider* $\Lambda^*_m \subset \Lambda^{*\gamma}$ *with* $\mathbf{0} \in \Lambda^*_m$*. Let the solution* $\boldsymbol{\psi} = (\psi_\mathbf{g})_{\mathbf{g}\in\Lambda^*_m}$ *of* $\mathrm{DHW}_{\Lambda^*_m}$ *with initial condition* $\boldsymbol{\psi}(0) = \boldsymbol{\delta}$ *and let* $\widehat{\psi}_\mathbf{0}$ *be the solution of* (3.26)*. Then we have the approximation errors:*

$$|\widehat{\psi}_\mathbf{0}(z) - \psi_\mathbf{0}(z)| \le \min\{N_{\mathrm{cpl}}|z|,\, 2\} \quad \textit{with } N_{\mathrm{cpl}} = \frac{\pi C_\mathbb{U}(\mathfrak{S}_0(\alpha_\mathbb{U}) - 1)}{\gamma\rho_\mathbf{0}}, \tag{3.27a}$$

$$\|\boldsymbol{\psi}(z)|_{\Lambda^*_m\backslash\{\mathbf{0}\}}\|_{\Lambda^*_m\backslash\{\mathbf{0}\}} \le \min\{N_{\mathrm{cpl}}|z|,\, 1\}\|\boldsymbol{\delta}\|_{\Lambda^*_m} \quad \textit{for all } z \in \mathbb{R}\,. \tag{3.27b}$$

Proof. This result follows exactly as in Theorem 3.3.10, where we now use the a priori estimate $\|\boldsymbol{\psi}(z)|_{\Lambda^*_m\backslash\{\mathbf{0}\}}\|_{\Lambda^*_m\backslash\{\mathbf{0}\}} \le \|\boldsymbol{\psi}(z)\|_{\Lambda^*_m} = \|\boldsymbol{\delta}\|_{\Lambda^*_m} = |\rho_\mathbf{0}|^{1/2}$. Then, the analog to (3.25) gives $|\rho_\mathbf{0}|^{1/2}|\widehat{\psi}_\mathbf{0}(z) - \psi_\mathbf{0}(z)| \le N_{\mathrm{cpl}}|\rho_\mathbf{0}|^{1/2}|z|$. Together with the trivial bounds $|\rho_\mathbf{0}|^{1/2}|\psi_\mathbf{0}(z)| \le \|\boldsymbol{\psi}(z)\|_{\Lambda^*_m} = |\rho_\mathbf{0}|^{1/2}$ we arrive at (3.27a).

To obtain the second equation we set $B(z) = \boldsymbol{\psi}(z)|_{\Lambda^*_m\backslash\{\mathbf{0}\}} \in \mathfrak{H}(\Lambda^*_m\backslash\{\mathbf{0}\})$ and apply Duhamel's principle to $\mathrm{i}R\dot{B} + \Sigma B - \mathbb{U}_{BB}B = \mathbb{U}_{B,\{\mathbf{0}\}}\psi_{\mathbf{0}}(z)$ and obtain:

$$\|\boldsymbol{\psi}(z)|_{\Lambda^*_m\setminus\{\mathbf{0}\}}\|_{\Lambda^*_m\setminus\{\mathbf{0}\}} \le \int_0^z \|\mathbb{U}_{B,\{\mathbf{0}\}}\|\,\|\psi_{\mathbf{0}}(\zeta)\|_{\{\mathbf{0}\}}\,\mathrm{d}\zeta \le \int_0^z N_{\mathrm{cpl}}|\rho_{\mathbf{0}}|^{1/2}\,\mathrm{d}\zeta = N_{\mathrm{cpl}}|\rho_{\mathbf{0}}|^{1/2}|z|.$$

Together with the trivial bound $\|\boldsymbol{\psi}(z)|_{\Lambda^*_m\setminus\{\mathbf{0}\}}\|_{\Lambda^*_m\setminus\{\mathbf{0}\}} \le \|\boldsymbol{\psi}(z)\|_{\Lambda^*_m} = |\rho_{\mathbf{0}}|^{1/2}$ we find (3.27b). □

Thus, this trivial result provides a rigorous quantitative estimate for the obvious fact that the incoming beam stays undisturbed only if the thickness z_* of the specimen is significantly shorter than the scattering length $|\mathbf{k}_0|/C_{\mathbb{U}}$, i.e. $N_{\mathrm{cpl}}z_* \ll 1$.

3.4.2 Approximation via the lowest-order Laue zone

The lowest-order Laue zone (LOLZ) is defined if the wave vectors in the tangent plane $\mathbf{T}_{\mathbf{k}_0} := \big\{\, \eta \in \mathbb{R}^d \,\big|\, \eta \cdot \mathbf{k}_0 = 0 \,\big\}$ to the Ewald sphere $\mathbb{S}_{\mathrm{Ew}}$ at $\mathbf{g} = \mathbf{0}$ form a lattice of dimension $d-1$. Denoting by κ_* the minimal distance between different points in Λ^* we define:

$$\Lambda^*_{\mathrm{LOLZ}} := \big\{\, \mathbf{g} \in \Lambda^* \cap \mathbf{T}_{\mathbf{k}_0} \,\big|\, \mathrm{dist}(\mathbf{g}, \mathbb{S}_{\mathrm{Ew}}) \le \kappa_*/2 \,\big\},$$

see Figure 3.4 for an illustration. Because the Ewald sphere can be approximated by the parabola $g_z = -|g_x|^2/(2|\mathbf{k}_0|)$, the set $\Lambda^*_{\mathrm{LOLZ}}$ is contained in a circle of radius $M := m_*|\mathbf{k}_0|^{1/2}$ inside $\mathbf{T}_{\mathbf{k}_0}$, where $m_* = \kappa_*^{1/2}$. (To include higher-order Laue zones up to order n one chooses $m_* = \big((2n+1)\kappa_*\big)^{1/2}$.)

This observation allows us to assess the approximation error for the solution $\boldsymbol{\psi}^{\mathrm{LOLZ}}$ that is obtained by solving the DHW equation on $\mathfrak{H}(\Lambda^*_{\mathrm{LOLZ}})$. For this, we first use Theorem 3.3.6 to reduce to the set Λ^{*M} with $M = m_*|\mathbf{k}_0|^{1/2}$, and then we reduce to the set $\Lambda^*_{\mathrm{LOLZ}} = \Lambda^{*M}_{\mathrm{Ew}}$ using Theorem 3.3.10 with a suitable $\widetilde{s}_* \sim \kappa_*$. In the following result, we give the exact formulas for the constants in the error estimate. In particular, we will drop the dependence on $\alpha_{\mathbb{U}}$, which we consider to be fixed. However, we keep the dependence on $|\mathbf{k}_0|$ and $C_{\mathbb{U}}$ to the influence of the energy and the scattering. To achieve formulas with correct physical dimensions, we sometimes use the length scale α_*, which could be chosen as the lattice constant of Λ, as $1/\kappa_*$, or simply $\alpha_{\mathbb{U}}$. We will use generic, dimensionless constants N and N_j that may change from line to line and will depend on α_* and $\alpha_{\mathbb{U}}$, but do not depend on $|\mathbf{k}_0|$ and $C_{\mathbb{U}}$.

Theorem 3.4.2 (LOLZ approximation). *Consider the solution* $\boldsymbol{\psi}^{\gamma}$ *of* $\mathrm{DHW}_{\Lambda^{*\gamma}}$ *with* $\gamma = 1/2$ *and the solution* $\boldsymbol{\psi}^{\mathrm{LOLZ}}$ *of* $\mathrm{DHW}_{\Lambda^*_{\mathrm{LOLZ}}}$ *for the initial condition* $\boldsymbol{\delta}$. *Given a constant* $N_0 > 0$, *there exists constants* k_* *and* N_1 *such that the following holds:*

$$\text{If } |\mathbf{k}_0| \ge k_* \text{ and } z_* \le N_0|\alpha_*\mathbf{k}_0|^{1/3}\frac{|\mathbf{k}_0|}{C_{\mathbb{U}}}, \text{ then for all } z \in [0, z_*] \text{ we have} \tag{3.28a}$$

$$\|\boldsymbol{\psi}^{\mathrm{LOLZ}}(z) - \boldsymbol{\psi}^{\gamma}(z)|_{\Lambda^*_{\mathrm{LOLZ}}}\|_{\Lambda^*_{\mathrm{LOLZ}}} \le N_1\Big(\frac{1}{|\alpha_*\mathbf{k}_0|^2} + \frac{\alpha_* C_{\mathbb{U}}^2}{|\mathbf{k}_0|^2}\,z_*\Big)\|\boldsymbol{\delta}\|\,. \tag{3.28b}$$

Proof. Step 1. Reduction to Λ^{*M}. Using $M = m_*|\mathbf{k_0}|^{1/2}$ and $|\mathbf{k_0}| \geq k_*$ we have $\Lambda^{*M} \subset \Lambda^{*\gamma}$, and Theorem 3.3.6 with $\alpha = \alpha_{\mathbb{U}}/2$ provides the error estimate:

$$\|\boldsymbol{\psi}^M(z) - \boldsymbol{\psi}^\gamma(z)|_{\Lambda^{*M}}\|_{\Lambda^{*M}} \leq N_2\, \mathrm{e}^{N_3 C_{\mathbb{U}} z/|\mathbf{k_0}| - N_4|\alpha_*\mathbf{k_0}|^{1/2}} \|\boldsymbol{\delta}\|\,.$$

Step 2. Reduction to Λ^*_{LOLZ}. The theory in Section 3.3.4 reduces to the Ewald sphere. In particular, because of our given radius $M = m_*|\mathbf{k_0}|^{1/2}$ the set Λ^{*M}_{Ew} exactly equals Λ^*_{LOLZ} if we choose the cut-off value $\widetilde{s}_*$ suitably.

For this, we have to identify the smallest value of $|\sigma_\mathbf{g}/\rho_\mathbf{g}|$ in $\Lambda^{*M}\backslash\Lambda^*_{\text{LOLZ}}$. Because $\rho_\mathbf{g} = \mathbf{k_0}\cdot\boldsymbol{\nu} + O(|\mathbf{k_0}|^{1/2})$ in Λ^{*M}, it suffices to minimize $|\sigma_\mathbf{g}|$ in $\Lambda^{*M}_{\text{far}} = \Lambda^{*M}\backslash\Lambda^*_{\text{LOLZ}}$, or simply minimize the distance to $\mathbb{S}_{\text{Ew}}$. Hence, the points in the interior of the Ewald balls in the lattice layer right below $\Lambda^*_{\text{LOLZ}} \subset \mathbf{T}$ are most critical. All of them have distance κ_* to $\mathbf{T}$ and thus their distance to the Ewald sphere is bigger or equal $\kappa_* - M^2/(2|\mathbf{k_0}|) = \kappa_*/2 > 0$.

From this, for $\mathbf{g} \in \Lambda^{*M}_{\text{far}}$ one has $|s_\mathbf{g}| \geq \frac{\kappa_*}{2}\,|\mathbf{k_0}|$, and with $\rho_\mathbf{0} \approx |\mathbf{k_0}|$ we are able to apply Theorem 3.3.10 with $\widetilde{\sigma}_* = \kappa_*/3$, which is independent of $|\mathbf{k_0}|$ and $\mathbb{C}_{\mathbb{U}}$. With this we conclude $\|\boldsymbol{\psi}^{\text{LOLZ}}(z) - \boldsymbol{\psi}^M(z)|_{\Lambda^*_{\text{LOLZ}}}\|_{\Lambda^*_{\text{LOLZ}}} \leq |z|N_4 C_{\mathbb{U}}^2\|\boldsymbol{\delta}\|/|\mathbf{k_0}|^2$ for all $z \in \mathbb{R}$.

Step 3. Combined estimate. We observe that the second relation in (3.28a) allows us to simplify the estimate in Step 1. For $z \in [0, z_*]$ the exponent can be estimated via:

$$N_3 C_{\mathbb{U}} z/|\mathbf{k_0}| - N_4|\alpha_*\mathbf{k_0}|^{1/2} \leq N_3 N_0|\alpha_*\mathbf{k_0}|^{1/3} - N_4|\alpha_*\mathbf{k_0}|^{1/2} \leq N_5 - \tfrac{N_4}{2}|\alpha_*\mathbf{k_0}|^{1/2}.$$

Now, the final result follows $\mathrm{e}^{-N_6|\mathbf{k_0}|^{1/2}} \leq N_7/|\mathbf{k_0}|^2$ and the previous two steps. □

3.4.3 Two-beam approximation and beating

The most simple nontrivial approximation is obtained by assuming that the incoming beam at $\mathbf{g} = \mathbf{0}$ interacts mainly with one other wave vector $\mathbf{g}'$. The energy exchange between $\psi_\mathbf{0}$ and $\psi_{\mathbf{g}'}$ is called beating and occurs on a well controllable length scale. Thus, it can be used effectively for generating contrast in microscopy, see [Dar14] or [MNS+20, Sec. 4].

The theory is often explained by the following two-equation approximation of DHW with $\Lambda_2^* = \{\mathbf{0}, \mathbf{g}'\}$, but even though it turns out that this model nicely predicts certain qualitative features it is not accurate enough for quantitative predictions. For a typical microscopical experiment, one chooses $\mathbf{k_0}$ such that $\mathbf{g} = \mathbf{0}$ and $\mathbf{g} = \mathbf{g}'$ are the only two wave vectors on the Ewald sphere:

$$\sigma_\mathbf{0} = \sigma_{\mathbf{g}'} = 0 \quad \text{and} \quad \rho_\mathbf{0} = \boldsymbol{\nu}\cdot\mathbf{k_0} = \rho_{\mathbf{g}'}. \tag{3.29}$$

Assuming $\mathbf{g}' = (0, n, 0) \in \Lambda_2^*$ with a small integer n, this can be achieved by setting $\mathbf{k_0} = (\theta, -n/2, k)$ with $k \approx |\mathbf{k_0}| \gg 1$ and $|\theta| < 1$, see Figure 3.5. Then, the two-equation

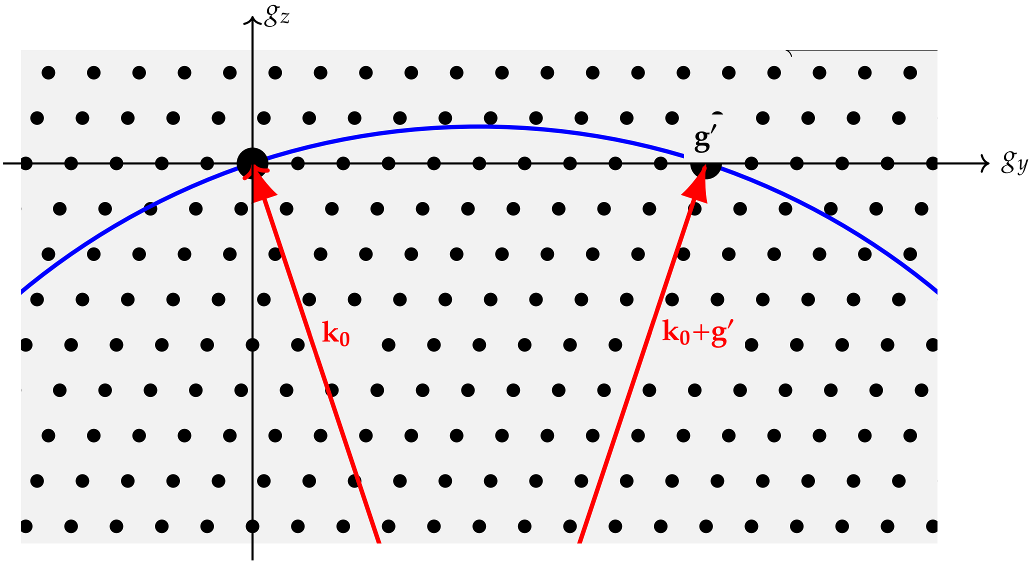

Figure 3.5: A typical setup for the two-beam conditions: $\mathbf{g} = \mathbf{0}$ and $\mathbf{g} = \mathbf{g}'$ are the only two points in $\mathbb{S}_{\mathrm{Ew}} \cap \Lambda^*$. Reprinted with permission from [KMM21, Fig. 4.2], published by the Society for Industrial and Applied Mathematics (SIAM). Copyright © by SIAM.

model for $\mathbf{g} = \mathbf{0}$ and $\mathbf{g} = \mathbf{g}'$ reads:

$$\frac{\rho_0}{\pi}\,\dot{\psi}_{\mathbf{0}} = \mathrm{i}\big(\sigma_0\psi_0 + U_0\psi_0 + \overline{U}_{\mathbf{g}'}\psi_{\mathbf{g}'}\big), \quad \frac{\rho_{\mathbf{g}'}}{\pi}\,\dot{\psi}_{\mathbf{g}'} = \mathrm{i}\big(\sigma_{\mathbf{g}'}\psi_{\mathbf{g}'} + U_{\mathbf{g}'}\psi_{\mathbf{0}} + U_{\mathbf{0}}\psi_{\mathbf{g}'}\big)\,. \tag{3.30}$$

This complex two-dimensional and real four-dimensional system can be solved explicitly leading to quasi-periodic motions with the frequencies $\omega_{1,2} = \pi(U_{\mathbf{0}} \pm |U_{\mathbf{g}'}|)/\rho_{\mathbf{0}}$, where we used (3.29) to simplify the general expression.

Recalling the wave-flux conservation from Proposition 3.3.1, we obtain the relation

$$\rho_{\mathbf{0}}|\psi_{\mathbf{0}}(z)|^2 + \rho_{\mathbf{g}'}|\psi_{\mathbf{g}'}(z)|^2 = \rho_{\mathbf{0}} \tag{3.31}$$

by using the initial condition $\boldsymbol{\psi}(0) = \boldsymbol{\delta}$. A direct, but lengthy, calculation gives:

$$I_{\mathbf{0}}(z) := |\psi_{\mathbf{0}}(z)|^2 = \big(\cos(\frac{\pi|U_{\mathbf{g}'}|}{\rho_{\mathbf{0}}}z)\big)^2 \text{ and } I_{\mathbf{g}'}(z) := |\psi_{\mathbf{g}'}(z)|^2 = \big(\sin(\frac{\pi|U_{\mathbf{g}'}|}{\rho_{\mathbf{0}}}z)\big)^2, \tag{3.32}$$

which clearly displays the energy exchange, also called beating.

We do not give a proof for the validity of the two-beam approximation, but rather address its limitations. However, we refer to the systematic-row approximation in the next section, which includes the two-beam approximation as a special case. To see the limitation, we simply argue that having the beams in $\mathbf{g} = \mathbf{0}$ and $\mathbf{g} = \mathbf{g}' = (0, n, 0)$, we also have scattering from $\mathbf{g} = \mathbf{0}$ to the neighbors $(0, j, 0)$. This scattering must be small if the two-beam approximation should be good. The smallness can happen if one of the following reasons occurs: (i) the scattering coefficient $U_{(0,j,0)}$ is 0 or very small or (ii) the excitation error $s_{(0,j,0)}$ is already big. The first case may indeed occur, e.g. for symmetry reasons, however, because beating needs a reasonably large $U_{\mathbf{g}'} = U_{(0,n,0)}$ we also have that $U_{(0,-n,0)} = \overline{U}_{\mathbf{g}'}$ is reasonably large. Hence, in this case only the reason (ii) can be valid, i.e. we need $|s_{(0,-n,0)}| \gg \pi|U_{(0,-n,0)}|/\rho_{(0,-n,0)} \approx 3|U_{\mathbf{g}'}|/|\mathbf{k_0}|$. Using $\sigma_{\mathbf{0}} = \sigma_{\mathbf{g}'} = 0$, the excitation error has the expansion $s_{(0,j,0)} \approx (nj-j^2)/(n|\mathbf{k_0}|)$, which leads with $j = -n$ to the condition $3|U_{\mathbf{g}'}| \ll |n|$, which is not easily satisfied.

Indeed, in [MNS+20] TEM imaging is done under two-beam conditions for $\mathbf{g}' = (0, 4, 0)$, where $U_{(0,j,0)} = 0$ for odd j and $U_{(0,2,0)} \approx -0.05\, U_{(0,4,0)}$. In particular, $j = 4$ was chosen, because it gives the biggest value for $|U_{(0,j,0)}|$ for $j \neq 0$. Nevertheless, it was necessary to base the analysis of the TEM images in the solution $\boldsymbol{\psi}$ of $\mathrm{DHW}_{\Lambda^*_m}$ for $\Lambda^*_m = \Lambda^{*M}_{\mathrm{Ew}}$ obtained via the software package pyTEM. The simple usage of the approximations in (3.32) would not be sufficient.

We will see in Section 3.5 that even in simple examples the two-beam approximation is only a very rough approximation, see e.g. Figure 3.4.

3.4.4 Systematic-row approximation

We choose:

$$\Lambda^*_{\mathrm{syrow}} = \big\{\, n\, \mathbf{g}_* \,\big|\, n_{\min} \le n \le n_{\max} \,\big\},$$

where $\mathbf{g}_*$ is small and almost perpendicular to $\mathbf{k_0}$, such that the convex hull of the set $\Lambda^*_{\mathrm{syrow}}$ is roughly tangent to the Ewald sphere $\mathbb{S}_{\mathrm{Ew}}$. Of course, this set should coincide with $\Lambda^{*M}_{\mathrm{Ew}}$ of Section 3.3.4, which can be achieved by choosing an appropriate $\mathbf{k_0}$. In particular, the case of two-beam conditions of Section 3.4.3 can always be seen as embedded into a systematic-row case.

Indeed, consider the simple dual lattice $\Lambda^* = \mathbb{Z}^3$ and choose $\mathbf{k_0} = (k_x, 0, k_z)$ where now $1 \ll k_x \ll k_z \approx |\mathbf{k_0}|$, i.e. the incoming wave has a small, but nontrivial angle to the normal $\boldsymbol{\nu}$ of the specimen. Assuming $k_x = c_*|\mathbf{k_0}|^{2/3}$ and considering only $\mathbf{g} \in \Lambda^{*M} = B^M(0) \cap \mathbb{Z}^3$ with $M = |\mathbf{k_0}|^{1/4}$, we see that:

$$\sigma_{\mathbf{g}} = |\mathbf{k_0}|^2 - |\mathbf{k_0}{+}\mathbf{g}|^2 \approx -g_x^2 - g_y^2 - g_z^2 - 2c_*|\mathbf{k_0}|^{2/3} g_x - 2|\mathbf{k_0}| g_z,$$

can only take values smaller than $O(|\mathbf{k_0}|^{1/2})$ if the wave vectors satisfy $g_x = g_z = 0$, i.e. $\mathbf{g} = n(0, 1, 0)$ with $|n| \le |\mathbf{k_0}|^{1/4}$, which is a finite row of wave vectors.

Moreover, in Λ^{*M} we have $\rho_{\mathbf{g}} = (\mathbf{k_0}{+}\mathbf{g}) \cdot \boldsymbol{\nu} = |\mathbf{k_0}| + O(|\mathbf{k_0}|^{1/2})$ and conclude:

$$\Lambda^*_{\mathrm{syrow}} := \big\{\, (0, n, 0) \,\big|\, |n| \le |\mathbf{k_0}|^{1/4} \,\big\} = \Lambda^{*M}_{\mathrm{Ew}} := \big\{\, \mathbf{g} \in \Lambda^{*M} \,\big|\, |s_{\mathbf{g}}|/(2\rho_{\mathbf{g}}) < \widehat{\sigma}_* \,\big\}$$
$$\text{with } M = \kappa_*^{3/4}|\mathbf{k_0}|^{1/4} \text{ and } \widehat{\sigma}_* = \kappa_*^{3/2}|\mathbf{k_0}|^{-1/2}.$$

Thus, as for the case of the lowest-order Laue zone we obtain an error estimate.

approximation	Laue zone	systematic row
$(M, \widetilde{\sigma})$	$(\lvert\mathbf{k}_0\rvert^{1/2}, 1)$	$(\lvert\mathbf{k}_0\rvert^{1/4}, \lvert\mathbf{k}_0\rvert^{-1/2})$
number of points	$\lvert\mathbf{k}_0\rvert$	$\lvert\mathbf{k}_0\rvert^{1/4}$
thickness restriction	$z_* \le N_0 \lvert\mathbf{k}_0\rvert^{1/3} \ell_{\text{scatt}}$	$z_* \le N_0 \lvert\mathbf{k}_0\rvert^{1/5} \ell_{\text{scatt}}$
first error term	$\lvert\alpha_* \mathbf{k}_0\rvert^{-2}$	$\lvert\alpha_* \mathbf{k}_0\rvert^{-2}$
second error term	$\dfrac{\alpha_* z_*}{\ell_{\text{scatt}}^2}$	$\dfrac{\alpha_*^{3/2} \lvert\mathbf{k}_0\rvert^{1/2} z_*}{\ell_{\text{scatt}}^2}$

Table 3.2: Comparison of the Laue approximation in Section 3.4.2 and the systematic-row approximation. Reprinted with permission from [KMM21, Fig. 4.3], published by the Society for Industrial and Applied Mathematics (SIAM). Copyright © by SIAM.

Theorem 3.4.3 (Systematic-row approximation)**.** *Under the above assumptions, consider the solutions* $\boldsymbol{\psi}^\gamma$ *and* $\boldsymbol{\psi}_{\text{syrow}}$ *of* $\text{DHW}_{\Lambda^{*\gamma}}$ *with* $\gamma = 1/2$ *and* $\text{DHW}_{\Lambda^*_{\text{syrow}}}$*, respectively. Then, for all* N_0 *there exists* k_* *and* N_1 *such that the following holds:*

$$\textit{If } |\mathbf{k}_0| \ge k_* \textit{ and } z_* \le N_0 |\alpha_* \mathbf{k}_0|^{1/5} \frac{|\mathbf{k}_0|}{C_{\mathbb{U}}}, \textit{ then for all } z \in [0, z_*] \textit{ we have} \tag{3.33a}$$

$$\|\boldsymbol{\psi}_{\text{syrow}}(z) - \boldsymbol{\psi}^\gamma(z)|_{\Lambda^*_{\text{syrow}}}\|_{\Lambda^*_{\text{syrow}}} \le N_1 \Big(\frac{1}{|\alpha_* \mathbf{k}_0|^2} + \frac{\alpha_*^{3/2} C_{\mathbb{U}}^2}{|\mathbf{k}_0|^{3/2}} z_* \Big) \|\boldsymbol{\delta}\| . \tag{3.33b}$$

Proof. Step 1. Reduction to Λ^{*M}. Using $M = \kappa^{3/4} |\mathbf{k}_0|^{1/4}$ and $|\mathbf{k}_0| \ge k_*$ we have $\Lambda^{*M} \subset \Lambda^{*\gamma} = \mathbf{G}_{1/2}$, and Theorem 3.3.6 with $\alpha = \alpha_{\mathbb{U}}/2$ provides the error estimate:

$$\|\boldsymbol{\psi}^M(z) - \boldsymbol{\psi}^\gamma(z)|_{\Lambda^{*M}}\|_{\Lambda^{*M}} \le N_2 \, \mathrm{e}^{N_3 C_{\mathbb{U}} z / |\mathbf{k}_0| - N_4 |\alpha_* \mathbf{k}_0|^{1/4}} \|\boldsymbol{\delta}\|_{\mathbf{G}} .$$

Step 2. Reduction to Λ^*_{syrow}. Applying Theorem 3.3.10 with $\widetilde{s}_* = \kappa_*^{3/2} |\mathbf{k}_0|^{-1/2}$, we obtain the error bound:

$$\|\boldsymbol{\psi}_{\text{syrow}}(z) - \boldsymbol{\psi}^M(z)|_{\Lambda^*_{\text{syrow}}}\|_{\Lambda^*_{\text{syrow}}} \le N_5 \frac{z_*}{\kappa_*^{3/2}} \frac{C_{\mathbb{U}}^2}{|\mathbf{k}_0|^{3/2}} \|\boldsymbol{\delta}\|_{\Lambda^{*M}} . \tag{3.34}$$

Step 3. Combined estimate. We conclude as in Step 3 of the proof of Theorem 3.4.2. □

In contrast to the cut-off choice $\widetilde{\sigma}_* \sim 1$ for the Laue-zone approximation, we have now chosen $\widetilde{s}_* \sim |\mathbf{k}_0|^{-1/2}$. This reduces the number of points in the systematic-row approximation, i.e. the number of coupled ODEs to be solved is proportionally $|\mathbf{k}_0|^{1/4}$, whereas for the Laue-zone approximation, the number of ODEs is proportional to $|\mathbf{k}_0|$. However, the gain in computation power is accompanied by a loss of accuracy and a smaller domain of applicability, see Table 3.2.

$\tilde{g}_z \setminus \tilde{g}_y$	-2	-1	0	1	2	3
-2	-14.07	-14.24	-14.33	-14.33	-14.24	-14.07
-1	-6.87	-7.04	-7.12	-7.12	-7.04	-6.87
0	0.25	0.08	0	0	0.08	0.25
1	7.28	7.12	7.04	7.04	7.12	7.28
2	14.24	14.09	14.00	14.00	14.08	14.24

Table 3.3: Excitation errors $s_{\mathbf{g}} = \sigma_{\mathbf{g}}/(2\rho_{\mathbf{g}})$ for every point $\mathbf{g} = \frac{4}{a_0}(\tilde{g}_y, \tilde{g}_z) \in \Lambda^*_{30}$. The middle row corresponds to beams of the systematic-row approximation. Reprinted with permission from [KMM21, Fig. 5.1], published by the Society for Industrial and Applied Mathematics (SIAM). Copyright © by SIAM.

3.5 Simulations for TEM experiments

Here, we provide a numerical example of the DHW equations, compare the solutions for different choices of the wave-vector set Λ^*_m, and relate the observed errors with the mathematical bounds established above.

In order for our simulations to be as close as possible to values used in real TEM, we choose a lattice constant of $a_0 = 0.56503\,\mathrm{nm}$, which is a typical value for GaAs. The specimen thickness is equal to $z_* = 200a_0 = 113.006\,\mathrm{nm}$. At 400 k eV, as is the case in TEM, the wave length is $\lambda = 1/|\mathbf{k_0}| = 1.644\,\mathrm{pm}$, which in normalized dimensions is $\lambda = 0.00294a_0$. This gives us a wavevector of $|\mathbf{k_0}| = 608.293\,\mathrm{nm}^{-1}$. We consider the full system to consist of 30 beams:

$$\Lambda^*_{30} = \left\{ \mathbf{g} = \frac{4}{a_0}(\tilde{g}_y, \tilde{g}_z) \,\middle|\, \tilde{g}_y \in \{-2, \ldots, 3\} \text{ and } \tilde{g}_z \in \{-2, \ldots, 2\} \right\}.$$

One would expect to use a beam list of the form $\left\{ \mathbf{g} = \frac{1}{a_0}(\tilde{g}_y, \tilde{g}_z) \,\middle|\, \tilde{g}_y, \tilde{g}_z \in \mathbb{Z} \right\}$. But for GaAs, the scattering potential has significant contributions $U_{\mathbf{g}}$ only for beams of the form in Λ^*_{30}, while the other $U_{\mathbf{g}}$ are small or even 0, see Figure 3.3.4. This is due to the face-centered cubic lattice of the crystal and the properties of the Ga and As atomic form factors. Therefore, we restrict our beam list to that case in our example.

For the potential we use $U_{(0,0)} = 10\,\mathrm{nm}^{-2}$, $U_{(\pm1,0)} = U_{(0,\pm1)} = 3\,\mathrm{nm}^{-2}$, and $U_{(\pm1,\pm1)} = U_{(\pm1,\mp1)} = 2\,\mathrm{nm}^{-2}$ and $U_{\tilde{\mathbf{g}}} = 0$ for the rest. We consider strong beam excitation $(\tilde{g}_y, \tilde{g}_z) = (1, 0)$ corresponding to $\mathbf{g} = \frac{1}{a_0}(4, 0)$ and $\mathbf{k_0} = (-2/a_0, 608.293)$.

We first solve the DHW equations for Λ^*_{30} with 30 beams as a reference solution. Note that in 2D there is no distinction between Laue zone and systematic-row approximation. Table 3.3 displays the excitation errors $s_{\mathbf{g}}$: In the middle row, which corresponds to the points close to the Ewald sphere, the entries have a modulus that is more than a factor of 10 smaller than in the rows above and below. We have a zero excitation error at $(0, 0)$ and $(1, 0)$, due to our strong beam excitation condition.

Figure 3.6 shows that the amplitudes of the numerical solutions are related to the excitation

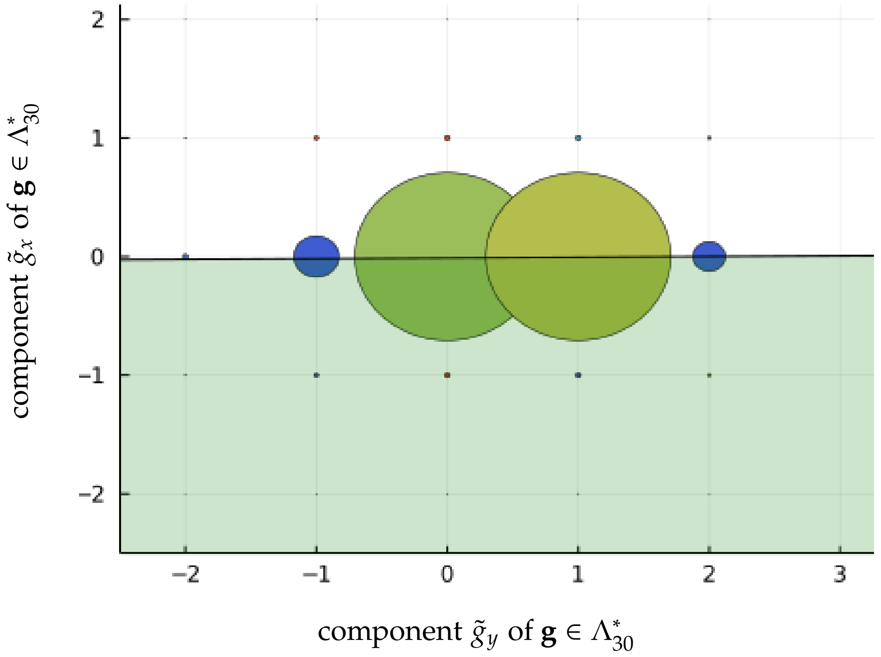

Figure 3.6: The radius of the circles correspond to the amplitudes $|\psi_{\mathbf{g}}(z_*)|$. Close to the Ewald sphere (boundary of light green area), the excitation errors are significantly smaller and the amplitudes are much larger. All simulations are done in Julia. Reprinted with permission from [KMM21, Fig. 5.2], published by the Society for Industrial and Applied Mathematics (SIAM). Copyright © by SIAM.

errors. For each beam $\mathbf{g}$, we plot a circle with center $(\tilde{g}_y, \tilde{g}_z)$ and radius proportional to $|\psi_{\mathbf{g}}(z_*)|$. We see that near the Ewald sphere, where the excitation error is small, the amplitude is significantly higher. It becomes obvious that there are four main modes, corresponding to the beams $(-1,0)$, $(0,0)$, $(1,0)$, and $(2,0)$.

Next, we reduce the beam list Λ_{30}^* to observe how the errors of the solutions change. We create three sets corresponding to the systematic-row approximation:

$$\begin{aligned}
\Lambda_2^* &= \Big\{ \mathbf{g} = \frac{4}{a_0}(\tilde{g}_y, \tilde{g}_z) \,\Big|\, \tilde{g}_y \in \{0,1\} \text{ and } \tilde{g}_z \in \{0\} \Big\},\\
\Lambda_4^* &= \Big\{ \mathbf{g} = \frac{4}{a_0}(\tilde{g}_y, \tilde{g}_z) \,\Big|\, \tilde{g}_y \in \{-1,\cdots,2\} \text{ and } \tilde{g}_z \in \{0\} \Big\},\\
\Lambda_6^* &= \Big\{ \mathbf{g} = \frac{4}{a_0}(\tilde{g}_y, \tilde{g}_z) \,\Big|\, \tilde{g}_y \in \{-2,\cdots,3\} \text{ and } \tilde{g}_z \in \{0\} \Big\},
\end{aligned}$$

where the set Λ_2^* corresponds to the two-beam case, shown in Figure 3.7. For comparison, we also create a set including beams above and below the Ewald sphere:

$$\Lambda_{18}^* = \Big\{ \mathbf{g} = \frac{4}{a_0}(\tilde{g}_y, \tilde{g}_z) \,\Big|\, \tilde{g}_y \in \{-2,\cdots,3\} \text{ and } \tilde{g}_z \in \{-1,\cdots,1\} \Big\}.$$

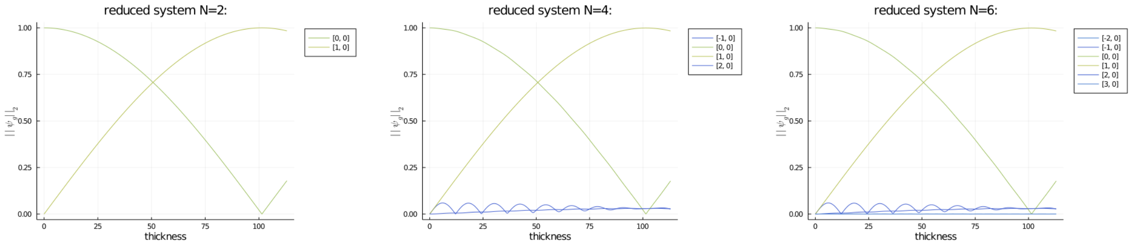

Figure 3.7: Beam amplitudes $|\psi_{\mathbf{g}}(z)|$ of solutions for the three choices Λ^*_2, Λ^*_4, and Λ^*_6. The same beating of the two main modes is observed in all the cases. Reprinted with permission from [KMM21, Fig. 5.3], published by the Society for Industrial and Applied Mathematics (SIAM). Copyright © by SIAM.

System	$(0, 0)$ mode	$(1, 0)$ mode	digits
Λ^*_2	$-\underline{0.16}153606468 - \underline{0.077}40830300\,\mathrm{i}$	$\underline{0.4}2515771142 - \underline{0.8}8721717658\,\mathrm{i}$	1
Λ^*_4	$-\underline{0.1644}6909478 - \underline{0.0676}6454587\,\mathrm{i}$	$\underline{0.3779}0257701 - \underline{0.9077}5029000\,\mathrm{i}$	4
Λ^*_6	$-\underline{0.1644}5260546 - \underline{0.067648}75833\,\mathrm{i}$	$\underline{0.377}89496977 - \underline{0.9077}5362575\,\mathrm{i}$	4
Λ^*_{18}	$-\underline{0.1644425}2690 - \underline{0.0676480}8597\,\mathrm{i}$	$\underline{0.377914}10830 - \underline{0.9077468}3865\,\mathrm{i}$	7
Λ^*_{30}	$-0.16444251537 - 0.06764807576\,\mathrm{i}$	$0.37791412093 - 0.90774682391\,\mathrm{i}$	—

Table 3.4: Comparison of solutions for $\tilde{g} = (0, 0)$ and $\tilde{g} = (1, 0)$. The underlined decimals indicate which numbers are already correct (up to rounding) with respect to the last line, i.e. we take the Λ^*_{30} system as reference. Reprinted with permission from [KMM21, Fig. 5.4], published by the Society for Industrial and Applied Mathematics (SIAM). Copyright © by SIAM.

From Figure 3.7 we have a first qualitative comparison for the systematic-row cases. We see that the qualitative features, meaning the beating and the two main modes, namely $(0, 0)$ and $(1, 0)$, are captured in every case. The two-beam case however fails to capture the other two main modes, for $(-1, 0)$ and $(2, 0)$.

To obtain a quantitative comparison of the different models, we show the numerical values of $\psi_{(1,0)}(z_*)$ and $\psi_{(2,0)}(z_*)$ in Figure 3.4. As a first observation we see that the two-beam case has only one significant digit correct, making it a very rough approximation. Moving to Λ^*_4 with four beams gives an accuracy of 4 significant digits, while increasing the size of the systematic-row approximation further does not bring higher accuracy as Λ^*_6 with six beams still has only four significant digits. The accuracy of the solutions is however further improved to 7 significant digits by adding the layer above and below the Ewald sphere in the Λ^*_{18} system, which has 18 beams.

For comparing numerical errors with the mathematical error bounds in Figure 3.2, we observe that the scattering length is $\ell_{\text{scatt}} = \frac{|\mathbf{k_0}|}{|C_U|} = 60.83\,\text{nm} \approx z_*/2$. Choosing $\alpha_* = a_0 = 0.565\,\text{nm}$ and using $|\mathbf{k_0}| = 0.608 \cdot 10^{12}\,\text{m}^{-1}$, we find the error terms:

$$|\alpha_* \mathbf{k_0}|^{-2} = 0.0000084647989 \lll 1 \quad \text{and} \quad \frac{\alpha_* z_*}{\ell^2_{\text{scatt}}} = 0.01735570 \ll 1,$$

which are indeed small for the chosen setup.

For many practical purposes, like the simulation of TEM images with pyTEM as in [Nie19], an accuracy of 4 significant digits is certainly good enough. However, for other applications higher accuracy may be needed, e.g. for detecting phase differences for beams of low amplitudes like in electron holography, see e.g. [Lic13].

In fact, the software pyTEM creates a beam list Λ_m^* in the following way. It first restricts to the LOLZ or systematic-row approximation by setting $g_z = 0$. Next, a minimum for $|U_{\mathbf{g}}|$ is chosen to restrict to the sublattice generated by those $\mathbf{g}$ with $|U_{\mathbf{g}}| \geq u_{\min}$. For instance, the coefficients displayed in Figure 3.3(b) lead to the sublattice $\left\{ \mathbf{g} = \frac{1}{a_0}(0, 2m, 0) \,\middle|\, m \in \mathbb{Z} \right\}$. Finally, a maximum value $\widetilde{s}_*$ is chosen for the excitation error $s_{\mathbf{g}}$, which leads to a final systematic row approximation with 12 beams with $m \in \{-5, \ldots, 6\}$. In the next chapter, we will use the software package pyTEM to create a database of simulated TEM images of quantum dots. To do so, the DHW equations are coupled with the strain profile, which is calculated using elasticity theory.

Chapter 4

Simulated TEM Images of Quantum Dots

Quantum dots (QD) are semiconductor nanostructures with interesting optoelectronic properties that are determined by their geometry and are used in many different fields, like lasers, quantum cryptography and quantum metrology. The growth of semiconductor QDs with desired electronic properties would highly benefit from the assessment of QD geometry, distribution and strain profile in a feedback loop between epitaxial growth and analysis of their properties. TEM can in principle be used to assist such an optimization loop of QDs. However, the reconstruction of the geometric properties of QDs from TEM images is a difficult problem due to the limited image resolution (0.5-1nm), the highly nonlinear behavior of the dynamic electron scattering, non-local effects due to strain and strong stochastic influences due to uncertainties in the experiment. In contrast to what is common for images from light microscopy, for TEM imaging of QDs there is no simple one-to-one correspondence between the TEM image, which rather shows the so-called *coffee-bean contrast*, and the shape of the QD.

Here, we present a mathematical model and a toolchain for the numerical simulation of TEM images of semiconductor quantum dots (QDs). This includes elasticity theory to obtain the strain profile coupled with the Darwin-Howie-Whelan equations, describing the propagation of the electron wave through the sample. We perform a simulation study on indium gallium arsenide QDs with different shapes and compare the resulting TEM images to experimental ones. This toolchain is used to generate a database of simulated TEM images, which is a key element for a model-based geometry reconstruction of semiconductor QDs, involving machine learning techniques. The work presented here was published in [MNS+20] and the chapter follows closely the structure of that paper, with some additional explanation of the theory behind the simulation in Sections 4.2 and 4.3.

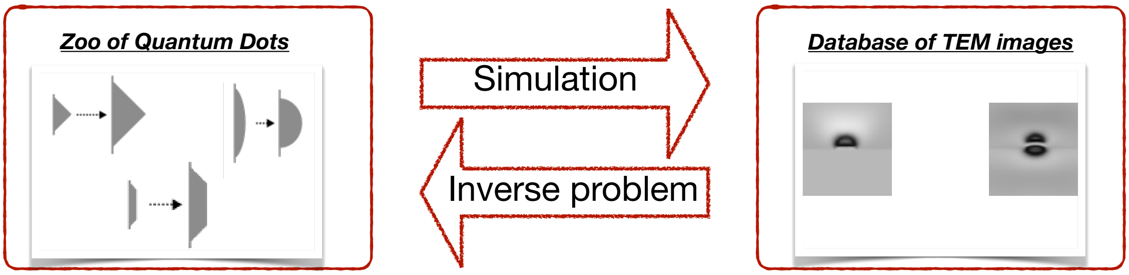

Figure 4.1: MBGR approach: By the numerical simulation of the imaging process, a database of simulated TEM images spanning the image space for a large number of possible QD configurations and image acquisition parameters is generated. This simulated image space can then be explored by means of statistical methodology, for example by shape space methods, functional data analysis, or deep learning. Such methods can then be used for inferring the geometry of QDs from experimental TEM images.

4.1 Model based geometry reconstruction approach

In [KMN+18; MKN+18], we introduced a novel concept for 3D *model-based geometry reconstruction* (MBGR) of QDs from TEM imaging. The approach was based on (a) an appropriate model for the QD configuration in real space, including a categorization of QD shapes (e.g. pyramidal or lens-shaped) and continuous parameters (e.g. size, height), (b) a database of simulated TEM images covering a large number of possible QD configurations and image acquisition parameters (e.g. bright field/dark field, sample tilt), as well as (c) a statistical procedure for the estimation of QD properties and classification of QD types based on acquired TEM image data. The idea is illustrated in a simple way in Figure 4.1. First, we simulate TEM images of as many QD configurations as possible. Then, we use this simulated database for the QD classification and properties estimation. This second part, the inverse problem, is still work in progress so we will not focus on that here. The first part, the simulation process, is completed and the results are published in [MNS+20] as mentioned before.

To simulate the TEM images, we combined two software packages. First the WIAS-pdelib software [FS+19] is used in order to calculate the displacement (also the strain and stress) for a specific geometry and indium concentration. The output from this then enters the pyTEM software [Nie19], which simulates a TEM image for chosen excitation conditions by solving the DHW equations numerically. The database we created concerns indium gallium arsenide QDs embedded in a gallium arsenide matrix. The simulation process is shown in Figure 4.2. To have a better understanding of the simulation process we will explain next how the displacement enters the equations and how we calculate this displacement using elasticity theory.

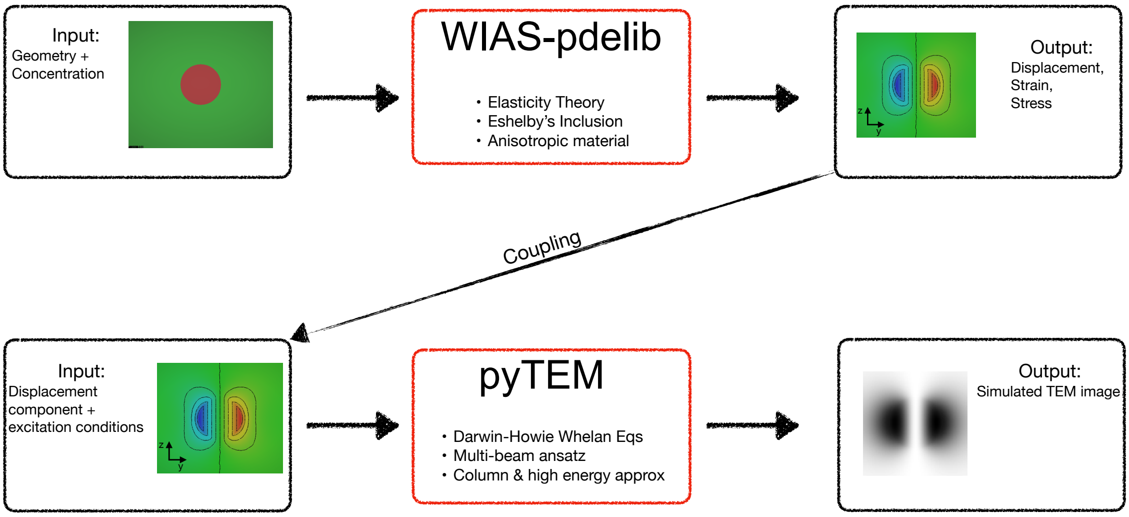
Input:
Geometry +
Concentration
WIAS-pdelib
• Elasticity Theory
• Eshelby's Inclusion
• Anisotropic material
Output:
Displacement,
Strain,
Stress
Coupling
Input:
Displacement
component +
excitation conditions
pyTEM
• Darwin-Howie Whelan Eqs
• Multi-beam ansatz
• Column & high energy approx
Output:
Simulated TEM image

Figure 4.2: Simulation of TEM images: First the displacement is calculated from WIASpdelib solver for a specific geometry and indium concentration. Then this enters the pyTEM solver, which creates a simulated TEM image for chosen excitation conditions.

4.2 Influence of strain in the DHW equation

TEM imaging is widely used for the study of defects in crystalline materials, see [PHN+18; WS19; SS93; ZD20]. By defects we mean perturbations of the crystal symmetry, in the sense that the atoms are displaced from their original position in the perfect crystal. If an atom was at position $\mathbf{r}$, its new position will be $\mathbf{r}' = \mathbf{r} + \mathbf{u}(\mathbf{r})$, where $\mathbf{u}(\mathbf{r})$ is the displacement field, see Figure 4.3 a). In the next section, we will describe how the displacement field is calculated in WIAS-pdelib, but for now we give an elementary example in order to understand how a strained crystal looks likes. We consider a spherical particle with radius r_0 and lattice parameter a_p inside a matrix with lattice parameter a_m, as is done in [De 03, Ch.8, p.479]. The displacement field is given by:

$$\mathbf{u}(\mathbf{r}) = C(\delta)\frac{\left(\min\{|\mathbf{r}|, r_0\}\right)^3}{|\mathbf{r}|^3}\,\mathbf{r}, \tag{4.1}$$

where $C(\delta)$ is a constant that depends on the elastic properties of the isotropic matrix and δ the matrix misfit given by $\delta = (a_p - a_m)/a_m$. In this case, the displacement inside the particle is proportional to $\mathbf{r} = (x, y, z)$, whereas outside it decays as $1/|\mathbf{r}|^2$, see Figure 4.3. The displacement field $\mathbf{u}$ is only valid for small isotropic inclusions where the particle diameter is significantly smaller than one extinction distance.

For small deformations the displacement will modify the Fourier coefficients of the potential in the DHW equations (3.4) by a phase factor:

$$U_{\mathbf{g}} \to U_{\mathbf{g}} e^{-2i\pi\mathbf{g}\cdot\mathbf{u}(\mathbf{r})}.$$

Using this and letting $\psi_{\mathbf{g}} = \varphi_{\mathbf{g}} e^{-2i\mathbf{g}\cdot\mathbf{u}(\mathbf{r})}$ in (3.4), we get the DHW equations for a strained crystal [De 03, Ch.8]:

$$\frac{\mathrm{d}}{\mathrm{d}z}\varphi_{\mathbf{g}}(z) = 2i\pi\Big(s_{\mathbf{g}} + \frac{\mathrm{d}}{\mathrm{d}z}(\mathbf{g}\cdot\mathbf{u}(\mathbf{r}))\Big)\varphi_{\mathbf{g}}(z) + \frac{i\pi}{\rho_{\mathbf{g}}}\sum_{\mathbf{h}\in\Lambda_m^*} U_{\mathbf{g}-\mathbf{h}}\varphi_{\mathbf{h}}(z) \tag{4.2}$$

$$\text{and } \varphi_{\mathbf{g}}(0) = \delta_{\mathbf{0},\mathbf{g}} \quad \text{for } \mathbf{g} \in \Lambda_m^*. \tag{4.3}$$

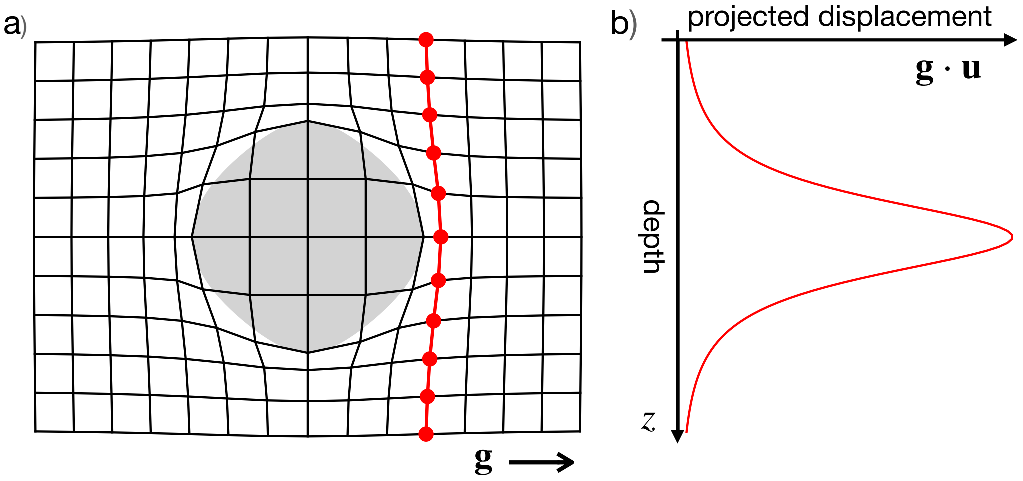

Figure 4.3: Crystal lattice with spherical inclusion: a) Deformation of the lattice b) Variation of the projection of the displacement **u** on the **g** vector along the line scan in z-direction (red) in the crystal.

The set Λ_m^* is a subset of the dual lattice Λ^* containing $m-$beams. To simulate a TEM image with defects, the displacement $\mathbf{u}(\mathbf{r})$ in (4.2) is evaluated as $\mathbf{u}(z; x_i, y_j)$, for each horizontal position (x_i, y_j), where (i, j) denotes the image pixel. If this is constant, then the defect will not be visible. Another important fact for the imaging of defects is that the projection of the displacement to the reciprocal lattice vector **g** is what really matters, see Figure 4.3 b). If $\mathbf{g}\cdot\mathbf{u}(\mathbf{r})$ is constant, then again the defect is not visible. This means that by choosing different vectors $\mathbf{g}_{\mathrm{ap}}$ we get different information about the defect. In [MNS+20] we also took into account the indium content $c(\mathbf{r})$, which enters the Fourier coefficients as:

$$U_{\mathbf{g}} \to \left[c(\mathbf{r})U_{\mathbf{g}}^{\mathrm{InAs}} + (1 - c(\mathbf{r}))U_{\mathbf{g}}^{\mathrm{GaAs}}\right] e^{-2\pi i \mathbf{u}(\mathbf{r})\cdot\mathbf{g}}. \tag{4.4}$$

More on how the displacement influences the TEM images will be discussed in the next chapter. Now we give a brief introduction to elasticity theory to have a better picture of the simulation process shown in Figure 4.2.

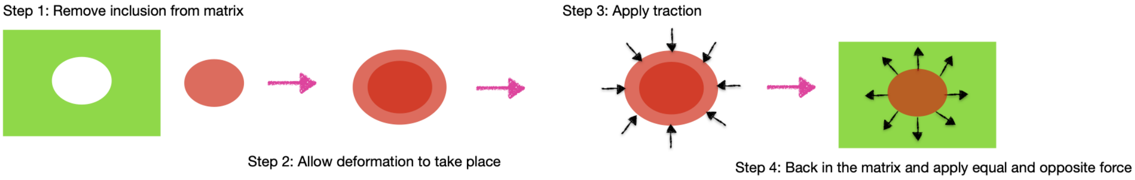
Step 1: Remove inclusion from matrix
Step 2: Allow deformation to take place
Step 3: Apply traction
Step 4: Back in the matrix and apply equal and opposite force

Figure 4.4: Eshelby's method briefly described in four steps. Step 1: Remove inclusion from the matrix. Step 2: Allow deformation to take place. Step 3: Apply traction to bring the inclusion to its original form. Step 4: Put inclusion back in the matrix and apply an equal and opposite force.

4.3 Elasticity theory and Eshelby's method

The dynamical electron scattering in crystalline solids, e.g. semiconductor nanostructures, is influenced by spatial variations in the material composition and by local deformations of the lattice due to elastic strain. In order to model the TEM images, we need to use elasticity theory to obtain the strain profile and couple this with the Darwin-Howie-Whelan equations (4.2).

The indium gallium arsenide QDs under consideration and the surrounding GaAs matrix have different lattice constants. This induces mechanical stresses in the nanostructure. The strain tensor is defined as $\varepsilon(\mathbf{u}) = \frac{1}{2}\left(\nabla\mathbf{u} + (\nabla\mathbf{u})^T\right)$, where $\mathbf{u}$ is the displacement and the stress σ is linked to the strain by Hooke's law $\sigma = \mathbf{C}\varepsilon$. Here, $\mathbf{C}$ is the elastic stiffness tensor, see Appendix A.

We model the elastic relaxation of the misfit-induced strain following the concept of Eshelby's inclusion [Esh57]. The approach was developed for the description of the elastic relaxation within and around *inclusions* of a solid surrounded by a *matrix*. The GaAs matrix provides a *global reference* for measuring displacements and strains. For simplicity, we assume that both matrix and inclusion (QD) exhibit cubic symmetry. Eshelby's approach was the following: First, remove the inclusion from the matrix and let the unconstrained transformation take place. Now the inclusion will assume a uniform strain ε^* and experience zero stress. This strain under zero stress is called *eigenstrain*. From the eigenstrain the *eigenstress* σ^* is defined as:

$$\sigma^* = \mathbf{C}\varepsilon^*. \tag{4.5}$$

Next, apply surface tractions such that the inclusion is restored to its original form. Put the inclusion back in the matrix and rejoin the material across the cut. Now, the stress in the matrix is zero and has a known value in the inclusion. The applied surface tractions form a layer of body force over the interface between inclusion and matrix. To remove this unwanted layer, apply an equal and opposite layer of body force. Figure 4.4 illustrates these steps.

If we remove the inclusion from the matrix, it is stress-free, if the strain ε of the reference system equals the eigenstrain ε^*. Assuming a stress-strain relation according to Hooke's law, we can mimic the stress-free condition for $\varepsilon = \varepsilon^*$ in the reference system of the matrix by incorporating the eigenstress in the momentum balance:

$$\nabla \cdot (\sigma - \sigma^*) = 0. \tag{4.6}$$

The boundary condition on the Neumann part of the boundary (stress-free relaxation) has to be modified accordingly:

$$(\sigma - \sigma^*) \cdot \mathbf{n} = 0. \tag{4.7}$$

We will not expand further into Eshelby's method or elasticity, but the interested reader is encouraged to read the original paper from Eshelby [Esh57] or a relevant book like [Mur82].

4.4 Numerical simulation of TEM images for different geometries

A simulated TEM image is generated by propagating the beams through the specimen for every pixel (i, j), $i, j = 1, \dots, N$. This is done numerically by solving the Darwin-Howie-Whelan equations (4.2) using displacements $\mathbf{u}$ obtained from the elasticity problem (4.6) for a given geometry.

The excitation errors $s_{\mathbf{g}}$, entering the Darwin-Howie-Whelan equations, depend on the orientation of the crystallographic lattice with respect to the beam direction. The specimen can be oriented such that only a small number of beams $\mathbf{g}$ with amplitudes $\phi_{\mathbf{g}}$ are excited. For two-beam conditions, the Ewald sphere only cuts two reciprocal lattice points. Thereby, most of the intensity is contained within the undiffracted ϕ_0 and a single diffracted beam $\phi_{\mathbf{g}'}$ while the other beams remain largely unexcited.

In imaging conditions, where the objective aperture selects only a single beam $\mathbf{g_{ap}}$, the image contrast is simply obtained by taking the square of the modulus of the beam's amplitude at the exit plane $z = z_*$:

$$I_{\mathbf{g_{ap}}}(i, j) = |\phi_{\mathbf{g_{ap}}}(z_*; x_i, y_j)|^2. \tag{4.8}$$

For example, for excitation of (040)-two-beam conditions, the bright field is given by $I_{\mathbf{0}}(i, j)$ while the dark field image is given by $I_{\mathbf{g}'}(i, j)$ with $\mathbf{g}' = (040)$.

4.4.1 Toolchain for simulation of TEM images

The simulation toolchain starts with a parametric geometry description of the QD shape, e.g. using base length and height of the pyramidal QD. A representation of the geometry by a tetrahedralization is created using the 3D mesh generator TetGen [Si15], see Figure 4.7a. The generated mesh enters a FEM-based elasticity solver of WIAS-pdelib [FS+19] which computes the strain profile and the displacement field $\mathbf{u}$ in the QD and in the sample. Finally, the multi-beam solution is obtained by the Darwin-Howie-Whelan solver pyTEM [Nie19] depending on excitation conditions and the sample orientation and results in the simulated TEM image. For the examples shown in the following, we assumed an acceleration voltage of 300 kV. The x and y range of the simulated TEM images is -50 nm to 50 nm around the center of the quantum dot, sampled with 101 points. The beams used are chosen from (020) systematic row for the (040) reflection and (002) systematic row for the (004) reflection. From these, the beams with the smallest excitation error were used (6 beams in our case).

4.4.2 Spherical QD

As a first example, we consider a spherical InAs QD with radius 10 nm embedded in a GaAs matrix. Figure 4.5b shows the dark field TEM image under (040)-two-beam conditions, revealing a coffee-bean like contrast which looks similar to the experimental results shown in Figure 2.2. For comparison Figure 4.5a shows a simulated TEM image using in Eq. (4.4) the effect of the material contrast only, neglecting strain effects. Even the qualitative behavior differs strongly from the results of the fully-coupled simulation (Figure 4.5b) and from the experimental observations (Figure 2.2). This demonstrates that the TEM contrast is dominated by the strain profile around the QD, shown in Figure 4.5c, and the nonlocal behavior of the mapping QD geometry (sphere) to TEM image (coffee-bean).

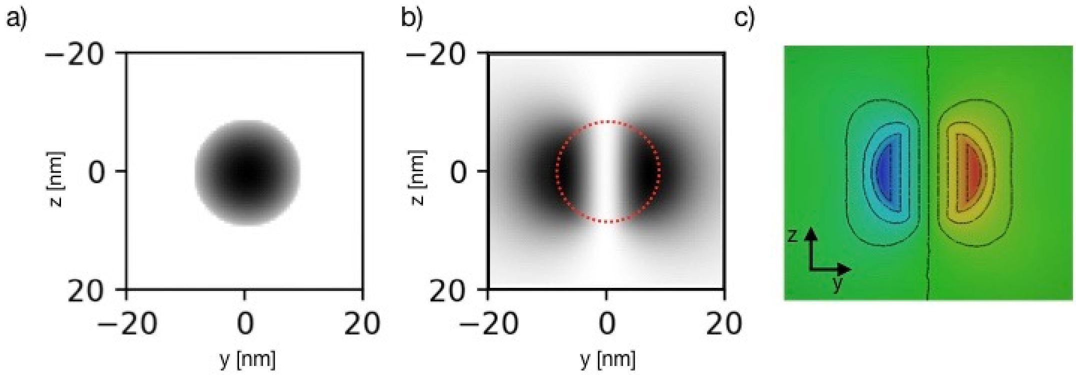

Figure 4.5: Simulated TEM images: (a) dark field for material contrast only (b) dark field also including influence of strain. The image contrast in (a) is strongly increased for better visualization. Due to the excitation under (040)-two-beam conditions, the image contrast is sensitive to the [010]-component of the displacement field, shown in (c) along a cross-section through the center of a spherical InAs QD as obtained by FEM. © 2018 IEEE. Reprinted, with permission, from [KMN+18].

4.4.3 Pyramidal and lens-shaped QDs

For more realistic QD TEM images, we study QDs with two different shapes: lens-shaped QDs with circular base (diameter of 15 nm) and (truncated) pyramidal QDs (baselength of 15 nm) with different vertical aspect ratios, respectively, and a thin wetting layer, see Figure 4.6 and Figure 4.7a. We assume an indium content of 80% for all cases.

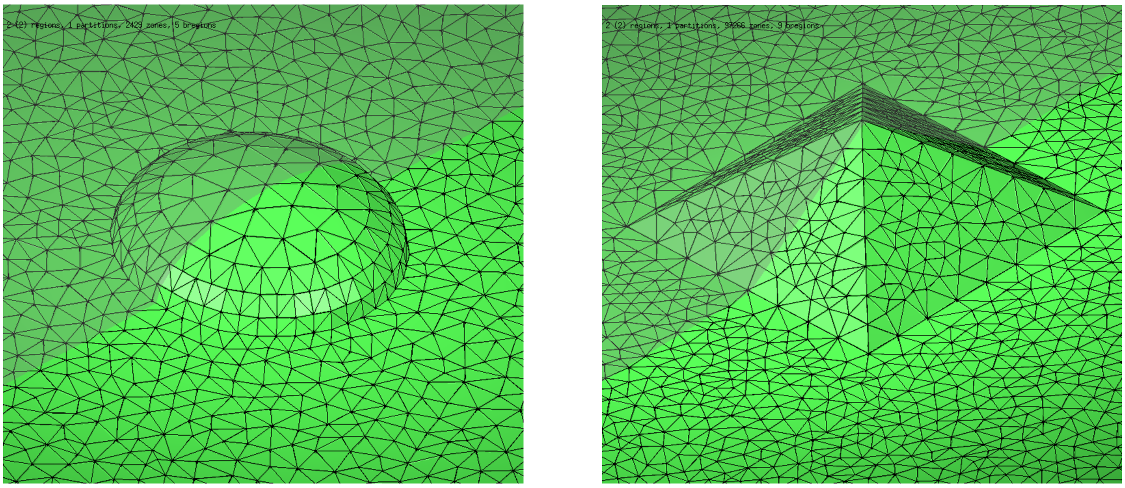
2 (2) regions, 1 partitions, 2429 zones, 5 bregions
2 (2) regions, 1 partitions, 97266 zones, 9 bregions

Figure 4.6: 3D view of the geometry of a lens-shaped and a pyramidal quantum dot. The shadow indicates the cutting plane for the cross sections shown in Figure 4.7. Reprinted from [MNS+20] under CC-BY.

For comparison with the experimental TEM images shown in Figure 2.2, we simulated TEM images for the same excitation conditions, namely (040)- and (004)-two-beam conditions, see Figure 4.7c and Figure 4.7e, respectively. Consequently, the image contrast is sensitive to the y- and x-component of the displacement field, shown in Figure 4.7b and Figure 4.7d along a yx-cross section through the center of the QDs, respectively.

For both, pyramidal and lens-shaped QDs, a coffee-bean like contrast can be found for (040)-two-beam conditions as it is also observed in the experimental data, see Figure 2.2. However, for (004)-two-beam conditions we observe a striking difference between the images: The pyramidal QDs produce more a crescent-like contrast, whereas the contrast for the lens-shaped QDs resembles the coffee-bean contrast again. This can be explained by the different behavior of the elastic relaxation of the misfit induced strain: For lens-shaped structures the relaxation takes place in the QD as well as below and above it, while for pyramidal ones it is mainly concentrated in the QD itself and above, see Figure 4.7d.

Another observation we can make from the simulated images is a line of no contrast across the center of lens-shaped QDs only. This characteristic feature is also observed experimentally, see Figure 2.2. Therefore, even on the basis of the four different QD shapes we studied, one can already conclude that a lens-shaped structure matches the experimental observations much better than pyramidal structures (truncated or not), see

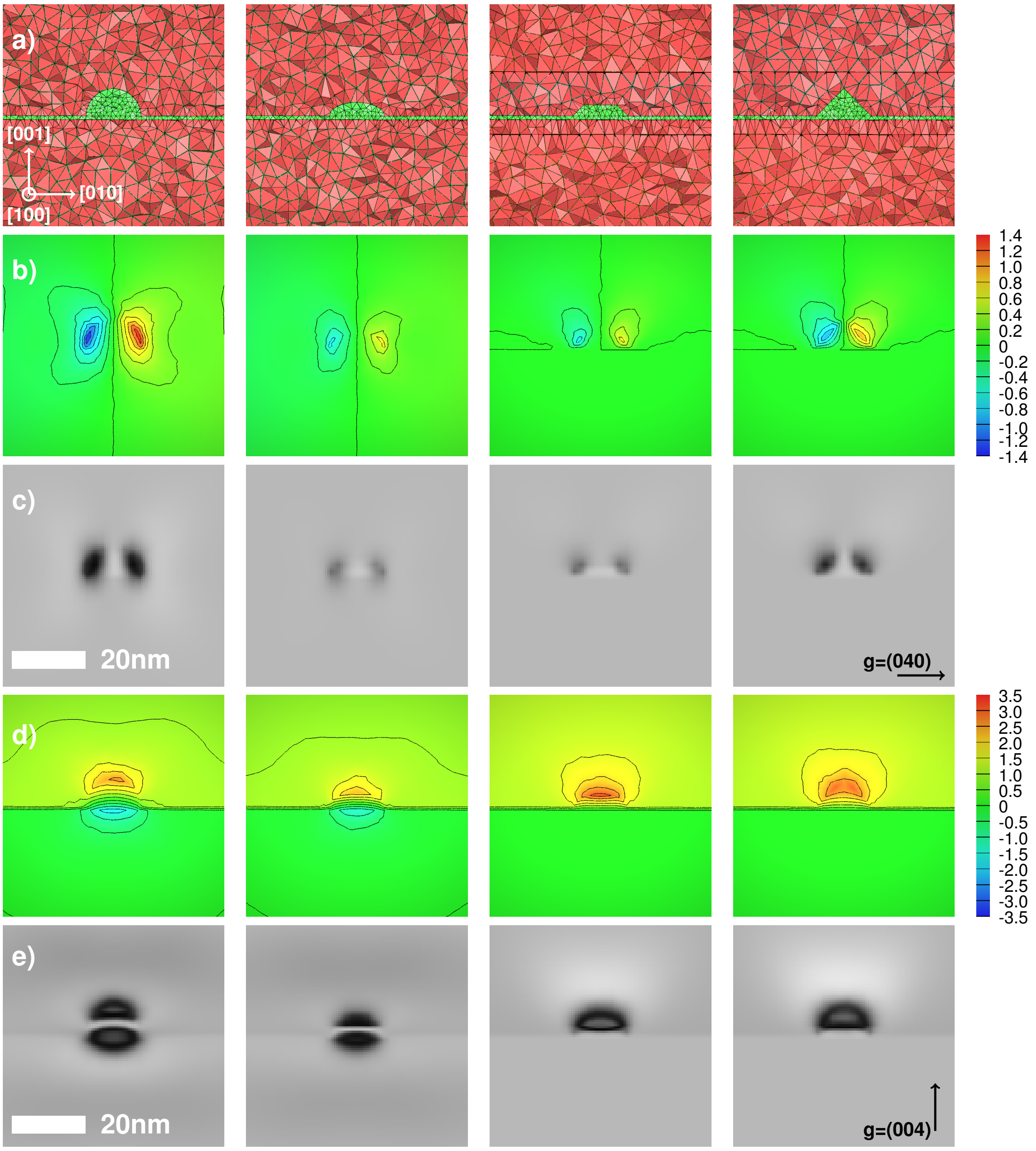

Figure 4.7: InGaAs (green) quantum dots (indium content 80%) embedded in a GaAs (red) matrix with different shapes: Lens-shaped QDs with circular base (two left columns) and pyramidal QDs (two right columns) with different vertical aspect ratios, respectively. FEM simulation of the elastic relaxation of the misfit induced strain: (a) Geometry and FEM mesh, where we made a cut through the mesh by cell removal, so the colour changes occur due to light reflections from the remaining tetrahedra. (b) u_y component and (d) u_z component of the displacement field along a yz-cross-section through the center of the QDs in Å. The strain fields are not fully symmetric because we used an unstructured and coarse mesh. Simulated TEM images for two different excitations: (c) Dark field for (040) beam for excitation under (040) two-beam conditions and (e) Dark field for (004) beam for excitation under (004) two-beam conditions. The sample thickness is 150 nm and for the wavevector we have $|\mathbf{k_0}| = 507.93\ \text{nm}^{-1}$. All images show the same 60 nm x 60 nm field of view. Reprinted from [MNS+20] under CC-BY.

comparison in Figure 4.8.

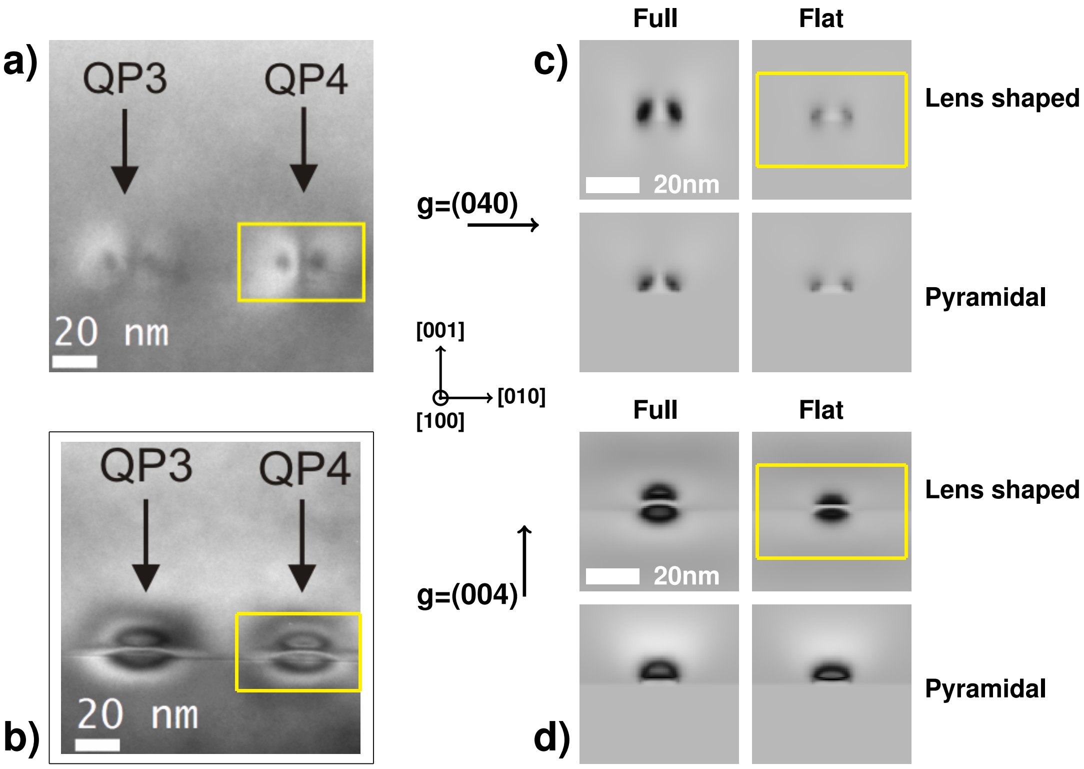

Figure 4.8: Experimental images (a, b) from Figure 2.2 compared to simulated images (c, d) of InGaAs quantum dots (indium content 80%) embedded in a GaAs matrix from Figure 4.7. From top left to bottom right the shapes are lens-shaped, flat lens, full pyramid and truncated pyramid. Dark field images are shown for the (040) beam (a, c) and the (004) beam (b, c). The yellow boxes indicate the same areas in both experimental and simulated TEM images. For the wavevector we have $|\mathbf{k}_0| = 507.93\ \mathrm{nm}^{-1}$. Reprinted from [MNS+20] under CC-BY.

4.5 Database of TEM images

Using the toolchain described above, we generated a database of TEM images for initially two classes of geometries: Pyramidal and lense-shaped QDs, see Figure 4.6. This database contains images for different QD geometry parameters (baselength, aspect-ratio, concentration, position) and excitation parameters (acceleration voltage, beam directions). As an example, we show a series of specimen parameter variations for a lens-shaped InGaAs quantum dot embedded in a GaAs matrix: different values of the sample thickness in Figure 4.9a, the size of the QD in Figure 4.9b, the indium content in Figure 4.9c and the position of the QD in the matrix relative to the top surface in Figure 4.9d. A SQL-database is used to store the metadata of the images including the actual values of the parameters, the numerical parameters controlling the solvers, and the file locations. The consistency of parameters and data across the toolchain is ensured by using portable metadata descriptions in JavaScript Object Notation (JSON).

Here, it is worth mentioning that our computational toolchain is not restricted to QDs, but can be applied also to other epitaxial heterostructures or coherent precipitates. This includes the surface relaxation of thin TEM lamellas or structures with spatially varying material composition, e.g. the QDs with varying indium content in our case.

Our study on four different QD shapes showed a strong sensitivity of image contrast to the characteristic profiles of the strain field. The influence of the strain profile on the TEM image will be the subject of our next chapter, where we will focus on symmetries observed in TEM images.

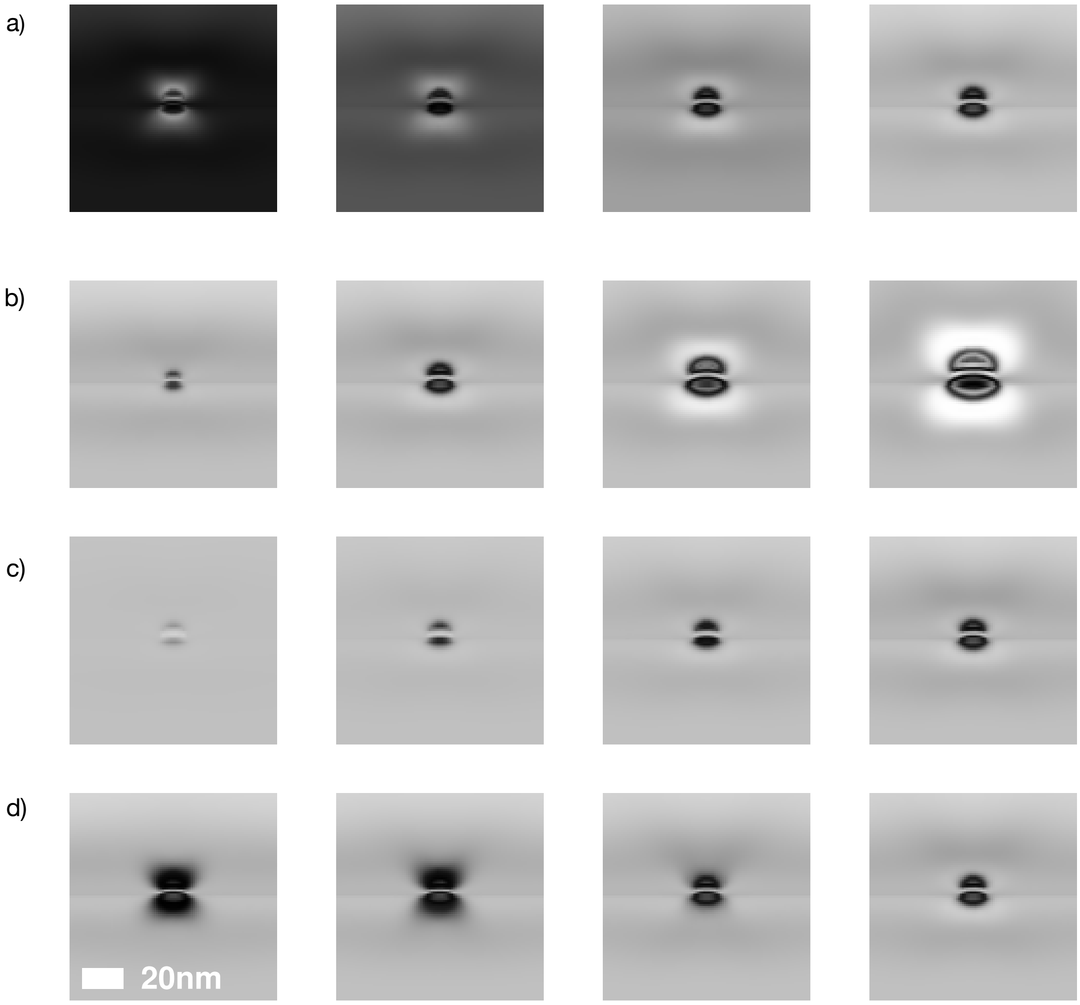

Figure 4.9: InGaAs lens-shaped quantum dots embedded in a GaAs matrix. Dark field images for (040) two-beam conditions: (a) thickness variation 120 nm, 130 nm, 140 nm, 150 nm, size of QD 15 nm, indium content 80%, position of QD at 75 nm (b) size variation 10 nm, 15 nm, 20 nm, 25 nm, sample thickness 150 nm, indium content 80%, position of QD at 75 nm (c) indium content variation 20%, 40%, 60%, 80%, sample thickness 150 nm, QD size 15 nm, position of QD at 75 nm (d) position variation along the beam direction 45 nm, 55 nm, 65 nm, 75 nm, size of QD 15 nm, indium content 80%, sample thickness 150 nm. All images have the same gray scaling. Black corresponds to no intensity while white corresponds to the intensity of the incoming beam. For the wavevector we have $|\mathbf{k}_0| = 507.93\ \mathrm{nm}^{-1}$. Reprinted from [MNS+20] under CC-BY.

Chapter 5

Symmetries in TEM imaging of strained crystals

The main goal of transmission electron microscopy is to extract information on the specimen from the generated TEM images. This is particularly used for detecting shapes, sizes and composition of defects or inclusions like quantum wells and quantum dots in a larger specimen consisting of a regular crystalline material. However, there is no direct way to infer the inclusion properties from the TEM image. Hence, a commonly taken approach that was described in the previous chapter is to simulate the TEM imaging process with inclusions being described by parametrized data. Then, the comparison with experimental pictures can be used to fit the chosen parameters and deduce the desired data of the experimental inclusions.

A main feature in this process are symmetries for two reasons; first the inclusions may have certain symmetries and second the TEM images may display symmetries that are related but not identical. The latter arise from the fact that the experimental setup may have its own intrinsic symmetry properties. In this chapter, we will analyze these symmetries and explain why sometimes TEM images look more symmetric than the inclusion under investigation, or as the Curie's principle is stated in [CI16] (a3): *the effect is more symmetric than its cause*.

The interest in TEM image symmetries dates back to the 1960'-70's, cf. [HW61; ISW74], with the work focused mainly on the Reciprocity Theorem. It states that *the amplitude at a point B of a wave originating from a source at point A and scattered by a potential V is equal to the scattered amplitude at point A originating from the same source at B*. Many papers have been written for alternative proofs of this theorem, cf. [BFT+64; PT68; Moo72; QG89], as well as applications of it in the interpretation of TEM images, e.g. in connection with imaging of dislocations, cf. [FTK+72; HWM62; Kat80].

While some of our results can also be deduced from the reciprocity theorem, like mid-plane reflection, there are more symmetries in the imaging process which can be proven mathematically by assuming the column approximation and focusing on the Darwin–Howie–Whelan equations. Combining the symmetry properties of the imaging process with symmetry properties of the inclusion explains extra symmetries observed in TEM images of strained crystals. The work presented in this chapter is currently under review and a preprint can be found in [KMM22].

The structure of this chapter is as follows: In Section 5.1 we provide a short introduction of what we mean by image symmetries related to the DHW equations. In Section 5.2 we discuss all issues concerning symmetries in TEM imaging by considering well-chosen examples. In particular, we highlight the relevance of the symmetries for the detection of shapes of inclusions. The mathematically rigorous treatment of the symmetries for the m-beam model is given in Section 5.3, where the notion of weak and strong symmetries is introduced to provide a coherent structure of the symmetry properties, which also reveals why the two-beam case is different from the m-beam case with $m > 2$.

5.1 Image symmetries via the DHW equations

The Darwin–Howie–Whelan equations, describing the propagation of electron beams through crystals, were already introduced in Section 2.4. While these equations are typically formulated for infinitely many beams in the dual lattice Λ^*, for all practical purposes it is sufficient to use only a few important beams, because at high energy and for thin specimens only very few beams are excited by scattering of the incoming beam. A mathematical analysis of the corresponding beam selection was given in Chapter 3, which was based on the work published in [KMM21]. This theoretical work was restricted to perfect crystals without inclusions. Here, we stay with finitely many beams, i.e. with so-called m-beam models with wave vectors $\mathbf{g} \in \Lambda^*_m$, but generalize the analysis to crystals with inclusions. The main assumption is, however, that the crystallographic lattice stays approximately intact and can be modeled as a strained crystal where the positions of the lattice points undergo a displacement $\mathbf{u}(\mathbf{r})$. Then, the DHW equation for strained crystals reads:

$$\frac{\mathrm{d}}{\mathrm{d}z}\varphi_{\mathbf{g}}(z) = 2\mathrm{i}\pi\Big(s_{\mathbf{g}} + \mathbf{g}\cdot\frac{\mathrm{d}}{\mathrm{d}z}\mathbf{u}(z;x,y)\Big)\varphi_{\mathbf{g}}(z) + \frac{\mathrm{i}\pi}{\rho_{\mathbf{g}}}\sum_{\mathbf{h}\in\Lambda^*_m} U_{\mathbf{g}-\mathbf{h}}\varphi_{\mathbf{h}}(z) \quad \text{for } \mathbf{g}\in\Lambda^*_m, \tag{5.1}$$

as was explained in Section 4.2. Here, $\varphi_{\mathbf{g}}$ denotes the wave function of the beam associated with $\mathbf{g} \in \Lambda^*_m$, where $\mathbf{g} = \mathbf{0}$ denotes the incoming beam. The vertical coordinate $z \in [0, z_*]$ gives the depth inside the specimen ($z = 0$ entry plane and $z = z_*$ exit plane), whereas the horizontal coordinates (x, y) are fixed and correspond to the image pixel, see Figure 2.8.

After a minor transformation the above system will take the vectorial form:

$$\dot{\phi} := \frac{\mathrm{d}}{\mathrm{d}z}\phi = \mathrm{i}\left(V + \Sigma + F(z)\right)\phi \quad \text{and} \quad \phi(0) = \sqrt{\rho_0}\, e_{\mathbf{0}} \in \mathbb{C}^m, \tag{5.2}$$

where $\phi = (\phi_{\mathbf{g}})_{\mathbf{g}\in\Lambda_m^*} \in \mathbb{C}^m$ contains the relevant wave functions. The Hermitian matrix V corresponds to the electrostatic interaction potential, the diagonal matrix $\Sigma = \mathrm{diag}(s_{\mathbf{g}})$ contains the so-called excitation errors and $F(z) = \mathrm{diag}(\mathbf{g} \cdot \frac{\mathrm{d}}{\mathrm{d}z}\mathbf{u}(x, y, z)) \in \mathbb{R}^{d\times d}$ contains the projections of the strains to the individual wavevectors $\mathbf{g} \in \Lambda_m^*$. We will call F the *strain profile*.

Image symmetries are now easily understood as changing the image pixel (x, y) to another pixel $(\widetilde{x}, \widetilde{y})$ having the same strains throughout the whole thickness, i.e. $\mathbf{u}(z; x, y) = \mathbf{u}(z; \widetilde{x}, \widetilde{y})$ for all $z \in [0, z_*]$, which implies $F(z) = \widetilde{F}(z)$. Such a situation is related to a symmetry of the inclusion generating a symmetric strain field. As we will see, additional symmetries may occur in (5.2) in three distinct cases:

1. if $F(z)$ is replaced by $-F(z)$, a so-called sign change;
2. if F is reflected at the midplane $z = z_*/2$, i.e. $F(z)$ is replaced by $F(z_*{-}z)$;
3. if Σ is replaced by $-\Sigma$.

The latter symmetry is relevant when a series of images is done while varying the excitation error $s_{\mathbf{g}}$ along the series.

These symmetries are observed experimentally (cf. [MNBL19]) but occur for the ODE system (5.2) only under additional conditions. Typically, the symmetries are exact only for the case of the two-beam model with $\Lambda_2^* = \{\mathbf{0}, \mathbf{g}'\}$. Nevertheless, the symmetries are approximately true in m-beam models if the intensities of the two strong beams (bright field and dark field intensities) are much higher than those of the weak beams. Next, we will see examples of symmetries in TEM images and explain these observations via the DHW equations.

5.2 Symmetries in TEM images

In this section, we study observed symmetries in TEM images of strained crystals and discuss their interpretation. To this purpose, we introduce selected examples demonstrating different kinds of symmetries, e.g. images that are pixelwise symmetric, like c) and e) in Figure 5.1. This kind of symmetry occurs when there is a sign change in the displacement component, see Section 5.2.1, or when the inclusion is shifted from the center, see Section 5.2.2. In Section 5.2.3, symmetries of a series of TEM images for varying excitation errors $s_{\mathbf{g}}$ and varying positions are discussed. These examples show the importance to distinguish

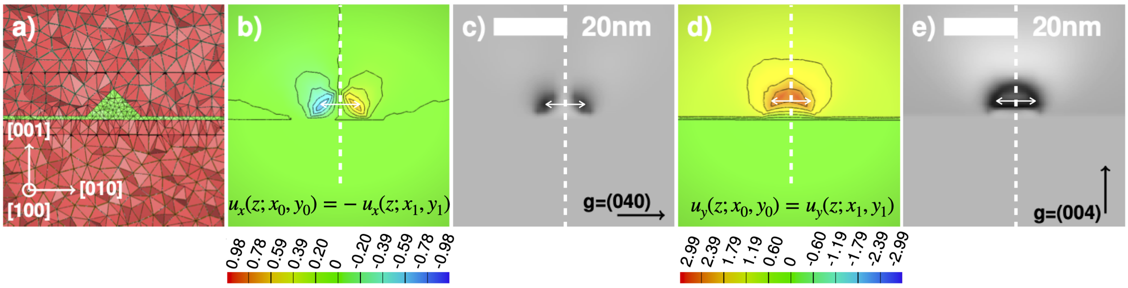

Figure 5.1: Simulation of TEM images for pyramidal QD: a) QD geometry indicating the crystallographic directions b) u_x component and d) u_y component of displacement field along a cross-section in the center of the structure. c) and e) corresponding TEM images for strong beam conditions as indicated by the direction of the chosen vectors $\mathbf{g}$. The images in the figure are adapted from [MNS+20, Fig. 5] used under CC-BY.

different kind of symmetries that can occur and to examine which ones are connected to specific properties of the displacement or strain profile and which are independent of it.

To understand the origin of these symmetries, we performed an analysis on the symmetry properties of solutions of the DHW equations. The main results are explained in Section 5.2.4, while the formal proofs are given in Section 5.3. This analysis revealed three important symmetry principles, stated in Section 5.2.4.3. By combining these principles with specific properties of the strain profiles, we can explain all the observed symmetries introduced in Sections 5.2.1-5.2.3. The capability of our approach to explain symmetries in TEM images beyond these examples is demonstrated in Section 5.2.6, where the developed theory is applied to a more complex problem featuring general displacement profiles.

5.2.1 Symmetry with respect to the sign of the displacement

In Figure 5.1 c) and e) we see two simulated TEM images for different choices of the vectors $\mathbf{g_{ap}}$. Each image is pixelwise symmetric, in the sense that for two different pixels (x_0, y_0) and (x_1, y_1) we have the same intensities: $I_{\mathbf{g_{ap}}}(x_0, y_0) = |\varphi_{\mathbf{g_{ap}}}(z_*; x_0, y_0)|^2 = |\varphi_{\mathbf{g_{ap}}}(z_*; x_1, y_1)|^2 = I_{\mathbf{g_{ap}}}(x_1, y_1)$. For image 5.1 e) this in not surprising since the profile of the vertical component of the displacement along the column related to pixel (x_0, y_0) is the same as the one for pixel (x_1, y_1), namely $u_y(z; x_0, y_0) = u_y(z; x_1, y_1)$ for $z \in [0, z_*]$, due to the symmetry of the pyramid. However, the pixelwise symmetry in image 5.1 c) is interesting: the profiles of the horizontal displacement component, which are responsible for the image contrast, have opposite values $u_x(z; x_0, y_0) = -u_x(z; x_1, y_1)$. This indicates that there might be some symmetry in TEM images with respect to the sign of the displacement.

In (5.1), we see that it is the product of the strain $\frac{d}{dz}\mathbf{u}$ with the reciprocal lattice vector $\mathbf{g}$ that enters the equations. This term will from now on be expressed as $F_{\mathbf{g}}(z) = \frac{d}{dz}(\mathbf{g} \cdot \mathbf{u}(z; x_i, y_j))$

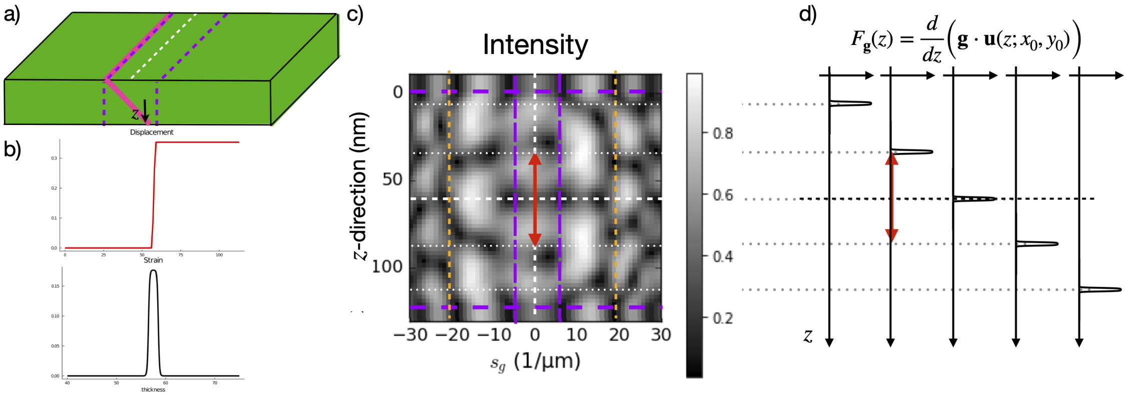

Figure 5.2: TEM imaging of inclined quantum well: a) illustration of a specimen for an inclined quantum well showing the z-direction and two line scans (purple dotted lines). b) The displacement (red) and strain (black) profiles projected to the reciprocal vector $\mathbf{g}_{\mathbf{ap}}$. c) Intensity values for different positions and different excitation errors $s_{\mathbf{g}_{\mathbf{ap}}}$ for a beam propagating in z direction. Adapted from [MNBL19, Fig.5] used under CC-BY. d) Strain profile for the different positions corresponding to a shift of the strain across the z direction.

and the influence of the strain to a m-beam system will be represented by the matrix-valued function $F(z) = \operatorname{diag}\left(F_{\mathbf{g}}\right)_{\mathbf{g}\in\Lambda_m^*}$. So, we want to know if the transformation $F(z) \rightsquigarrow -F(z)$ gives the same intensity. If it does, then the question that arises is whether it is for a specific shape of the strain profile $F(z)$ or it is independent of it and applies to general strain profiles.

5.2.2 Symmetry with respect to the center of the sample

Our next example is inspired by images provided in [MNBL19], where TEM imaging of an inclined strained semiconductor quantum well, like the one in Figure 5.2 a), has been studied. A quantum well is a planar heterostructure consisting of a thin film, forming the quantum well, sandwiched between barrier material layers forming the matrix. Due to the lattice mismatch between the materials, the lattice of the quantum well is deformed. For pseudomorphically grown quantum wells with perfect interfaces, it can be assumed that the displacement grows linearly within the quantum well region and has a constant value outside, resulting in a strain profile similar to an indicator function, see Figure 5.2 b).

The intensity values of the dark field for such a structure are shown in Figure 5.2 c), for different values of the excitation error and for different positions. Due to the incline angle between the planar interface and the imaging direction, the different positions correspond to different depths of the quantum well as measured from the surface of the specimen, see 5.2 a). An interesting first observation here is that the intensity seems to be symmetric with respect to a shift in the position from the center of the sample and for every excitation

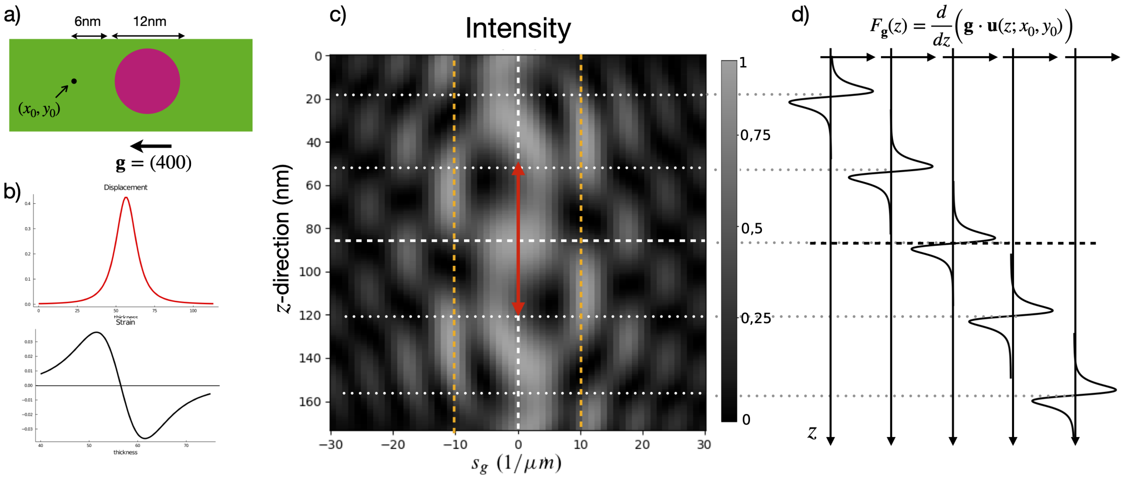

Figure 5.3: TEM imaging of spherical quantum dot: a) illustration of the specimen in (x, y) projection showing the direction of the chosen beam $\mathbf{g_{ap}}$. b) Propagating the beam across z for a chosen (x_0, y_0) gives the intensity at the corresponding pixel. The displacement (red) and strain (black) profiles projected to the reciprocal vector $\mathbf{g_{ap}}$. c) Intensity values for different positions and different excitation errors $s_{\mathbf{g_{ap}}}$. Adapted from [Nie21, Fig. 5.13] used under CC-BY. d) Strain profile for the different positions corresponding to a shift of the strain across the z direction.

error $s_{\mathbf{g_{ap}}}$. A natural question that occurs is whether this shifting symmetry is a general property of TEM imaging. The answer is negative and this can be seen in Figure 5.3 c) which shows the dark field intensities for a spherical quantum dot (Figure 5.3 a) again for different excitation errors and different positions. Shifting the quantum dot from the center, for an excitation error $s_{\mathbf{g_{ap}}} \neq 0$, does not give the same intensity. However, if we choose $s_{\mathbf{g_{ap}}} = 0$ then we observe again a symmetry with respect to shifting. To analyze these observations. we take a closer look into the shape of the strain in each case. For the quantum well in Figure 5.2, the strain profile is an even function (Figure 5.2 b)) while for the quantum dot in Figure 5.3, it is an odd function (Figure 5.3 b)). The latter is due to the symmetry of the sphere, cf. displacement field for spherical inclusion (4.1). Shifting the inclusion would correspond to shifting the strain in both cases as seen in Figures 5.2 d) and 5.3 d), respectively. The questions to be answered here are i) what is special in the case $s_{\mathbf{g_{ap}}} = 0$ that makes shifting a symmetry, ii) how does shifting an even or odd strain profile affect the intensities and iii) what happens for a general strain profile?

5.2.3 Symmetry with respect to the sign of $s_{\mathbf{g}}$

In the previous examples, we considered pixelwise symmetry for one specific image. This was expressed as $I_{\mathbf{g_{ap}}}(x_0, y_0) = I_{\mathbf{g_{ap}}}(x_1, y_1)$. In this section we talk about pixelwise symmetry between images. This means that if $I_{\mathbf{g_{ap}}}$ corresponds to the intensity of an image and $\widetilde{I}_{\mathbf{g_{ap}}}$ to the intensity of another image, then the two images are pixelwise symmetric if $I_{\mathbf{g_{ap}}}(x_i, y_j) = \widetilde{I}_{\mathbf{g_{ap}}}(x_i, y_j)$ for every pixel (i, j).

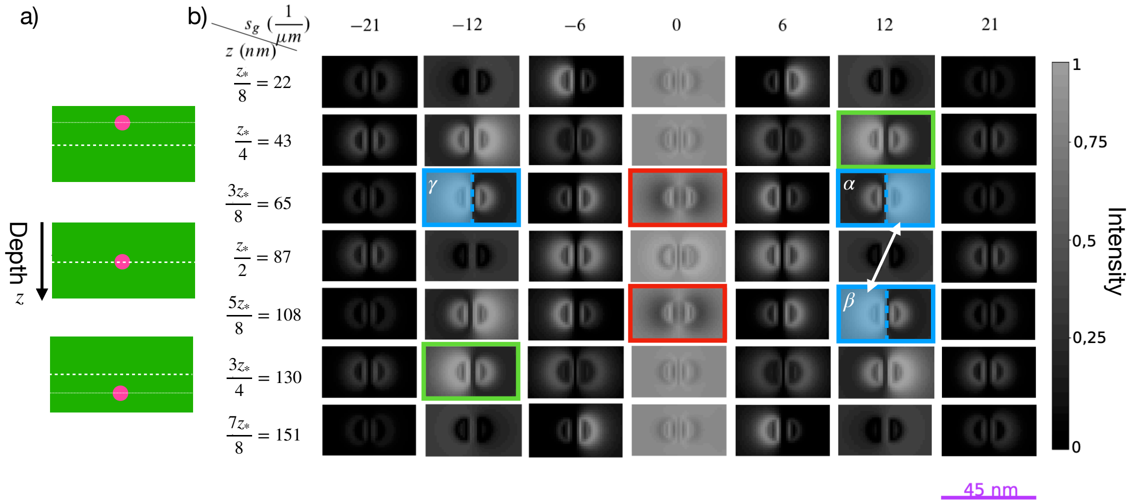

Figure 5.4: Series of TEM images for a spherical quantum dot: a) schematics of the position of quantum dot in the sample. b) simulated TEM images for different depths of the quantum dot and for different excitation errors $s_{\mathbf{gap}}$. For $s_{\mathbf{gap}} = 0$ the TEM images show a pixelwise symmetry with respect to the center (red boxes). For $s_{\mathbf{gap}} \neq 0$ the TEM images are symmetric with respect to the center if in addition the sign of the excitation error is changed (green boxes). The images are mirrored to each other with respect to the center for the same excitation error (α and β blue boxes) or with respect to the sign of the excitation error for a fixed position (α and γ blue boxes). Adapted from [Nie21, Fig.5.12] used under CC-BY.

In Figure 5.4, we have TEM images, adapted from [Nie21], of a spherical quantum dot at different positions and for different excitation errors. The observations we made for shifting at the previous section apply here as well. Shifting the quantum dot for an excitation error $s_{\mathbf{gap}} = 0$ creates images that are pixelwise symmetric with each other (red boxes), while for $s_{\mathbf{gap}} \neq 0$ they are not symmetric (α and β blue boxes). Shifting for an $s_{\mathbf{gap}} \neq 0$, however, seems to create mirrored images, in the sense that the image α is a mirrored version of image β with respect to the symmetry axis of the sphere.

Interestingly though, we see that if we shift the quantum dot from the center and additionally change the sign of the excitation error $s_{\mathbf{gap}}$, then the two images are pixelwise symmetric (green boxes or blue β and γ boxes). Again, the question that arises here is whether these observations are connected to a specific property of the strain profile or is there a symmetry connected to shifting and sign change of $s_{\mathbf{gap}}$ that occurs for general profiles?

5.2.4 Symmetries explained via DHW equations

To understand the symmetries in TEM images we described above, we studied the properties of the beam propagation through the specimen using the DHW equations. It turned out, that the intensity at the exit plane is invariant under specific transformations of the strain field. In the following, we give an introduction to our approach and an overview of the different types of symmetries formally defined and proved in mathematically rigorous terms in Section 5.3. We conclude the section with an explanation of the observed symmetries using the theory we developed.

5.2.4.1 Transformation to Hermitian form

To begin with, it is essential to use the self-adjoint structure that is somehow hidden in the DHW equations. This can either be done as in Chapter 3, where $\mathbb{C}^m$ is equipped with the scalar product $\langle a, b\rangle = \sum_{\mathbf{g}\in\Lambda_m^*} \rho_{\mathbf{g}} a_{\mathbf{g}} \overline{b}_{\mathbf{g}}$, or by the simple transformation:

$$\phi_{\mathbf{g}} = \sqrt{\rho_{\mathbf{g}}}\, \varphi_{\mathbf{g}} \text{ for } \mathbf{g} \in \Lambda_m^*,$$

which will be used in this chapter. This has the advantage that $\mathbb{C}^m$ is equipped with the standard (complex) Euclidean scalar product, but the intensities take the form $I_{\mathbf{g}}(x_i, y_j) = |\varphi_{\mathbf{g}}(z_*; x_i, y_j)|^2 = |\phi_{\mathbf{g}}(z_*; x_i, y_j)|^2/\rho_{\mathbf{g}}$.

In terms of $\phi = \left(\phi_{\mathbf{g}}\right)_{\mathbf{g}\in\Lambda_m^*} \in \mathbb{C}^m$, the system (4.2) is rewritten in matrix form as follows:

$$\dot{\phi} := \frac{\mathrm{d}}{\mathrm{d}z}\phi = \mathrm{i}\left(A + F(z)\right)\phi \quad \text{and} \quad \phi(0) = \sqrt{\rho_{\mathbf{0}}}\, e_{\mathbf{0}} \in \mathbb{C}^m. \tag{5.3a}$$

Subsequently, we will omit the normalizing factor $\sqrt{\rho_{\mathbf{0}}}$ in the initial condition $\phi(0)$, because it is not relevant in TEM imaging, where gray-scale pictures are created using relative intensities only. The system matrix $A = V + \Sigma$ and the influence $F(z)$ of the strain are given via:

$$V = \left(\frac{\pi U_{\mathbf{g}-\mathbf{h}}}{\sqrt{\rho_{\mathbf{g}}\rho_{\mathbf{h}}}}\right)_{\mathbf{g},\mathbf{h}\in\Lambda_m^*}, \quad \Sigma = \mathrm{diag}(2\pi s_{\mathbf{g}})_{\mathbf{g}\in\Lambda_m^*}, \quad F(z) = \mathrm{diag}\left(2\pi\frac{\mathrm{d}}{\mathrm{d}z}(\mathbf{g}\cdot\mathbf{u}(z))\right)_{\mathbf{g}\in\Lambda_m^*}, \tag{5.3b}$$

where V describes the interaction of the beams via the scattering potential and Σ is related to the excitation conditions. As the Fourier coefficients of the scattering potential satisfy $U_{-\mathbf{g}} = \overline{U}_{\mathbf{g}}$, we see that $V \in \mathbb{C}^{m\times m}$ is indeed a Hermitian matrix, while Σ and $F(z)$ are real-valued diagonal matrices.

What is important in TEM imaging is the intensity of the strongly excited beams at the exit plane $z = z_*$ and not all components of ϕ. Our theory is developed in such a way that it focuses on the amplitude of the undiffracted beam, $|\phi_{\mathbf{0}}(z_*)|$, which corresponds to a bright-field image. The point is that this generates a potential reflection symmetry $z \rightsquigarrow z_* - z$, because the initial condition $\phi(0) = e_0$ and the exit measurement $\phi_{\mathbf{0}}(z_*) = \phi(z_*)\cdot e_{\mathbf{0}}$ use the same vector $e_{\mathbf{0}}$.

Intensities of solutions for different choices of the pair $(A, F(z))$ are compared to see which replacements of (A, F) by $(\widetilde{A}, \widetilde{F}(z))$ lead to the same (measurement) results. Such transformations are then called symmetries. Changes in $F(z)$ correspond to transformations in the strain, while changes in the matrix A can correspond to transformations in the excitation errors (given by Σ) or the potential (given by U).

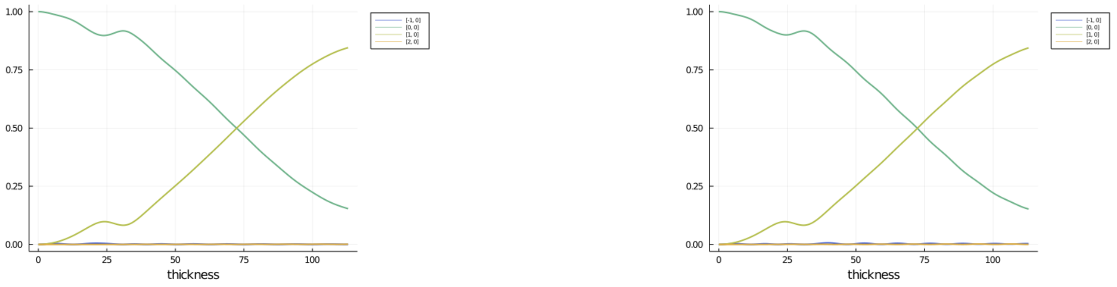

(a) System $(A, F(z))$

(b) System $(A, -F(z))$

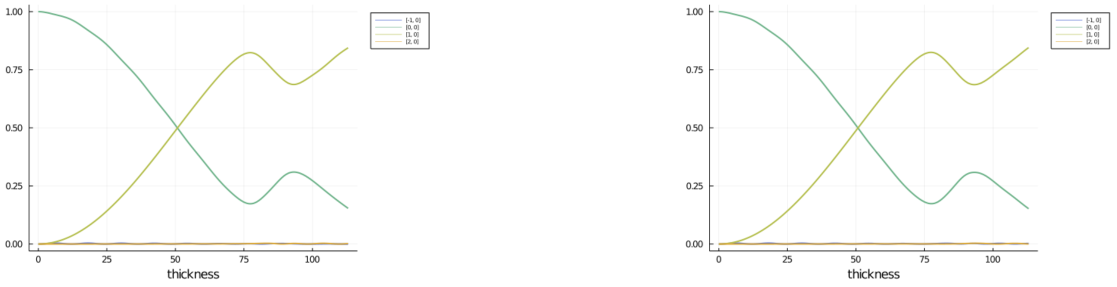

(c) System $(A, F(z_* - z))$

(d) System $(A, -F(z_* - z))$

Figure 5.5: Strong and weak symmetry in four-beam approximation: (a) Intensities for system $(A, F(z))$ used as reference (b) Intensities for system $(\widetilde{A}, \widetilde{F}(z)) = (A, -F(z))$. The solution $\widetilde{\phi}$ has a strong symmetry compared to the solution ϕ of (a). (c) Intensities for system $(\hat{A}, \widehat{F}(z)) = (A, F(z_* - z))$. The solution $\hat{\phi}$ has a weak symmetry compared to the solution ϕ of (a). (d) Intensities for system $(\tilde{A}, \widetilde{F}(z)) = (A, -F(z_* - z))$ showing a strong symmetry to case (c) and weak symmetry to (a) and (b).

5.2.4.2 Strong and weak symmetries

Two kinds of symmetries are defined in Section 5.3.1: *strong* and *weak symmetries*. For *strong symmetry*, the intensity of the beam along the whole column $[0, z_*]$ is invariant under the transformation $(A, F) \longrightarrow (\widetilde{A}, \widetilde{F})$. This means, the corresponding solutions ϕ and $\widetilde{\phi}$ satisfy $|\phi_\mathbf{0}(z)| = |\widetilde{\phi}_\mathbf{0}(z)|$ for all $z \in [0, z_*]$. For *weak symmetry*, this invariance holds for the intensity of the beam at the exit plane only, namely $|\phi_\mathbf{0}(z_*)| = |\widetilde{\phi}_\mathbf{0}(z_*)|$. In TEM imaging, this distinction is not visible since we only see the intensity at the exit plane. For the mathematical analysis, however, this distinction is highly relevant because of the different underlying mechanisms. Of course, any composition of weak and strong symmetries provides a weak symmetry again.

We illustrate strong and weak symmetries by numerical simulations of the DHW equations using four beams and a displacement field as given by (4.1), see Figure 5.5. In this example, we also observe a dark field symmetry, namely $|\phi_{\mathbf{g_{ap}}}(z)| = |\widetilde{\phi}_{\mathbf{g_{ap}}}(z)|$ (strong symmetry) or $|\phi_{\mathbf{g_{ap}}}(z_*)| = |\widetilde{\phi}_{\mathbf{g_{ap}}}(z_*)|$ (weak symmetry) with $\mathbf{g_{ap}} = (1, 0)$. In Table 5.1, we see the intensities for all four beams at the exit plane. While Figure 5.5 suggests an exact

$\mathbf{g}$	$(A, F(z))$	$(A, -F(z))$	$(A, F(z_* - z))$	$(A, -F(z_* - z))$
$(-1, 0)$	0.00012040357	$\underline{0.00}330035539$	$\underline{0.000}04461419$	$\underline{0.00}230899563$
$(0, 0)$	0.15359073146	$\underline{0.15}209371434$	$\underline{0.15359073146}$	$\underline{0.15}209371434$
$(1, 0)$	0.84539398729	$\underline{0.84}447759832$	$\underline{0.84}447759832$	$\underline{0.84539398729}$
$(2, 0)$	0.00089487769	$\underline{0.000}12833195$	$\underline{0.00}188705604$	$\underline{0.000}20330274$

Table 5.1: Comparison of intensities at the exit plane for the four-beam model in Figure 5.5. For both bright field ($\mathbf{g} = (0, 0)$) and dark field ($\mathbf{g} = (1, 0)$) we observe an *approximate symmetry* with an error of about 1%.

$\mathbf{g}$	$(A, F(z))$	$(A, -F(z))$	$(A, F(z_* - z))$	$(A, -F(z_* - z))$
$(0, 0)$	0.15309988945	$\underline{0.15309988945}$	$\underline{0.15309988945}$	$\underline{0.15309988945}$
$(1, 0)$	0.84690011055	$\underline{0.84690011055}$	$\underline{0.84690011055}$	$\underline{0.84690011055}$

Table 5.2: Comparison of intensities at the exit plane for the systems in Figure 5.5 and under two-beam approximation. Both bright and dark field show a *perfect symmetry* in this case (up to some numerical error).

symmetry, Table 5.1 reveals that the symmetry is only *approximate* with an error up to 1%. The reason is that the four-beam model does not enjoy the symmetries, however the solutions stay close to the solutions of the two-beam model, see Table 5.2 which has the desired symmetries. This simple example demonstrates the importance of the two-beam approximation in the study of symmetries for both bright field and dark field.

5.2.4.3 Three important symmetry facts

Here, we give an overview of the necessary results from Section 5.3 that help us explain the symmetries in TEM imaging observed at the beginning of the section. The results are stated as facts and put into physical terms, while the formal versions of them and the proofs can be found in the next section.

The first fact concerns the change in the sign of the strain, which corresponds to changing the sign of $F(z)$, and is proved in Corollary 5.3.3.

Fact 5.2.1. *In the two-beam approximation* $\Lambda_2^* = \{\mathbf{0}, \mathbf{g}'\}$ *and under strong beam conditions, i.e.* $s_\mathbf{0} = s_{\mathbf{g}'} = 0$, *changing the sign of the strain* ($F(z) \rightsquigarrow -F(z)$) *is a strong symmetry.*

The next fact concerns reflections at the midplane of the specimen given by the transformation $F(z) \rightsquigarrow F(z_* - z)$ and is proved in Corollary 5.3.5 part (W3).

Fact 5.2.2. *In the two-beam approximation* $\Lambda_2^* = \{\mathbf{0}, \mathbf{g}'\}$ *a midplane reflection of the strain* ($F(z) \rightsquigarrow F(z_* - z)$) *is a weak symmetry.*

Here, it is important to notice that Fact 5.2.2 does not require strong beam conditions, so it can be applied for excitation errors $s_{\mathbf{g}'} \neq 0$. This result is equivalent to the Type II symmetry in [PT68] or to [HW61] who showed this symmetry for bright field images. In the general m-beam case the midplane reflection symmetry holds under the assumption that all relevant $U_{\mathbf{g}}$ are real, see part (W2) of Corollary 5.3.5.

In the next fact, we combine the first two facts with an additional sign change of the excitation error $s_{\mathbf{g}'}$, proved in Corollary 5.3.6.

Fact 5.2.3. *In the two-beam approximation $\Lambda_2^* = \{\mathbf{0}, \mathbf{g}'\}$, combining the sign change of the strain with a midplane reflection ($F(z) \rightsquigarrow -F(z_* - z)$) and changing the sign of the excitation error $s_{\mathbf{g}'} \rightsquigarrow -s_{\mathbf{g}'}$ is a weak symmetry.*

The Type I symmetry in [PT68] is a special case of this results for $s_{\mathbf{g}'} = 0$. All results are derived for a general strain profile. The strain profiles in the examples we discussed before have an additional symmetry, namely they are even or odd functions which are shifted relative to the center of the specimen, see Figures 5.2d) and 5.3d). In the next subsection, we will show how the above observations interact with the parity of the strain profile $z \mapsto F(z)$.

5.2.4.4 Explanation of observed symmetries

With the symmetries that we have in hand, we are now able to answer all the questions that arose from the observations we made before. We start with the symmetry with respect to the sign of the strain ($F(z) \rightsquigarrow -F(z)$), that was discussed in Section 5.2.1 using the example of the pyramidal quantum dot in Figure 5.1. We can now say that this is a direct application of Fact 5.2.1 to every pair of pixels (i, j) and (i', j') such that $F(z; x_i, x_j) = -F(z; x_{i'}, y_{i'})$ and $F(z)$ being a general strain profile.

For the symmetry with respect to the center of the sample discussed in Section 5.2.2, a combination of the Facts 5.2.1 and 5.2.2 with the parity of the strain profile can explain the observations. We take each case separately. For the inclined quantum well the strain has an even profile, as in Figure 5.6 a). From Fact 5.2.2, we know that we can apply midplane reflection ($F(z) \rightsquigarrow F(z_* - z)$) and get the same pixel intensity. For an even profile midplane reflection and shifting coincide, see Figure 5.6 a). This is the reason why the image shows a pixelwise symmetry with respect to shifting. In the case of the spherical quantum dot, the strain has an odd profile, as in Figure 5.6 b). Applying midplane reflection we don't get the same result as shifting, see Figure 5.6 b). We would need to apply the sign change as well, as stated in Fact 5.2.1. This, however, can not be done unless we have strong beam conditions (meaning $s_{\mathbf{g}_{\mathrm{ap}}} = 0$). This is the reason why, for $s_{\mathbf{g}_{\mathrm{ap}}} = 0$, we observe a symmetry with respect to shifting while for $s_{\mathbf{g}_{\mathrm{ap}}} \neq 0$ we don't.

The observations concerning the sign change of the $s_{\mathbf{g}}$ made in Section 5.2.3, see e.g. green and red boxes in Figure 5.4, can be explained from Fact 5.2.3: it says that a midplane reflection combined with a sign change in the strain ($F(z) \rightsquigarrow -F(z_* - z)$) is a symmetry if we

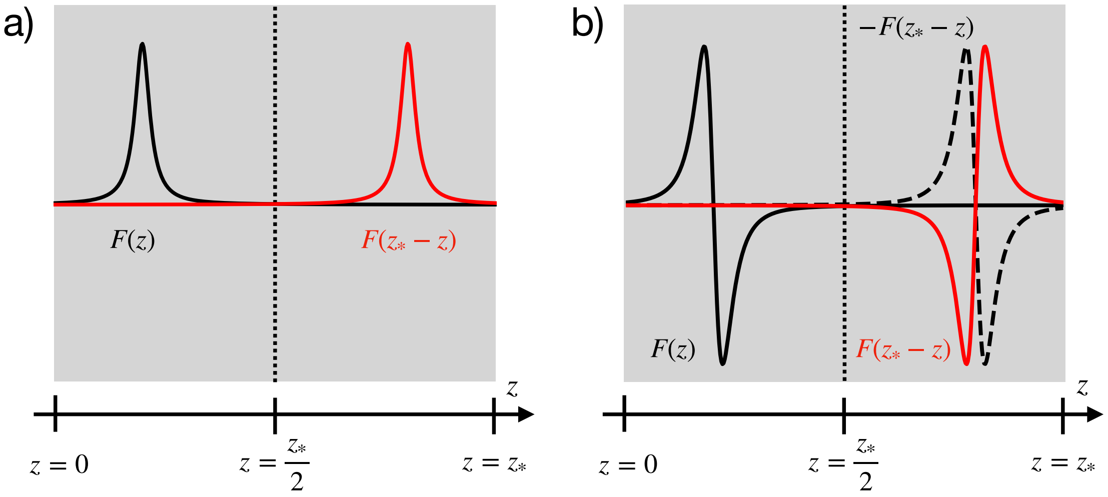

Figure 5.6: Plot of a shifted even function $F(z)$ (black) and the midplane reflection of it $F(z_* - z)$ (red) illustrating that the midplane reflection corresponds to shifting $F(z)$ a). Plot of a shifted odd function $F(z)$ (black) and the midplane reflection of it (red) illustrating that shifting (black dotted) needs an additional sign change to correspond to midplane reflection b).

also change the sign of the excitation error ($\Sigma \rightsquigarrow -\Sigma$). In this case, strong beam condition ($s_{\mathbf{gap}} = 0$) is not a requirement. This means that we can apply midplane reflection plus sign change of the strain, which for the odd strain profile in Figure 5.4 would correspond to shifting the strain profile with respect to the center, and then change the sign of the excitation error. This explains the symmetric images in Figure 5.4 indicated by the green and red boxes. The images in Figure 5.4 indicated by the blue boxes can also be explained now but we will do this in the next section, since they are not pixelwise symmetric as the previous examples but they have a mirror like symmetry.

5.2.5 Mirrored TEM images induced by strain

Here, we will focus on explaining the images in Figure 5.4 that are indicated by the blue boxes. First, we start with the TEM images α and β, see also Figure 5.7. This means we have two images of a spherical quantum dot using the same excitation error, here $s_{\mathbf{gap}} = 12\frac{1}{\mu m}$, but placed in different positions, symmetrical to the center of the sample, see Figure 5.7 a) and b).

To analyze the images pixelwise, we make two line scans in the z direction, A and B. The corresponding pixels for each image are indicated in Figure 5.7 a) (image α) and b) (image β), using the same notation A and B. We can see in Figure 5.7 a) that the pixel intensities corresponding to the line scans A and B in image α are not the same. So, the image itself does not have pixelwise symmetry. Comparing the pixels between the images α and β, though, shows that the pixel in the image α that corresponds to the line scan A (or B) is

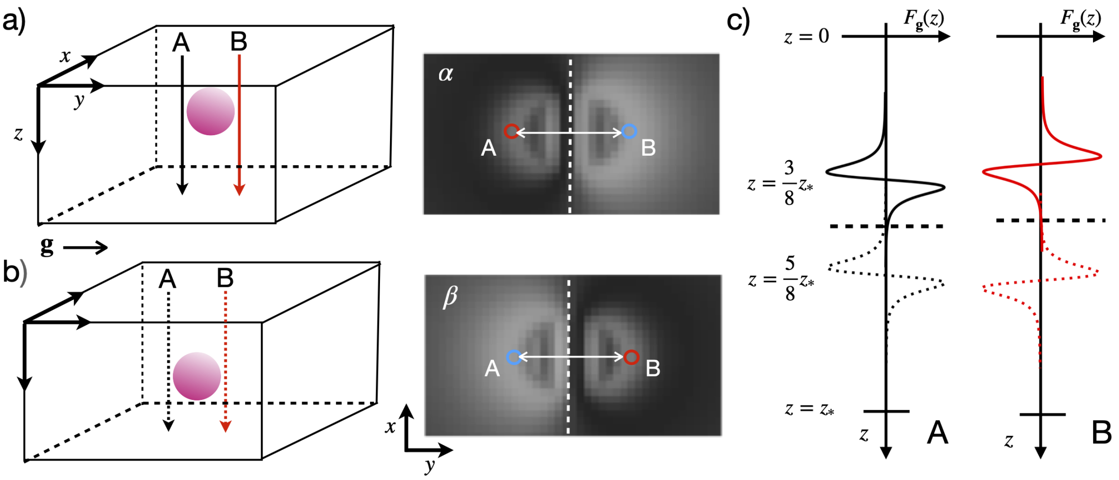

Figure 5.7: Mirrored images: a) Spherical quantum dot positioned at $z = \frac{3}{8}z_*$ and the corresponding TEM image (α). Solving the equations across the line scans A and B gives the corresponding pixels in α, denoted also by A and B. b) Spherical quantum dot positioned at $z = \frac{5}{8}z_*$ and the corresponding TEM image (β), showing again the pixels A and B that correspond to the same line scans. c) Strain profiles across the line scans A and B. The solid black and red profiles correspond to the TEM image α, while the dotted black and red profiles to TEM image β. The TEM images are adapted from [Nie21, Fig.5.12] used under CC-BY, cf. Figure 5.4.

the same as the pixel in the image β that corresponds to the line scan B (or A).

To understand these properties using the theory we developed, we study the strain profile for each line scan, shown in Figure 5.7 c). First, we focus on why the image itself is not pixelwise symmetric. For the quantum dot in image α, the strain profile across the two line scans is shown in Figure 5.7 c) by the solid black and red lines. We see that the difference between these two profiles is the sign. Changing the sign of the strain though is a symmetry only under strong beam conditions (Fact 5.2.1) but in this case we have $s_{\mathbf{g}_{\mathrm{ap}}} \neq 0$. The same exact argument applies to image β.

Next, we compare the two images with each other. The strain profile for the spherical quantum dot in image β is given in Figure 5.7 c) by the dotted black and red lines. The reason that the pixel corresponding to the line scan A in image α is equal to the one that corresponds to line scan B in image β is Fact 5.2.2, since the strain profile for the first case (solid black line in Figure 5.7 c)) is a midplane reflection of the strain profile in the second case (dotted red line in Figure 5.7 c)). This is due to the fact that for an odd function shifting the strain (black dotted line) plus sign change correspond to midplane reflection, see also Figure 5.6 b).

Additionally, from Fact 5.2.3, we know that image β is symmetric to the image γ in Figure 5.4. Combining all the above we can see why also the images corresponding to the same position but with opposite excitation errors are mirrored images of each other, see Figure

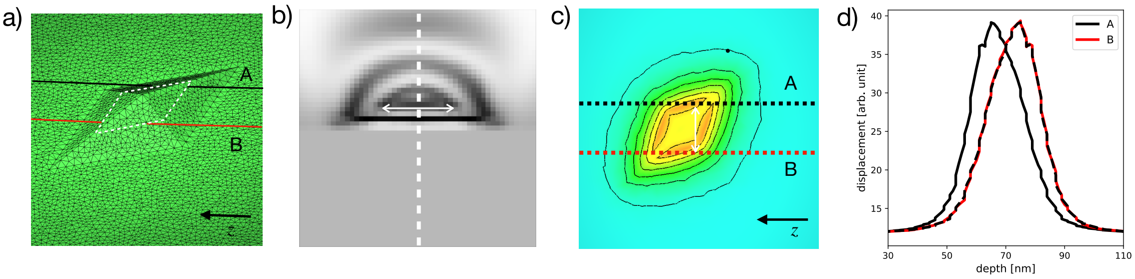

Figure 5.8: Pyramidal quantum dot with a rhomboidal base : a) 3D geometry showing the z direction and two line scans A and B. b) Simulated TEM image for $\mathbf{g_{ap}} = (004)$ showing a pixelwise symmetry. c) Displacement component responsible for the image contrast at the cut (white dotted lines) in a) and the line scans A and B. d) Displacement profiles across the line scans A (black solid) and B (red solid). We see that the displacement profile is not even nor odd and that the displacement in B is the midplane reflection of the displacement in A (black dashed).

5.4. This mirror-like symmetry is induced by the parity of the strain profile.

5.2.6 Symmetries for general profiles

The examples discussed until now were for a strain profile with odd or even parity. However, this parity is not the essential cause for the symmetries observed between two pixels. What is important is the symmetry between the strain profiles with respect to sign change and midplane reflection. To make this clear, we consider the case of a general strain profile without a specific parity. For this purpose, we examine TEM images of a pyramidal quantum dot with a rhomboid as a base instead of a square. We assume that the quantum dot is placed at the center of the sample. To create these TEM images, we used the computational method described in Chapter 4 and the toolchain employed therein. First, a 3D mesh is generated to represent the geometry of the quantum dot using TetGen [Si15], see Figure 5.8 a). Then, the generated mesh enters the FEM based solver WIAS-pdelib [FS+19], in order to find the displacement $\mathbf{u}$, see Figure 5.8 c). Finally, the relevant displacement component enters the DHW solver PyTEM [Nie19] in order to simulate the corresponding TEM image, see Figure 5.8 b). For this set up two TEM images are computed, corresponding to different vectors $\mathbf{g_{ap}}$ using strong beam excitation conditions.

For an excitation corresponding to $\mathbf{g_{ap}} = (004)$, the TEM image is shown in 5.8 b). The (projected) component of the displacement, which is responsible for the image contrast in this case, is shown in 5.8 c). This was taken in a cross-section parallel to the base of the pyramid, as indicated by the white dotted lines in 5.8 a). Next, we analyze the displacement profile along the two line scans A and B evolving in z-direction, as indicated in Figures 5.8 a) and c) by the black and red dotted lines. The displacement profiles across these line scans are shown in 5.8 d), where we can see that they are not even or odd. However, we observe a pixelwise symmetry in the TEM image. The displacement

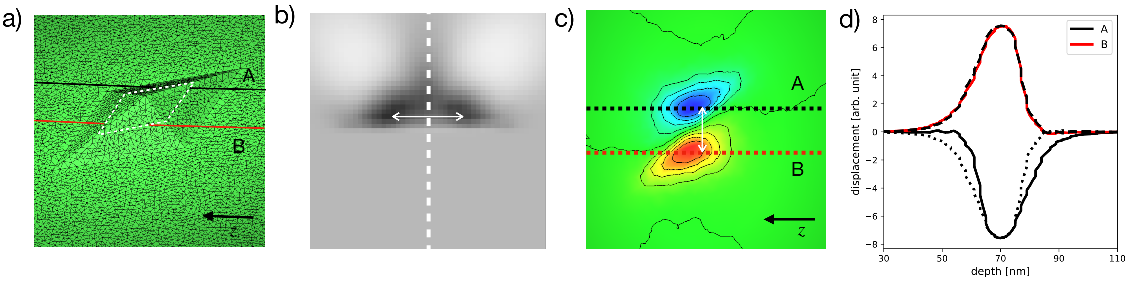

Figure 5.9: Pyramidal quantum dot with different lateral aspect ratio: a) 3D geometry showing the z direction and the two line scans A and B. b) Simulated TEM image for $\mathbf{g_{ap}} = (040)$ showing a pixelwise symmetry. c) Displacement component responsible for the image contrast at the cut (white dotted lines) in a) and the line scans A and B. d) Displacement profiles across the line scans A (black solid) and B (red solid). We see that the displacement profile is not even nor odd and that the displacement in B is the midplane reflection (black dotted) plus sign change of the strain in A.

$u_A(z)$ across line A is a midplane reflection of the displacement $u_B(z)$ across line B: $u_A(z_* - z) = u_B(z)$. This means that the strain across A differs with the strain across B by a sign plus midplane reflection, $\frac{d}{dz}u_B(z) = -\frac{d}{dz}u_A(z_* - z)$. Then, the symmetry we observe in the TEM image follows from Fact 5.2.3 and due to the strong beam condition ($s_{\mathbf{g}_{ap}} = 0$).

For an excitation corresponding to $\mathbf{g_{ap}} = (040)$, the TEM image is shown in 5.9 b). Under this excitation the imaging is sensitive to a different component of the displacement field as in the case before. The corresponding displacement field in the cross-section is shown in 5.9 c). We can see that the displacement obeys the sign change symmetry with respect to the center of the structure, as also observed for the pyramidal quantum dot with square base, see Figure 5.1. As in the example before, we plot the displacement profile across lines A and B as shown in 5.9 d). Here again we see that it is not even or odd. However, midplane reflection and sign change of the displacement profile in A equals the displacement in B: $u_B(z) = -u_A(z_* - z)$. This gives for the corresponding strain that $\frac{d}{dz}u_B(z) = \frac{d}{dz}u_A(z_* - z)$. Then, Fact 5.2.2 explains the pixelwise symmetry we observe. These two examples demonstrate that the results from Section 5.2.4.3 are indeed valid for a general displacement profile.

5.3 Mathematical treatment of the symmetries

We now provide the mathematics underlying the symmetry considerations for the solutions of the DHW equations. For this we use the general m-beam model in the Hermitian form derived in (5.3). To study the symmetries, we consider the system matrix $A = V + \Sigma$ and the strain function F as data specified to lie in the following spaces:

$$V \in \mathbb{C}^{m\times m}_{\text{herm}}, \quad \Sigma \in \mathbb{D}_m := \mathbb{R}^{m\times m}_{\text{diag}}, \quad F \in C^0([0, z_*]; \mathbb{D}_m).$$

The typical measurements for generating TEM images do not involve all components of $\phi(z_*) \in \mathbb{C}^m$ at the exit plane, but only the intensity of beam $\mathbf{g}_{\text{ap}} \in \Lambda^*_m$ selected by the objective aperture, see Figure 2.1, namely $I_{\text{ap}}(x_i, y_j) = |\phi_{\mathbf{g}_{\text{ap}}}(z_*; x_i, y_j)|^2$. As mentioned above, the so-called *bright field*, which is given by the choice $\mathbf{g}_{\text{ap}} = \mathbf{0}$, plays a special mathematical role. The reason for this is the double appearance of the vector $e_\mathbf{0}$, namely (i) in the initial condition $\phi(0) = e_\mathbf{0}$ and (ii) in the exit measurement $\phi_{\mathbf{g}_{\text{ap}}}(z_*) = \phi_\mathbf{0}(z_*) = \phi(z_*) \cdot e_\mathbf{0}$.

The double appearance of $e_\mathbf{0}$ can even be used for symmetries in the *dark field* where $\mathbf{g}_{\text{ap}} \neq \mathbf{0}$ under the assumption that we have a two-beam model, i.e. $\Lambda^*_2 = \{\mathbf{0}, \mathbf{g}'\}$ and $\mathbf{g}_{\text{ap}} = \mathbf{g}'$. In this case, we can exploit the Hermitian structure of (5.3) which provides the simple conservation of the Euclidean norm, namely $|\phi(z)| = |\phi(0)| = 1$ for all $z \in [0, z_*]$. This property was first derived in [KMM21, Sec. 3.1], where it was related to a wave-flux conservation in the Schrödinger equation. In this case, we have $|\phi_{\mathbf{g}'}(z)|^2 = 1 - |\phi_\mathbf{0}(z)|^2$ for all $z \in [0, z_*]$. Thus, if $|\phi_\mathbf{0}(z_*)|$ is preserved by a symmetry, then so is $|\phi_{\mathbf{g}'}(z_*)|$.

In light of the above discussions, we are interested in the question whether

- (sign change) flipping the function F into $-F$ or
- (midplane reflection) flipping $F(\cdot)$ into $F(z_* - \cdot)$

lead to the same value of $|\phi_\mathbf{0}(z_*)|$ or not.

To analyze these two symmetries and their joint effect, for both m-beam models and the two-beam model, we consider more general classes of transformations involving also changes of $A = V + \Sigma$ and not only of the strain related part F. This will uncover the proper mathematical structure of the symmetries and show why the case $m = 2$ is special. For this, we define two types of symmetries.

Definition 5.3.1 (Strong and weak symmetries)**.** *We say that replacing the pair* $(A, F) \in \mathbb{C}^{m\times m}_{\text{herm}} \times \mathrm{C}^0([0, z_*]; \mathbb{D}_m)$ *by the pair* $(\widetilde{A}, \widetilde{F})$ *is a* ***strong symmetry*** *if the corresponding solutions* ϕ *and* $\widetilde{\phi}$ *of* (5.3a) *satisfy* $|\phi_\mathbf{0}(z)| = |\widetilde{\phi}_\mathbf{0}(z)|$ *for all* $z \in [0, z_*]$.

We call the replacement a ***weak symmetry*** *if we have* $|\phi_\mathbf{0}(z_*)| = |\widetilde{\phi}_\mathbf{0}(z_*)|$.

Throughout this section, we will denote by $\mathbb{U}_{A+F}(z) \in \mathbb{C}^{m\times m}$ the evolution operator solving:

$$\dot{\mathbb{U}} = \mathrm{i}\big(A + F(z)\big)\mathbb{U}, \qquad \mathbb{U}(0) = I.$$

As $A + F(z)$ is Hermitian for all z, the evolution operators $\mathbb{U}_{A+F}$ are unitary, i.e.

$$\mathbb{U}_{A+F}(z)^{-1} = \big(\mathbb{U}_{A+F}(z)\big)^* = \overline{\mathbb{U}_{A+F}(z)}^{\top}. \tag{5.4}$$

In particular, this implies that the Euclidean norm $|\phi| = \big(\sum_{\mathbf{g}\in\Lambda_m^*}|\phi_\mathbf{g}|^2\big)^{1/2}$ is preserved for solutions $\phi(z)$ of (5.3). Of course, we have a general transformation rule for arbitrary unitary matrices $\mathbb{Q}\in\mathbb{C}^{m\times m}$ (i.e. $\mathbb{Q}^*\mathbb{Q}=I$), namely:

$$\mathbb{U}_{\mathbb{Q}(A+F)\mathbb{Q}^*}(z) = \mathbb{Q}\,\mathbb{U}_{A+F}(z)\mathbb{Q}^*. \tag{5.5}$$

The first result concerns the set of all strong symmetries.

Proposition 5.3.2 (Strong symmetries)**.** *Any of the following transformations and any composition of them are strong symmetries:*

(S1) *simultaneous linear phase factor:* $(\widetilde{A},\widetilde{F}) = (A+\delta I, F)$

(S2) *complex conjugation:* $(\widetilde{A},\widetilde{F}) = (-\overline{A}, -F)$

(S3) *constant phase factors:* $(\widetilde{A},\widetilde{F}) = (Q_\psi A Q_\psi^*, F)$ *with* $Q_\psi = \mathrm{diag}(1, \mathrm{e}^{\mathrm{i}\psi_2},\dots,\mathrm{e}^{\mathrm{i}\psi_m})$,

where $\delta,\psi_j\in\mathbb{R}$.

Proof. In all three cases, the result follows easily by writing down the corresponding evolution operators.

(S1) $\mathbb{U}_{\delta I+A+F}(z) = \mathrm{e}^{\mathrm{i}\delta z}\mathbb{U}_{A+F}(z)$ giving $\widetilde{\phi}_0(z) = \mathrm{e}^{\mathrm{i}\delta z}\phi_0(z)$.

(S2) By complex conjugation of (5.3a), we easily obtain $\mathbb{U}_{-\overline{A}-F}(z) = \overline{\mathbb{U}_{A+F}(z)}$. As the initial condition $\phi(0)=e_\mathbf{0}$ is real, we conclude $\widetilde{\phi}(z) = \overline{\phi(z)}$ and hence $\widetilde{\phi}_\mathbf{0}(z) = \overline{\phi_\mathbf{0}(z)}$.

(S3) For this case, we use the transformation rule (5.5) with $\mathbb{Q} = Q_\psi$ and observe that $Q_\psi F(z) Q_\psi^* = F(z)$ because F is diagonal. Hence, we have $\widetilde{\phi}_\mathbf{0}(z) = \phi_\mathbf{0}(z)$. ☐

As a first nontrivial result, we now reduce to the case $m=2$ with the additional restriction $A_{\mathbf{00}} = A_{\mathbf{g}'\mathbf{g}'}$. Indeed, the condition:

$$A_{\mathbf{00}} = A_{\mathbf{g}'\mathbf{g}'}, \quad \text{which means } \frac{U_\mathbf{0}}{\rho_\mathbf{0}} + 2s_\mathbf{0} = \frac{U_\mathbf{0}}{\rho_{\mathbf{g}'}} + 2s_{\mathbf{g}'},$$

is typically satisfied (in high enough accuracy) in the case of the strong two-beam conditions, because one usually chooses $s_{\mathbf{g}'} = s_\mathbf{0} = 0$ and one has $\rho_\mathbf{0} = \mathbf{k}_\mathbf{0}\cdot\boldsymbol{\nu}\approx\rho_{\mathbf{g}'}$. This holds automatically if $\mathbf{g}'\cdot\boldsymbol{\nu}=0$ or it is approximately true in the case of high energy electrons, i.e. $|\mathbf{k}_0|\gg|\mathbf{g}'|$.

Corollary 5.3.3 (Sign change using $m=2$ and $A_{\mathbf{00}} = A_{\mathbf{g}'\mathbf{g}'}$)**.** *In the case* $A = V+\Sigma\in\mathbb{C}^{2\times 2}_{\mathrm{Herm}}$ *with* $A_{\mathbf{00}} = A_{\mathbf{g}'\mathbf{g}'}$*, the transformation* $(\widetilde{A},\widetilde{F}) = (A,-F)$ *is a strong symmetry, i.e.* $|\widetilde{\phi}_\mathbf{g}(z)| = |\phi_\mathbf{g}(z)|$ *for* $z\in[0,z_*]$ *and* $\mathbf{g}\in\Lambda_2^* = \{\mathbf{0},\mathbf{g}'\}$.

Proof. The result follows by combining the three strong symmetries (S1)–(S3). We write:

$$A = \begin{pmatrix} a & b \\ \overline{b} & a \end{pmatrix} \quad \text{with } a \in \mathbb{R} \text{ and } b = |b|\mathrm{e}^{\mathrm{i}\beta}.$$

Applying first (S2), we find a strong symmetry with $(A_1, F_1) = (-\overline{A}, -F)$. Next, we apply (S1) with $\delta = 2a$ such that $(A_2, F_2) = (2aI - \overline{A}, -F)$ is again a strong symmetry. Finally, we apply (S3) with $\psi_2 = \pi - 2\beta$ and observe that $\mathrm{e}^{\mathrm{i}\psi_2} = -\mathrm{e}^{-\mathrm{i}2\beta}$, which gives:

$$\mathrm{diag}(1, -\mathrm{e}^{\mathrm{i}2\beta})\,\big(2aI{-}\overline{A}\big)\,\mathrm{diag}(1, -\mathrm{e}^{-\mathrm{i}2\beta}) = A.$$

Hence, $(A_3, F_3) = (A, -F)$ is a strong symmetry giving $|\widetilde{\phi}_{\mathbf{0}}(z)| = |\phi_{\mathbf{0}}(z)|$ for all $z \in [0, z_*]$.

Finally, the assumption $m = 2$ and the unitarity (5.4) give, for $\eta = \phi$ or $\widetilde{\phi}$, the relation:

$$|\eta_{\mathbf{0}}(z)|^2 \overset{m=2}{=} |\eta(z)|^2 - |\eta_{\mathbf{g}'}(z)|^2 \overset{\text{unit.}}{=} |e_{\mathbf{0}}|^2 - |\eta_{\mathbf{g}'}(z)|^2.$$

Hence, we obtain $|\widetilde{\phi}_{\mathbf{g}'}(z)| = |\phi_{\mathbf{g}'}(z)|$ from the corresponding result for $\mathbf{g} = \mathbf{0}$. ☐

To study the midplane reflection we introduce the

$$\textit{flip operator} \quad R(z) = z_*{-}z,$$

acting on $\mathrm{C}^0([0, z_*]; \mathbb{D}_m)$ via $(F{\circ}R)(z) = F(R(z)) = F(z_*{-}z)$. The following identity will be crucial for the understanding of the flip symmetry as a weak symmetry. Of course, one cannot expect that flipping gives rise to a strong symmetry. To see this, we consider a nontrivial strain profile F with $F(z) = 0$ for $z \in [z_*/2, z_*]$, i.e. the perturbation acts only in the upper half of the specimen. The flipped case $\widetilde{F} = F{\circ}R$ then corresponds to a perturbation acting only in the lower half of the specimen. In such a case, one cannot expect that the bright-field intensities $|\phi_{\mathbf{0}}(z)|^2$ and $|\widetilde{\phi}_{\mathbf{0}}(z)|^2$ are the same inside the specimen. However, because of the double occurrence of the vector $e_{\mathbf{0}}$ there is some chance that the intensities match for $z = z_*$ only.

Lemma 5.3.4 (Reversal of direction). *For all $A \in \mathbb{C}^{m\times m}_{\mathrm{herm}}$ and $F \in \mathrm{C}^0([0, z_*]; \mathbb{C}^{m\times m}_{\mathrm{herm}})$ we have the identity:*

$$\mathbb{U}_{-A-F\circ R}(z_*) = \big[\mathbb{U}_{A+F}(z_*)\big]^*. \tag{5.6}$$

Proof. We set $\widetilde{\mathbb{U}}(z) = \mathbb{U}_{A+F}(z_*{-}z)$, which obviously satisfies $\widetilde{\mathbb{U}}(z_*) = I$ and

$$\dot{\widetilde{\mathbb{U}}}(z) = -\dot{\mathbb{U}}_{A+F}(z_*{-}z) = -\mathrm{i}\big(A{+}F(z_*{-}z)\big)\mathbb{U}_{A+F}(z_*{-}z) = \mathrm{i}\big({-}A{-}(F{\circ}R)(z)\big)\widetilde{\mathbb{U}}(z).$$

Thus, $\widetilde{\mathbb{U}}$ satisfies the same ODE as $\mathbb{U}_{-A-F\circ R}$, but the initial conditions are different. This observation, $\widetilde{\mathbb{U}}(z_*) = I$, and the unitarity relation (5.4) imply:

$$\mathbb{U}_{-A-F\circ R}(z) = \mathbb{U}_{A+F}(z_*{-}z)\big[\mathbb{U}_{A+F}(z_*)\big]^{-1} = \mathbb{U}_{A+F}(z_*{-}z)\big[\mathbb{U}_{A+F}(z_*)\big]^*.$$

Restricting to the case $z = z_*$ gives the desired assertion. ☐

Of course, all compositions of a strong symmetry with a weak symmetry again provide a weak symmetry. Hence, combining the above lemma with Proposition 5.3.2 gives the following result that relies on the double occurrence of $e_{\mathbf{0}}$ in the definition of weak symmetries.

Corollary 5.3.5 (Flipping with R as weak symmetry)**.** *For all $A \in \mathbb{C}^{m\times m}_{\text{herm}}$ and $F \in \mathrm{C}^0([0,z_*];\mathbb{D}_m)$ the following transformations are weak symmetries:*

(W1) $(\widetilde{A},\widetilde{F}) = (-A,-F\circ R)$

(W2) $(\widetilde{A},\widetilde{F}) = (\overline{A},F\circ R)$

(W3) $(\widetilde{A},\widetilde{F}) = (A,F\circ R)$ *in the case* $m=2$.

Proof. We use that weak symmetry is defined in terms of:

$$\widetilde{\phi}_{\mathbf{0}}(z_*) = \big\langle \widetilde{\phi}(z_*), e_{\mathbf{0}}\big\rangle = \big\langle \mathbb{U}_{\widetilde{A}+\widetilde{F}}(z_*)e_{\mathbf{0}}, e_{\mathbf{0}}\big\rangle,$$

where $e_{\mathbf{0}}$ occurs as initial condition as well as test vector at $z=z_*$.

For (W1), we exploit the relation (5.6) from the previous lemma, which gives:

$$\widetilde{\phi}_{\mathbf{0}}(z_*) = \big\langle \mathbb{U}_{-A-F\circ R}(z_*)e_{\mathbf{0}}, e_{\mathbf{0}}\big\rangle = \big\langle \mathbb{U}_{A+F}(z_*)^*e_{\mathbf{0}}, e_{\mathbf{0}}\big\rangle = \big\langle e_{\mathbf{0}}, \mathbb{U}_{A+F}(z_*)^*e_{\mathbf{0}}\big\rangle = \overline{\phi_{\mathbf{0}}(z_*)}.$$

This immediately implies $|\widetilde{\phi}_{\mathbf{0}}(z_*)| = |\phi_{\mathbf{0}}(z_*)|$ as desired. For (W2) we simply apply the complex conjugation (S2) and use that F is real-valued.

For (W3), we start from (W2) and use $m=2$ to replace $\overline{A}$ by A using (S3) as for Corollary 5.3.3. □

From symmetry (W2) follows that, under the assumption that all relevant Fourier coefficients of the scattering potential $U_{\mathbf{g}}$ are real, the midplane reflection symmetry is also valid for the general m-beam model and not only for the two-beam approximation. This property may be satisfied for specifc crystal structures. One example are centrosymmetric materials, such as Al, Cu, and Au obeying a face-centered cubic lattice, see [De 03, Ch. 6.5].

Our last result concerns a symmetry in the two-beam model when one changes the sign of the excitation error $s_{\mathbf{g}'}$. This is relevant in experimental observations, where $s_{\mathbf{g}'}$ can easily be varied, cf. [Nie21]. In particular, we refer to the Figures 5.2, 5.3, and 5.4.

Corollary 5.3.6 (Excitation-error symmetry for $m=2$)**.** *Consider $\Lambda^*_2 = \{\mathbf{0},\mathbf{g}'\}$, $F \in \mathrm{C}^0([0,z_*];\mathbb{D}_2)$, and $A = V+\Sigma \in \mathbb{C}^{2\times 2}_{\text{Herm}}$ with $V_{\mathbf{00}} = V_{\mathbf{g}'\mathbf{g}'}$. Then, the transformation $(\widetilde{A},\widetilde{F}) = (V-\Sigma,-F\circ R)$ is a weak symmetry.*

Proof. The result follows by combining Corollary 5.3.3 and part (W3) of Corollary 5.3.5. More precisely, we first observe $\mathbb{U}_{A+F} = \mathbb{U}_{V+(\Sigma+F)}$. Applying Corollary 5.3.3 with (A, F) replaced by $(V, \Sigma+F)$ yields that $(A_1, F_1) = (V, -(\Sigma+F))$ is a strong symmetry. Combining this with part (W3) of Corollary 5.3.5 shows that $(A_2, F_2) = (V, -(\Sigma+F)\circ R)$ is a weak symmetry.

To conclude, we observe that $\Sigma\circ R = \Sigma$ because Σ is constant. Moving $-\Sigma$ into $\widetilde{A} = V - \Sigma$, we see that $(\widetilde{A}, \widetilde{F}) = (V-\Sigma, -F\circ R)$ is indeed a weak symmetry. □

Chapter 6

Summary and Outlook

The work presented in this thesis focused on the Darwin–Howie–Whelan equations. The structure of this system was analyzed mathematically and error estimates were provided to evaluate the accuracy of special approximations. In addition to this, the symmetry properties of the TEM imaging process were analyzed via the DHW equations. This analysis showed that the imaging process is invariant under special transformations. The most important symmetries are the sign change of the strain field and the midplane reflection, as well as a symmetry with respect to the sign change of the excitation error. Combining these results with specific properties of the strain profile of the inclusion explained extra symmetries observed in TEM images. This distinction between symmetries of the strain field and symmetries of the imaging process is particularly important to extract information for the inclusion, e.g. shape or size. A toolchain was also presented for the simulation of TEM images for quantum dots with realistic parametrized 3D geometries. This toolchain is not restricted to quantum dots but can also be applied to other epitaxial heterostructures or coherent precipitates. Using this toolchain, a study was performed on four different quantum dots shapes, which showed a strong sensitivity of the image contrast to the characteristics profiles of the strain field. FEM investigations showed that the strain field in the growth direction allows to distinguish between pyramidal and lens-shaped QDs. Therefore, TEM images of QDs under strong beam conditions in the growth direction are suitable for the classification of QDs shapes. From comparison with experimental data, a pyramidal structure (truncated or not) was excluded for InGaAs QDs, assuming a constant homogeneous indium content.

The results from the above mentioned work may find interesting applications in future studies of the DHW equations or TEM imaging. The analysis performed on the symmetry properties of TEM images could be applied to imaging of dislocations, since the TEM images are sensitive to the strain field they induce. Interesting questions like how would an external potential affect the symmetries or how can we explain symmetries observed in the phase could be approached by the theory developed here. From an application point of view, the database created by the toolchain described in this work could be used as a training set to apply deep learning techniques. Furthermore, statistical procedures might be useful to estimate continuous parameters such as height or base length of the QD. In any case, these and more interesting questions that may occur will require the collaboration of scientists from different fields in order to be answered.

Appendices

Appendix A

Lattice and elastic constants

For calculating the elastic strains in Section 4.3 we need the elastic stiffness tensor C for the distorted crystal, which for a material with cubic crystal system is:

$$C = \begin{pmatrix} C_{11} & C_{12} & C_{12} & 0 & 0 & 0 \\ C_{12} & C_{11} & C_{12} & 0 & 0 & 0 \\ C_{12} & C_{12} & C_{11} & 0 & 0 & 0 \\ 0 & 0 & 0 & C_{44} & 0 & 0 \\ 0 & 0 & 0 & 0 & C_{44} & 0 \\ 0 & 0 & 0 & 0 & 0 & C_{44} \end{pmatrix}. \tag{A.1}$$

The parameters C_{11}, C_{12} and C_{44} are the elastic constants, see Tab. A.1 for $InAs$ and $GaAs$.

	GaAs	InAs
a (Å)	5.653	6.058
C_{11} (GPa)	122.1	83.3
C_{12} (GPa)	56.6	45.3
C_{44} (GPa)	60.0	39.6

Table A.1: Lattice and elastic constants of GaAs and InAs taken from [VMR01].

For $In_{1-x}Ga_xAs$, with x being the indium content, the lattice and elastic constants are approximated in the following way:

$$\begin{aligned} a^{InGaAs} &= a^{GaAs} \cdot x + a^{InAs} \cdot (1-x) \\ C_{11}^{InGaAs} &= C_{11}^{GaAs} \cdot x + C_{11}^{InAs} \cdot (1-x), \\ C_{12}^{InGaAs} &= C_{12}^{GaAs} \cdot x + C_{12}^{InAs} \cdot (1-x), \\ C_{44}^{InGaAs} &= C_{44}^{GaAs} \cdot x + C_{44}^{InAs} \cdot (1-x). \end{aligned}$$

	x=0.2	x =0.7
a (Å)	5.977	5.7745
C_{11} (GPa)	91.06	110.4
C_{12} (GPa)	47.56	53.2
C_{44} (GPa)	43.68	53.8

Table A.2: Lattice and elastic constants of $In_{1-x}Ga_xAs$ in GaAs for x=0.2 and x=0.7.

Table A.2 shows the values for $x = 0.2$ and $x = 0.7$. The lattice misfit for an inclusion with lattice constant a^I inside a matrix with lattice constant a^M is defined via:

$$\delta = \frac{a^I - a^M}{a^M}.$$

Bibliography

[Bal66] C. S. Ball. “The Early History of the Compound Microscope”. In: *Bios* 37.2 (1966), pp. 51–60. ISSN: 00053155. URL: `http://www.jstor.org/stable/4606667`.

[BFAL96] T. Benabbas, P. Franņois, Y. Androussi, and A. Lefebvre. “Stress relaxation in highly strained InAs/GaAs structures as studied by finite element analysis and transmission electron microscopy”. In: *Journal of Applied Physics* 80.5 (1996), pp. 2763–2767. DOI: `10.1063/1.363193`.

[BFT+64] D. E. Bilhorn, L. L. Foldy, R. M. Thaler, W. Tobocman, and V. A. Madsen. “Remarks Concerning Reciprocity in Quantum Mechanics”. In: *Journal of Mathematical Physics* 5.4 (1964), pp. 435–441. DOI: `10.1063/1.1704136`. eprint: `https://doi.org/10.1063/1.1704136`. URL: `https://doi.org/10.1063/1.1704136`.

[Bor12] W. Borchardt-Ott. *Crystallography: An Introduction*. 3rd. Springer Berlin, Heidelberg, 2012. DOI: `10.1007/978-3-642-16452-1`.

[Bra50] A. Bravais. *Mémoire sur les systèmes formés par des points distribués régulièrement sur un plan ou dans l’espace*. Bachelier, 1850. URL: `https://books.google.de/books?id=S56znQEACAAJ`.

[CI16] E. Castellani and J. Ismael. “Which Curie’s principle?” In: *Philosophy of Science* 83.5 (2016). DOI: `10.1086/687933`.

[Dar14] C. G. Darwin. “The theory of X-ray reflexion. Part I and II”. In: *Phil. Mag.* 27.158+160 (1914), 315–333 and 675–690. DOI: `10.1080/14786440408635139`.

[De 03] M. De Graef. *Introduction to Conventional Transmission Electron Microscopy*. Cambridge University Press, 2003. DOI: `10.1017/CBO9780511615092`.

[DM12] M. De Graef and M. E. McHenry. *Structure of Materials: An Introduction to Crystallography, Diffraction and Symmetry*. 2nd ed. Cambridge University Press, 2012. DOI: `10.1017/CBO9781139051637`.

[Dyc76] D. van Dyck. “The importance of backscattering in high-energy electron diffraction calculation”. In: *phys. stat. sol. (b)* 77 (1976), pp. 301–308. DOI: `10.1002/pssb.2220770130`.

[Eng86] P. Engel. *Geometric Crystallography*. 1st. Springer Dordrecht, 1986. DOI: 10.1007/978-94-009-4760-3.

[Esh57] J.D Eshelby. "The Determination of the Elastic Field of an Ellipsoidal Inclusion, and Related Problems". In: *Proc. R. Soc. Lond. A.* 241 (1226 Aug. 1957), pp. 376–396. DOI: 10.1098/rspa.1957.0133.

[Ewa21] P. P. Ewald. "Die Berechnung optischer und elektrostatischer Gitterpotentiale". In: *Annalen der Physik* 3 (1921), pp. 253–287. DOI: 10.1002/andp.19213690304.

[FS+19] J. Fuhrmann, T. Streckenbach, et al. *pdelib: A finite volume and finite element toolbox for PDEs. [Software]*. 2019. URL: http://pdelib.org.

[FTK+72] F. Fujimoto, S. Takagi, K. Komaki, H. Koike, and Y. Uchida. "The reciprocity of electron diffraction and electron channeling". In: *Radiation Effects* 12.3-4 (1972), pp. 153–161. DOI: 10.1080/00337577208231136.

[Har11] M. Hartwig. "TEM-Untersuchungen der Spannungsfelder von In(Ga)As-Quantenpunkten". Bachelor's Thesis. TU Berlin, 2011.

[HW61] A. Howie and M. J. Whelan. "Diffraction contrast of electron microscope images of crystal lattice defects. II. The development of a dynamical theory". In: *Proc. Royal Soc. London Ser. A* 263.1313 (1961), pp. 217–237. DOI: 10.1098/rspa.1961.0157.

[HWM62] A. Howie, M. J. Whelan, and N. F. Mott. "Diffraction contrast of electron microscope images of crystal lattice defects. III. Results and experimental confirmation of the dynamical theory of dislocation image contrast". In: *Proceedings of the Royal Society of London. Series A. Mathematical and Physical Sciences* 267.1329 (1962), pp. 206–230. DOI: 10.1098/rspa.1962.0093.

[ISW74] J. C. Ingram, F. R. Strutt, and Wen-Shiantzeng. "An analysis of the symmetries in electron microscope images of a sloping down dislocation and its application as a method for dislocation characterization". In: *Phys. Status Solidi A* 22 (1974). DOI: 10.1002/pssa.2210220227.

[JAB+98] D. Jacob, Y. Androussi, T. Benabbas, P. Fraņois, and A. Lefebvre. "Surface relaxation of strained semiconductor heterostructures revealed by finite-element calculations and transmission electron microscopy". In: *Philosophical Magazine A* 78.4 (1998), pp. 879–891. DOI: 10.1080/01418619808239962.

[Jam90] R. James. "Applications of perturbation theory in high energy electron diffraction". PhD thesis. University of Bath, 1990.

[JLC+14] E. Javon, A. Lubk, R. Cours, S. Reboh, N. Cherkashin, F. Houdellier, C. Gatel, and M. J. Hÿtch. "Dynamical effects in strain measurements by dark-field electron holography". In: *Ultramicroscopy* 147 (2014), pp. 70–85. DOI: 10.1016/j.ultramic.2014.06.005.

[Kat80] K. H. Katerbau. "Diffraction contrast and defect symmetry". In: *Physica Status Solidi (a)* 59 (1980), pp. 211–221. DOI: 10.1002/pssa.2210590127.

[Kir20] E. J. Kirkland. *Advanced Computing in Electron Microscopy*. 3rd. Springer, 2020. DOI: 10.1007/978-1-4419-6533-2.

[KMM21] T. Koprucki, A. Maltsi, and A. Mielke. "On the Darwin–Howie–Whelan equations for the scattering of fast electrons described by the Schrödinger equation". In: *SIAM J. Appl. Math.* (2021), pp. 1551–1578. DOI: 10.1137/21M139164X.

[KMM22] T. Koprucki, A. Maltsi, and A. Mielke. "Symmetries in TEM imaging of crystals with strain". In: *arXiv* (2022). DOI: 10.48550/ARXIV.2206.01689.

[KMN+18] T. Koprucki, A. Maltsi, T. Niermann, T. Streckenbach, K. Tabelow, and J. Polzehl. "Towards model-based geometry reconstruction of quantum dots from TEM". In: *Proceedings of the 18th International Conference on Numerical Simulation of Optoelectronic Devices (NUSOD 2018)*. Ed. by Aleksandra Djurišić and Joachim Piprek. IEEE, 2018, pp. 115–116. DOI: 10.1109/NUSOD.2018.8570246.

[KMN+19] T. Koprucki, A. Maltsi, T. Niermann, T. Streckenbach, K. Tabelow, and J. Polzehl. "On a Database of Simulated TEM Images for In(Ga)As/GaAs Quantum Dots with Various Shape". In: *2019 International Conference on Numerical Simulation of Optoelectronic Devices (NUSOD)*. 2019, pp. 13–14. DOI: 10.1109/NUSOD.2019.8807025.

[Lic13] H. Lichte. "Electron Holography: phases matter". In: *Microscopy* 62.Suppl. 1 (2013), S17–S28. DOI: 10.1093/jmicro/dft009.

[LJC+14] A. Lubk, E. Javon, N. Cherkashin, S. Reboh, C. Gatel, and M. Hÿtch. "Dynamic scattering theory for dark-field electron holography of 3D strain fields". In: *Ultramicroscopy* 136 (2014), pp. 42–49. DOI: 10.1016/j.ultramic.2013.07.007.

[LZD+98] X. Z. Liao, J. Zou, X. F. Duan, D. J. H. Cockayne, R. Leon, and C. Lobo. "Transmission-electron microscopy study of the shape of buried $\mathrm{In}_x\mathrm{Ga}_{1-x}\mathrm{As}$/GaAs quantum dots". In: *Phys. Rev. B* 58 (8 Aug. 1998), R4235–R4237. DOI: 10.1103/PhysRevB.58.R4235.

[Mil39] W. H. Miller. *A Treatise on Crystallography*. Deighton, Cambridge, 1839.

[MKN+18] A. Maltsi, T. Koprucki, T. Niermann, T. Streckenbach, K. Tabelow, and J. Polzehl. "Model-based geometry reconstruction of quantum dots from TEM". In: *PAMM* 18.1 (2018), e201800398. DOI: https://doi.org/10.1002/pamm.201800398.

[MNBL19] L. Meißner, T. Niermann, D. Berger, and M. Lehmann. "Dynamical diffraction effects on the geometric phase of inhomogeneous strain fields". In: *Ultramicroscopy* 207 (2019). DOI: 10.1016/j.ultramic.2019.112844.

[MNS+20] A. Maltsi, T. Niermann, T. Streckenbach, K. Tabelow, and T. Koprucki. "Numerical simulation of TEM images for In(Ga)As/GaAs quantum dots with various shapes". In: *Opt. Quantum Electr.* 52 (May 2020), pp. 1–11. DOI: 10.1007/s11082-020-02356-y.

[Moo72] A. F. Moodie. "Reciprocity and Shape Functions in Multiple Scattering Diagrams". In: *Zeitschrift für Naturforschung A* 27.3 (1972), pp. 437–440. DOI: `doi:10.1515/zna-1972-0310`.

[Mur82] T. Mura. *Micromechanics of defects in solids*. 1st. Springer, 1982. DOI: `10.1007/978-94-011-9306-1`.

[Nie19] T. Niermann. *pyTEM: A python-based TEM image simulation toolkit*. Software. 2019. URL: `https://www.ioap.tu-berlin.de/menue/arbeitsgruppen/ag_lehmann/software/`.

[Nie21] L. Niermann. "Untersuchung und Anwendung der dynamischen Beugung an inhomogenen Verschiebungsfeldern in Elektronenstrahlrichtung in Halbleiterheterostrukturen". Doctoral Thesis. Berlin: Technische UniversitÃ€t Berlin, 2021. DOI: `10.14279/depositonce-11310`.

[Pas19] E. Pascal. "Dynamical models for novel diffraction techniques in SEM". PhD thesis. University of Strathclyde, 2019. DOI: `10.48730/9kj1-qa31`.

[PHN+18] E. Pascal, B. Hourahine, G. Naresh-Kumar, K. Mingard, and C. Trager-Cowan. "Dislocation contrast in electron channelling contrast images as projections of strain-like components". In: *Materials Today: Proceedings* 5 (2018), pp. 14652–14661. DOI: `10.1016/j.matpr.2018.03.057`.

[Pri82] E. Prince. *Mathematical techniques in crystallography and materials science*. 1st. Springer Berlin, Heidelberg, 1982. DOI: `10.1007/978-3-662-25351-9`.

[PSC+18] E. Pascal, S. Singh, P. G. Callahan, B. Hourahine, C. Trager-Cowan, and M. De Graef. "Energy-weighted dynamical scattering simulations of electron diffraction modalities in the scanning electron microscope". In: *Ultramicroscopy* 187 (2018), pp. 98–106. DOI: `10.1016/j.ultramic.2018.01.003`.

[PT68] A. P. Pogany and P. S. Turner. "Reciprocity in electron diffraction and microscopy". In: *Acta Crystallographica Section A* 24.1 (Jan. 1968), pp. 103–109. DOI: `10.1107/S0567739468000136`.

[QG89] L.C. Qin and P. Goodman. "An alternative study of the reciprocity theorem in electron diffraction". In: *Ultramicroscopy* 27.1 (1989), pp. 115–116. ISSN: 0304-3991. DOI: `https://doi.org/10.1016/0304-3991(89)90206-4`.

[Sen90] M. Senechal. *Crystalline Symmetries, An Informal Mathematical Introduction*. Taylor & Francis, 1990. ISBN: 9780750300414. URL: `https://books.google.de/books?id=SBvwAAAAMAAJ`.

[Si15] H. Si. "TetGen, a Delaunay-Based Quality Tetrahedral Mesh Generator". In: *ACM Transactions on Mathematical Software* 41 (2015), pp. 1–36. ISSN: 0098-3500. DOI: `10.1145/2629697`.

[Spi68] M. R. Spiegel. *Mathematical handbook of formulas and tables*. McGraw-Hill, New York, 1968.

[SRTL09] M. Schowalter, A. Rosenauer, J.T. Titantah, and D. Lamoen. "Computation and parametrization of the temperature dependence of Debye–Waller factors for group IV, III–V and II–VI semiconductors". In: *Acta Crystall. A* 65 (2009), pp. 5–17. DOI: 10.1107/S0108767308031437.

[SS93] R. Schäublin and P. Stadelmann. "A method for simulating electron microscope dislocation images". In: *Mater. Sci. Engin.* A164 (1993), pp. 373–378. DOI: 10.1016/0921-5093(93)90696-C.

[VMR01] I. Vurgaftman, J. R. Meyer, and L. R. Ram-Mohan. "Band parameters for III–V compound semiconductors and their alloys". In: *J. Appl. Phys.* 89 (2001), p. 5815. URL: http://aip.scitation.org/doi/abs/10.1063/1.1368156.

[WHHB57] M. J. Whelan, P. B. Hirsch, R. W. Horne, and W. Bollmann. "Dislocations and stacking faults in stainless steel". In: *Proc. R. Soc. Lond. A* 240 (1957), pp. 524–538. DOI: 10.1098/rspa.1957.0105.

[WK91] A. Weickenmeier and H. Kohl. "Computation of absorptive form factors for high-energy electron diffraction". In: *Acta Crystall. A* 47 (1991), pp. 590–597. DOI: 10.1107/S0108767391004804.

[WS19] W. Wu and R. Schaeublin. "TEM diffraction contrast images simulation of dislocations". In: *J. Microscopy* 275.1 (2019), pp. 11–23. DOI: 10.1111/jmi.12797.

[WTS+07] A. Winkelmann, C. Trager-Cowan, F. Sweeney, A. P. Day, and P. Parbrook. "Many-beam dynamical simulation of electron backscatter diffraction patterns". In: *Ultramicroscopy* 107 (2007), pp. 414–421. DOI: 10.1016/j.ultramic.2006.10.006.

[ZD20] C. Zhu and M. De Graef. "EBSD pattern simulations for an interaction volume containing lattice defects". In: *Ultramicroscopy* 218 (2020), pp. 113088/1–12. DOI: 10.1016/j.ultramic.2020.113088.